UNIVERSIDADE FEDERAL DE PERNAMBUCO
CENTRO DE TECNOLOGIA E GEOCIÊNCIAS
DEPARTAMENTO DE ELETRÔNICA E SISTEMAS
PROGRAMA DE PÓS-GRADUAÇÃO EM ENGENHARIA ELÉTRICA

TÚLIO DE LIMA PEDROSA

EVALUATING PLASMONIC NANOSCTRUCTURES FOR HIGH PERFORMANCE PHOTOTHERMAL THERAPY

Recife

2020

TÚLIO DE LIMA PEDROSA

EVALUATING PLASMONIC NANOSCTRUCTURES FOR HIGH PERFORMANCE PHOTOTHERMAL THERAPY

Dissertação apresentada ao Programa de Pós-Graduação em Engenharia Elétrica da Universidade Federal de Pernambuco como requisito parcial para obtenção do grau de Mestre em Engenharia Elétrica.

Área de Concentração: Fotônica.

Orientador: Prof. Renato Evangelista de Araujo.

Recife

2020

Catalogação na fonte
Bibliotecário Gabriel Luz, CRB-4 / 2222

P372e Pedrosa, Túlio de Lima.
Evaluating plasmonic na nosctructures for high performance photothermal therapy / Túlio de Lima Pedrosa – Recife, 2020.
110 f.: figs., tabs., abrev. e siglas, símbolos.

Orientador: Prof. Dr. Renato Evangelista de Araujo.
Dissertação (Mestrado) – Universidade Federal de Pernambuco. CTG. Programa de Pós-Graduação em Engenharia Elétrica, 2020.
Inclui referências e apêndice.

1. Engenharia Elétrica. 2. Lente térmica. 3. Nanopartículas metálicas. 4. Ressonância de plasmons de superfície localizados. 5. Terapia fototérmica. 6. Termoplasmônica. I. Araujo, Renato Evangelista de (Orientador). II. Título.

UFPE

621.3 CDD (22. ed.) BCTG / 2021 – 114

TÚLIO DE LIMA PEDROSA

EVALUATING PLASMONIC NANOSTRUCTURES FOR HIGH PERFORMANCE PHOTOTHERMAL THERAPY

Dissertação apresentada ao Programa de Pós-Graduação em Engenharia Elétrica da Universidade Federal de Pernambuco, como requisito parcial para a obtenção do título de Mestre em Engenharia Elétrica.

Aprovada em: 19/02/2020.

BANCA EXAMINADORA

_____

Prof. Dr. Renato Evangelista de Araujo (Orientador)
Universidade Federal de Pernambuco

_____

Prof. Dr. Leonardo de Souza Menezes (Examinador Externo)
Universidade Federal de Pernambuco

_____

Prof. Dr. George Boudebs (Examinador Externo)
Université d'Angers

Aos meus pais.

ACKNOWLEDGEMENTS

Agradeço primeiramente a minha família por todo o suporte por eles proporcionado durante todos esses anos, fundamental para que eu pudesse dar um passo adiante. A motivação diária a mim alimentada por meio do carinho e do afeto recebido de todos em meu leito familiar. A minha mãe Cristiane e ao meu pai Emerson pelo exemplo diário de esforço, humildade e humanidade. A minha irmã Tábata e ao meu irmão Tales pelos momentos compartilhados durante todos estes anos.

Ao Professor Renato Evangelista de Araujo pelo acolhimento no LOBI, e por toda paciência durante a minha instrução. Por ter acreditado no meu potencial e pela fundamental contribuição para o meu desenvolvimento pessoal e científico durante os dois anos que passei sob sua orientação. Meus sinceros agradecimentos.

A toda a equipe que compõe o LOBI, companheiros e companheiras de trabalho que tornam o ambiente de convívio agradável. Meus mais sinceros agradecimentos a Sandra Holanda, Fábio Rodrigo, Gabrielli Ferreira, Caio Vital, Raphael Baltar e a Olavo Cardozo pelas contribuições por meio de sugestões e discussões cieníficas e salutares. Em especial, agradeço a Sajid Farooq e a Carlos López, que contribuíram de maneira fundamental na minha compreensão dos temas que constituem este trabalho, e a Arthur Pimentel e Iasmim Araújo pelo suporte desempenhado nele.

Por fim, agradeço a todos os alunos e professores que constituem o Asa Branca Rocket Design, em especial Edmar Soares e Gabriel Fernandes pelos laços construídos e pela rede de suporte e motivação que se constrói indiretamente sobre essas relações, e ao professor Hermano Cabral.

"I should like to say two things, one intellectual and one moral:

The intellectual thing I should want to say to them is this: When you are studying any matter or considering any philosophy, ask yourself only what are the facts and what is the truth that the facts bear out. Never let yourself be diverted either by what you wish to believe or by what you think would have beneficent social effects if it were believed, but look only and solely at what are the facts. That is the intellectual thing that I should wish to say.

The moral thing I should wish to say to them is very simple. I should say: Love is wise, hatred is foolish. In this world, which is getting more and more closely interconnected, we have to learn to tolerate each other. We have to learn to put up with the fact that some people say things that we don't like. We can only live together in that way, and if we are to live together and not die together we must learn a kind of charity and a kind of tolerance which is absolutely vital to the continuation of human life on this planet."

Bertrand Russell, Face-to-Face - BBC (1959)

RESUMO

O controle de temperatura em tecidos biológicos tem sido amplamente utilizado para aplicações terapêuticas em diversas áreas da medicina tais como oncologia, fisioterapia, urologia, cardiologia e oftalmologia. A Terapia Fototérmica (TFT) baseia-se na indução de danos celulares por meio de absorção de luz por um tecido alvo. Entretanto, para um efetivo uso de luz em TFT, um aquecimento controlado e localizado deve ser obtido. O aquecimento localizado pode ser alcançado por meio da exploração de estruturas nanoplasmônicas. Este trabalho tem como objetivos a avaliação de nanoaquecedores para alta performance em TFT. Análises teóricas e experimentais foram realizadas para a aferição de propriedadas termo-ópticas de nanoestruturas de ouro e colóides metálicos. Parâmetros ópticos cruciais que determinam o aquecimento plasmônico foram avaliados, explorando a dependência com o tamanho das nanopartículas. Baseando-se no Método dos Elementos Finitos, os comprimentos ótimos dos nanobastões de ouro encontrados para TFT infravermelha foram de 45 nm e 60 nm para comprimentos de onda de 800 nm e 1064 nm respectivamente, no regime de excitação de nanosegundos. Para excitações contínuas, a geração de calor mostra uma tendência a maximizar-se em nanobastões com comprimentos maiores que 100 nm. A avaliação da performance das nanopartículas como nanoaquecedores é um passo fundamental no desenvolvimento de nanoplataformas eficientes para TFT. Na caracterização térmica de coloides metálicos, foi explorada a técnica de lente térmica, onde o aquecimento óptico de uma solução coloidal de nanoesferas de ouro com 50 nm de diâmetro foi analisado pela técnica de duplo feixe com *mode-mismatch*. Variações térmicas de até 1.28 ^{o}C foram medidas na região do laser de excitação. A introdução da técnica de lente térmica na avaliação do foto-aquecimento de coloides consite em uma abordagem inovadora e de grande potencial para a caracterização de nanoaquecedores.

Palavras-chave: Lente Térmica. Nanopartículas Metálicas. Ressonância de Plasmons de Superfície Localizados. Terapia Fototérmica. Termoplasmônica.

ABSTRACT

Tissue temperature control has been widely used for therapeutic application in several areas of medicine as oncology, physiotherapy, urology, cardiology and ophthalmology. Photothermal therapy (PTT) is based on the induction of cellular damage by light absorption in a target tissue. For an effective use of light on PTT, controlled and localized heating should be achieved. Localized heating has been accomplished by exploring plasmonic nanostructures. This work has as its main objective the evaluation of nanoheaters for high performance PTT. Experimental and theoretical analysis were employed to assess thermo-optical properties of gold nanostructures and metallic colloids. Crucial optical parameters ruling plasmonic heating were appraised, exploiting a nanoparticle size-dependence approach. Based on the finite-element method, the optimum size of gold nanorods for high performance infrared thermal therapy were found to be 45 nm and 60 nm at wavelengths of 800 nm and 1064 nm respectively for nanosecond pulse. For continuous excitation, particle morphology presents high significance, and heat generation shows the tendency to peak at lengths longer than 100 nm. The performance evaluation of nanoparticles as nanoheaters is a fundamental step to the development of efficient nanoplatforms for photothermal therapy. Here, the use of Thermal Lens technique on the characterization of nanoheaters was introduced. Optical heating of a colloidal solution of 50 nm diameter gold nanospheres were assessed by mode-mismatched Dual-Beam Thermal Lens technique. Temperature variations up to 1.28 ^{o}C were evaluated at the region of the excitation beam. The introduction of the Thermal Lens technique for the evaluation of heat generation in colloidal solutions of nanoparticles consists in a innovative approach for nanoheater characterization, with great potential.

Keywords: Localized Surface Plasmon Resonance. Metallic Nanoparticles. Photothermal Therapy. Thermal-Lens Technique. Thermoplasmonics.

LIST OF FIGURES

LIST OF TABLES

LIST OF ABBREVIATIONS AND ACRONYMS

AD	*Anno Domini*
AR	Aspect Ratio
CCP	Charge Coupled Plasmon
CDD	Charged Coupled Device
CMOS	Complementary Metal Oxide Semiconductor
CTP	Charge Transfer Plasmon
CW	Continuous Wave
DTL	Dual Thermal Lens
F-D	Fermi-Dirac Distribution
FEM	Finite Element Method
L_n	n^{th} lens
LSPR	Localized Surface Plasmon Resonance
NIR	Near Infrared
NP	Nanoparticle
PD	Photo-diode
PML	Perfect Matched Layer
PTT	Photothermal Therapy
STL	Single Thermal Lens
TFT	Terapia Fototérmica
TL	Thermal Lens
UV	Ultraviolet

LIST OF SYMBOLS

ℓ	Optical path length.
z	Sample position.
z_R	Rayleigh length.
z_{op}	Probe beam Rayleigh length.
w_0	Beam waist.
w_{ex}	Pump beam waist.
w_p	Probe beam waist.
C_{np}	Nanoparticle concentration.
P_{exc}	Excitation power.
P_{abs}	Absorbed power.
P_{loss}	Power loss.
ϵ_0	Vacuum permittivity.
ϵ	Relative permittivity.
ϵ'	Real part of relative permittivity.
ϵ"	Imaginary part of relative permittivity.
ϵ_m	Relative permittivity of the medium.
ϵ_{bulk}	Permittivity of bulk metal.
ϵ_{intra}	Contribution of intraband transitions to metal permittivity.
ϵ_{inter}	Contribution of interband transitions to metal permittivity.
ω	Angular frequency.
ω_p	Plasma frequency.
γ_0	Bulk Drude damping parameter.
γ	Modified Drude damping parameter.
N	Electron density.

N_p	Amount of nanoparticles.
e	Elementary charge.
m_e	Electron rest mass.
M	Nanoparticle mass.
A	Phenomenological scattering parameter.
v_F	Fermi velocity.
l_∞	Electron mean free path of bulk metals.
L_{eff}	Effective electron mean free path of metallic nanoparticles.
V	Volume.
S	Surface area.
R	Radius.
j	Imaginary unit.
d	Nanosphere diameter.
λ	Wavelength.
λ_{ref}	1 eV reference wavelength.
E_0	Incident electric field.
E_{in}	Internal electric field.
E_{ext}	External electric field.
a	Nanosphere radius.
$\vec{r}$	Position vector.
$\vec{E}$	Electric field vector.
$\vec{n}_r$	Radial unit vector.
$\vec{n}_\theta$	Polar unit vector.
$\vec{n}_z$	z-direction unit vector.
$\vec{p}$	Dipole moment vector.
α_p	Nanoparticle polarizability

κ	Thermal conductivity.
κ_m	Thermal conductivity of the medium.
a_n	Scattering coefficient a of nth order.
b_n	Scattering coefficient b of nth order.
σ_{ext}	Extinction cross-section.
σ_{sca}	Scattering cross-section.
σ_{abs}	Absorption cross-section.
m_r	Relative refractive index.
x	Nanosphere size parameter.
ψ_n	Riccati-Bessel function of the 1st kind and nth order.
ξ_n	Riccati-Bessel function of the 2st kind and nth order.
$\vec{q}$	Heat power density vector.
η	Photothermal conversion efficiency.
T	Temperature.
T_0	Initial temperature.
T_∞	Steady-state temperature.
τ	Thermalization time.
τ_{np}	Nanoparticle thermalization time.
τ_{global}	Global thermalization time.
τ_m	Thermalization time of the medium.
D_{th}	Thermal diffusivity.
Q	Energy absorbed by the nanoparticle.
ρ	Density.
C_p	Heat capacity.
I	Laser intensity.
θ	Thermal lens strength.

t	Time.
t_c	Characteristic time.
α	Absorption coefficient.
ΔT	Temperature variation.
ΔT_{np}	Nanoparticle temperature variation.
ΔT_{global}	Global temperature variation.
ΔT_{max}	Maximum temperature variation.
C_{th}	Thermal capacitance.
β	Nanoparticle shape factor.
R_{eq}	Equivalent radius.
J_0	Joule number.
S^2F	Steady-state factor.
C	Concentration.
C_0	Initial concentration.
R_{gas}	Universal gas constant.
ΔE	Energy change.
A_{rrh}	Arrhenius constant.
L	Nanorod length.
D	Nanorod diameter.
f	Focal length.
f_{Ln}	Focal length of n^{th} lens.
Σ	Aperture size.
n	Refractive index.
n_0	Initial refractive index.
Φ	Phase-shift.
v	Normalized sample position.

m	Mode-match factor.
h	Heat transfer coefficient.
G	Rate of temperature change.
B	Rate constant associated with heat loss.

CONTENTS

1 INTRODUCTION

Metals have always been worthy of human attention. Since the beginning of civilization, mankind has shown interest in this type of material, employing it in many different ways throughout history. At first, the characteristic shininess of metals when compared with small rocks present in nature lured the attention of early human wanderers to it. They started to wear metal shards found in the wild as ornaments and as collectible items.

Later, it was found that specific types of metals (noble metals, for instance) presented enough softness to be worked by primitive tools and had enough resistance to endure corrosion over time, when compared to other varieties of those “lustrous materials” that were very sturdy and prone to corrosion. Did not take too long until these special types of metals started to be employed as distinguishable jewelry and as a medium of exchange in early societies.

Technological advancements in metalworking led to the development of tools that were sharper and more durable, helping to kick-start the emergence of the first known civilizations. Thereafter, technology evolved slowly, but steadily until the advent of the age of enlightenment. This age will mark the beginning of industrial revolution and a great boost in all fields of scientific investigation, where metals once again proved to be vital, allowing the development of scientific instruments, new machines and structures. To this day, metals are still extremely important in maintaining aspects of our modern life as well as playing a significant role in technical and basic research.

Despite of all the acknowledgement received by metals for being practically ubiquitous in our everyday life, appearing in various shapes, ways and applications, there is a much less known side and much less evident role played by it that is not directly noticeable. This role is attached to what is not immediately apparent to our senses: the realm of nanoscience and nanotechnology. Throughout history, inadvertent examples of nanotechnology can be found.

One remarkable and widespread example is the late Roman era Lycurgus Cup from the 4^{th} century AD. The glass of the cup is dichroic, presenting a opaque greenish-yellow tone to light reflected by the glass, while presenting a translucent ruby-red colour to light transmitted through the glass. Experiments in samples of glass melts confirmed that the behavior of the cup is linked to the presence of of gold (about 40 ppm) and silver (about 300 ppm) nanoparticles in glass. This colloidal system gives rise to light scattering effects with the gold component being responsible for the reddish transmission effect and the silver for the greenish reflection effect (FREESTONE et al., 2007). Figure 1 shows the dichroism present in the Lycurgus Cup.

Another use of nanotechnology in old times is the production of lustre pottery. This activity can be traced to as early as the Bronze Age (COLOMBAN, 2010). The optical properties of the lustre are related to the concentration ratio between copper and silver nanoparticles

Figure 1 – Dichroism present in the Lycurgus Cup. (a) Greenish reflection effect from silver nanoparticles. (b) Redish transmission effect from gold nanoparticles.

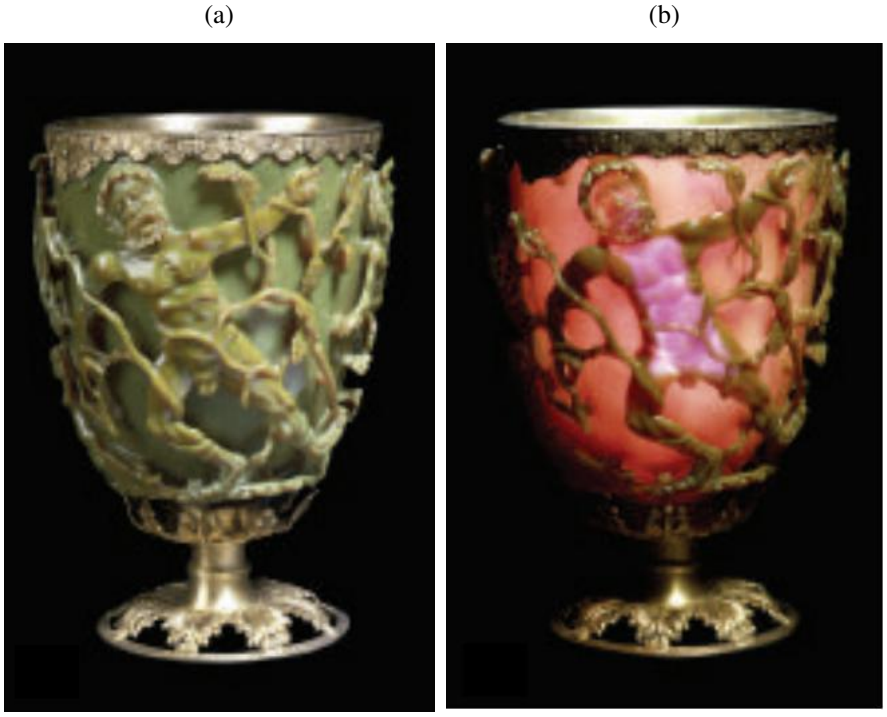

Source: adapted from (FREESTONE et al., 2007).

deposited as a thin film on the glazed surface. Changes in concentration ratio allows different nanostructures to be formed, creating colour effects ranging from gold lustre to yellow and red to copper-like lustre. The gold lustre is caused by a well-separated Ag and Cu mixture of quasi-spherical nanocrystals ranging from 5 to 100 nm (BORGIA et al., 2002). This same technique was still in use during the middle ages until the 17th century at least (CLIMENT-FONT, 2012).

The nanotechnology of the past wasn't restricted only to the use of metallic nanocrystals in coloring applications. It also saw applicability in warfare. The 17th century Damascus Sabre presents extraordinary mechanical properties and exceptionally sharp cutting edges. The TEM analysis of a sample of its blade indicated the presence of carbon nanotubes and cementite nanowires. The general assumption is that it was forged by a sophisticated thermomechanical treatment from small cakes of steel produced in India (REIBOLD et al., 2006), but the technique was long lost. Figures 2a and 2b shows respectively different color effects created by nanocrystals and nanostructures present in Damascus Sabre.

Later on, in 1857, Michael Faraday studied the optical properties of thin films made out of various metals and alloys, including gold and silver. The analysis of light interaction with a gold, copper and silver alloy beaten to a translucent thin film (mostly comprised of gold) and placed over a slab of glass revealed to reflect yellow light and transmit a greenish

Figure 2 – Examples of inadvertent nanotechnology throughout history. (a) Lustre and color effects caused by Cu and Ag nanoparticles in a piece of 16th century Italian pottery. (b) Cementite nanowires encapsulated by carbon nanotubes in Damascus Sabre.

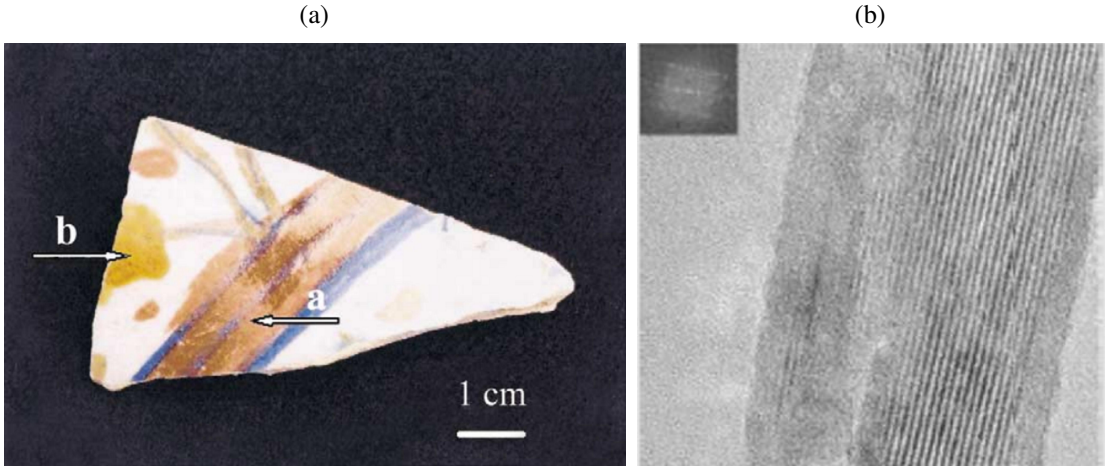

Source: adapted from (BORGIA et al., 2002) and (REIBOLD et al., 2006).

light (FARADAY, 1857). This work influenced later publications that would seek to rigorously perceive the behavior of light interacting with nanostructures, paving the way to the field of nano-optics. In the rising research fields of modern nanotechnology, a compelling subject with promising prospects is the topic of *plasmonics*. Such theme is related to the physical phenomenon of plasmon oscillations, where free electrons can sustain a damped resonant effect if excited at the proper wavelength. Even though ancient artisans, potters, ceramists and glass-blowers could not conceive what caused such colors and luster, their lack of understanding wasn't enough to avert the exploration of plasmonics in their craftsmanship. From the aforementioned examples of nanotechnology, the only in which plasmonics doesn't play a substantial role is in Damascus Sabre.

The physical effects related to plasmonic properties can be employed in a wide variety of fields and functionalities. Plasmonic phenomena offers good applicability, and plamonic driven nanomaterials have rendered various technologies in the last years. For instance, the local field enhancement resulting from localized plasmon resonance has been explored in fluorescence microscopy, where the use of a gold or silver nanoparticle sheet leads to an increase in the fluorescence quantum efficiency of a nearby fluorophore (CHEN; MUNECHIKA; GINGER, 2007; LI; LI; AROCA, 2017; USUKURA et al., 2017; MASUDA et al., 2017). The local field enhancement has also been used in plasmon-enhanced Raman spectroscopy, to either Surface Enhanced Raman Spectroscopy applications (ZHAO et al., 2014), as well as single molecule sensing in SERS plataforms (MAHDI; FARSINEZHAD; SHANKAR, 2017; ZONG et al., 2019). Plasmonic nanoparticles were also exploited in singlet oxygen generation (ZHANG et al., 2007; ZHANG et al., 2018) for applications in Photodynamic Therapy (DING et al., 2014; ZHOU et al., 2015).

The high dependency of the medium dispersion to localized plasmon resonance frequency makes the plasmonic peak shift caused by changing in the surrounding refractive index useful for sensing applications. Its employment in bio-sensing platforms has been investigated, and were used to identify the presence of the *Influenza* virus (PARK et al., 2012), as well as HIV-1 (LEE et al., 2013) and assess the occurrence of Zika-virus (TAKEMURA et al., 2019), Dengue (CAMARA et al., 2013) and *Candida Albicans* (NEVES et al., 2015; FAROOQ et al., 2018).

The high temperatures reachable by nanostructures supporting plasmon resonance under specific conditions can lead to the emergence of remarkable effects. One notable example is the capability of a nanodot in increasing the temperature of a solvent above its vaporization point. This effect is known as *superheating*, and can lead to advances in cancer treatment (CARLSON; GREEN; RICHARDSON, 2012; BAFFOU et al., 2014). The water surrounding the nanodot is superheated because homogeneous bubble nucleation is an activated process where a free energy barrier must be surmounted to convert liquid to vapor (CARLSON; GREEN; RICHARDSON, 2012). Micro-bubble formation is another effect that can similarly occur around nanodots. Here, the initial process is the same of superheating: the plasmonic effect is responsible for initial vaporization around the particle, but the presence of adsorbed gases in the solvent and the surface of nanoparticles induces diffusion of such gases, starting a nucleation process that leads to micro-bubble growth (BAFFOU et al., 2014). Moreover, plasmonic generated micro-bubbles were reported to induce cell perforation and cellular disruption (BOUTOPOULOS; BERGERON; MEUNIER, 2015).

Laser induced high temperatures are also capable of melting nanocrystals. Shape transformations are stimulated at relatively low fluences (μJ and mJ) by short and ultrashort pulses, melting or fragmenting nanorods back to spherical shape (LINK et al., 1999). The crystalline reorganization process has also been probed to better evaluate how this phenomenon takes place (LINK; WANG; EL-SAYED, 2000). More recently, studies showed that reshaping of single gold nanorods can be driven by thermal instability associated to its size. In this sense, below melting point reshaping can be achieved driven by surface diffusion (TAYLOR; SIDDIQUEE; CHON, 2014). There is still much to be understood in this phenomenon, and molecular dynamics simulations of Au clusters and nanoparticles were run to appraise the reshaping dynamics (WANG; TEITEL; DELLAGO, 2005; PETROVA et al., 2006; WANG; DELLAGO, 2003).

This work has as its main objective the evaluation of nanoheaters for high performance photothermal therapy (PTT). The optimization of heat generation in metallic nanoparticles for PTT applications is a prime element to achieve such objective, thus, a novel methodology for the optimization of metallic nanoparticles is described. The use of metallic nanoparticles in PTT enables temperature variations that can initiate cell death mechanisms in tumorous tissues. However, the heating of biological tissues in PTT for clinical applications is limited by safety and sanitary standards. For instance, renal excretion of nanoparticles and particle cytotoxicity are crucial issues that limits the administration of metallic nanoparticles for human cancer treatment.

The reduction of laser irradiation to safe fluence levels for skin exposure is also essential. For instance, laser exposition of human skin at 1064 nm is limited to 100 mJ/cm^2 for laser pulses shorter than 100 ns and 1 W/cm^2 for CW illumination (NIEMZ, 2007). The optimization of metallic nanoheaters plays an important role in the reduction of such fluences necessary to achieve effective temperature variation in tissues. The thermal evaluation of nanoheater performance may be accomplished by the employment of Thermal Lens technique. The characterization of colloidal solutions constituted by metallic nanoparticles may be performed more effectively by the use of Thermal Lens technique, in spite of thermocouples and thermal cameras to assess sample temperature dynamics.

1.1 OVERVIEW

This dissertation is organized in five distinct chapters that were systematically arranged to smoothly guide the reader across the developed work: Introduction, Thermoplasmonics, Nanoheater Optimization for Photothermal Therapy, Characterization of Metallic Nanoparticle Colloids by Thermal Lens Mesasurement and Conclusions.

The second chapter, *Thermoplasmonics*, discusses the optical and thermal properties of metallic nanoparticles, emphasizing gold nanostructures. Here, the importance of the Drude model for the description of metallic nanocrystal permittivities is shown. The tools to estimate optical cross sections of nanoparticles are also presented, and the Localized Surface Plasmon Resonance effect, as well as some of its dependencies are evaluated. Moreover, this chapter assess the heating of single metallic nanoparticles under pulsed and continuous light excitation regimes, providing figures of merit to quantify heating generation in each case.

Chapter 3 discloses a new methodology to engage in optimization of plasmonic nanostructures for high performance photothermal therapy. Gold nanorods are the nanoparticle morphology of interest, and optimization to both pulsed and continuous light excitation are appraised.

The use of Thermal Lens technique to estimate and characterize metallic nanoparticle colloids is suggested in chapter 4. Here, the collective heating of a nanoparticle ensemble is depicted and the localized heating of each individual nanoparticle is described as a function of the bulk temperature in the sample. The dual-beam mode-mismatched Thermal Lens technique is employed to measure bulk temperature variations at the pumped region of a colloidal solution of gold nanospheres. Thermal Lens is a technique that has seen widespread use to measure a variety of optical and thermal parameters of some transparent materials. However, it has never been directly employed to measure temperature. Advantages and limitations associated to temperature assessment by the thermal lens technique are highlighted.

The last chapter (*Conclusions and Future Prospects*) discusses and highlights the usefulness of the accomplished results and their applicability. Subsequent steps and future efforts to improve the disclosed techniques and outcomes are itemized as well. Two additional appendices

are included to supply further information about the techniques and tools not reported in the main body of this dissertation. For instance, *Appendix A* features the *Matlab* codes used to accomplish this work. Furthermore, *Appendix B* describes the basics of Finite-Element Method and features instructions to motivate the simulation of optical and thermal properties of metallic nanoparticles in *COMSOL Multiphysics*.

2 THERMOPLASMONICS

Thermoplasmonics is the field of nanoplasmonics that deals with heat generation by nanoparticle ensembles. In thermoplasmonics, the electric field damping caused by the localized plasmon resonance effect is explored in the heating of metallic nanoparticles and their surroundings, causing the nanoparticle to act as a nanoheater. Hence, the temperature increase at the nanoparticle surface and the temperature gradient in the nanoparticle neighbourhood become highly desirable.

Consequently, a good structure for thermoplasmonics must present high damping coefficients. In addition to that, high heat capacity and high melting points are advantageous, since they enable the nanoheater to exchange energy quickly with its surroundings while avoiding phase transitions. Many interesting effects take place during the heating of nanoensembles. Such thermal phenomena can be applied in various ways.

Among thermoplasmonics applications, its employment in life and biomedical sciences stands out. Photothermal Therapy, for instance, is a very promising technique that relies on nanoheaters to induce localized cellular necrosis and apoptosis with applications in cancer treatment (PATTANI et al., 2015; ZHANG et al., 2018; DOUGHTY et al., 2019). Cellular membrane disruption mediated by the formation of microbubbles in the vicinity of a nanoparticle is another localized effect that can be explored as cancer treatment (PRENTICE et al., 2005), although active matter control in microfluidic environments can also be achieved by bubble formation (JONES et al., 2019). As an inorganic example of thermoplasmonic usage, one can cite its role in nanofluids for solar collectors. Here, the nanoparticle acts as a mediator, absorbing sun light and releasing the energy to water as heat (HUSSEIN, 2015; JIN et al., 2020; MUHAMMAD et al., 2016). Nanoparticles can also be used as plasmonic nanothermometers, performing the task of measuring very localized temperature variations by detecting the blue-shifted anti-Stokes emission spectrum of the heated nanoparticle (CARATTINO; CALDAROLA; ORRIT, 2018).

In spite of thermoplasmonics not be restricted to the domain of metallic nanocrystals, metallic structures have thermal properties that are highly desirable for most, if not all the applications mentioned above. Therefore, this work will focus solely on the analysis of the optical and thermal properties of metallic nanoparticles, and primarily, gold nanocrystals.

2.1 OPTICAL PROPERTIES OF METALLIC NANOPARTICLES

2.1.1 Dielectric Function of Metallic Nanoparticles

The optical properties of metals can be explained by the model proposed by Paul Drude in 1900 (DRUDE, 1900). This model sought to explain the transport phenomenon of electrons in metals. At the time, it was only three years since the discovery of electrons by Thompson. The

atomic theory lacked the fundamental particles yet to be discovered in the following years and quantum theory had just been proposed by Planck the same year. Not much was understood about the microscopic properties of matter and how it collaborated to the behavior of bulk materials.

In this sense, Drude applied the kinetic theory of gases to metals, in which the conduction electrons were treated as a gas cloud and were to move in a static background of heavy ions. The main assumptions were that the Coulomb interaction among electrons (independent carriers) and between electrons and the background ions (unbounded/free electrons) were to be neglected. In the presence of external fields, the electrons move accordingly to Newton's laws of motion. This motion is to be damped by collisions between electrons and the static ions of the background (ASHCROFT; MERMIN, 2011).

This semi-classical approach yielded, among many outcomes, the permittivity of metals given by:

$$\epsilon(\omega) = 1 - \frac{\omega_p^2}{\omega^2 + j\gamma_0\omega} \ . \tag{2.1}$$

Here, $\omega_p = \sqrt{\frac{Ne^2}{\epsilon_0 m_e}}$ is the plasma frequency, with N representing the density of free-electrons, e the elementary charge, m_e the mass of the electron, ϵ_0 the vacuum permittivity, and γ_0 is the bulk damping parameter.

A quick inspection of equation 2.1 shows that frequencies bellow the plasma frequency will be absorbed by the metal, while it will be reflected for frequencies larger than the plasma frequency. To some metals, the plasma frequency occurs around the ultraviolet region, reflecting most of visible light and giving its shiny appearance. However, real metals are much more complex. In bulk gold, for instance, relativistic effects shifts the absorption to lower energies, falling from ultraviolet to visible range (PYYKKO; DESCLAUX, 1979).

While equation 2.1 accounts for intraband transitions, the interband transitions in metals (related to the bound electrons) are known to contribute to the dielectric function (BEVERSLUIS; BOUHELIER; NOVOTNY, 2003) and hence, have to be accounted for if one wants accurate results at higher energies (HERRERA et al., 2014). In gold, the interband transitions start to occur at λ = 516.6 nm, appearing yellow due to absorption of blue light (DERKACHOVA; KOLWAS; DEMCHENKO, 2016). A good way to represent the permittivity of bulk metals is to write it as:

$$\epsilon_{bulk}(\omega) = \epsilon_{inter}(\omega) + \epsilon_{intra}(\omega) \ , \tag{2.2}$$

with ϵ_{intra} and ϵ_{inter} being the the contribution of its intraband and interband transitions. In equation 2.1, the bulk damping parameter is proportional to the ratio between the Fermi velocity and the mean free path of the electron cloud ($\gamma_0 \propto \frac{v_F}{l_\infty}$). As the size of the metallic structure

decreases, the probability of collisions also diminishes, while collisions with nanoparticle surface increases. This is specially true in the nanometric regime, where the nanoparticle diameter has dimensions comparable to the mean free path of the conduction electrons. This aspect leads to the reduction of the mean free path and increase of the damping factor, causing the permittivity of metallic nanoparticles to be size dependent (ROSS; SCHATZ, 2015). Therefore, the damping parameter can be written as:

$$\gamma = \gamma_0 + A\frac{v_F}{L_{eff}} \ , \tag{2.3}$$

where the effective mean free path is $L_{eff} = 4V/S$ for convex shapes. Here, S is the nanoparticle surface area and V is the nanoparticle volume. If the nanoparticles are spherical, $L_{eff} = 4R/3$, R representing the radius of the nanoparticle. The parameter *A* describes the scattering at the surface of nanostructures or at the interface between materials at composite nanostructures. For spheres, *A* is usually considered to be equal to one (CORONADO; SCHATZ, 2003), while the surface scattering parameter for nanords lies between 0.25 and 0.5 (BERCIAUD et al., 2005; SöNNICHSEN et al., 2002).

To compute the size dependent permittivity of metallic nanoparticles, it is wise to utilize experimental permittivity data available for bulk metals in the literature to account for intraband and interband contributions in the spectral region of interest. After that, the size dependence is inserted in the equation by subtracting the term of Drude equation for γ_0 and adding the term with the modified damping factor γ instead. Therefore the size dependency of nanoparticle permittivity is given by:

$$\epsilon(\omega) = \epsilon_{bulk}(\omega) + \frac{\omega_p^2}{\omega^2 + j\omega\gamma_0} - \frac{\omega_p^2}{\omega^2 + j\omega\left(\gamma_0 + A\frac{v_F}{L_{eff}}\right)} \ . \tag{2.4}$$

Table 1 shows the values of each parameter of gold in equation 2.4. Together with the bulk gold permittivity provided by Johnson et al. (JOHNSON; CHRISTY, 1972), it is possible to evaluate the real and imaginary permittivity of gold nanospheres in the visible and near infrared regions.

Figures 3a and 3b show, respectively, the real and imaginary permittivities of gold nanospheres ranging from 5 to 50 nm in radius. One can notice that figure 3a presents negative values of real permittivity , while figure 3b displays that smaller particles have higher losses. The model derived in equation 2.4 however, is limited to nanostructures bigger than 5 nm. To smaller structures, quantum effects related to a reduced number of atoms in the crystal start to appear (KREIBIG; VOLLMER, 1995), and thus, the description of the crystal permittivity by means of the Drude model becomes inappropriate.

Table 1 – Nanoscopic and optical parameters of bulk gold.

Parameter	Value	Description
N	5.90×10^{28} m^{-3}	Electron density
ω_p	1.369×10^{16} rad/s	Plasma frequency
A	1	Surface scattering constant
v_F	1.4×10^{6} m/s	Fermi velocity
γ_0	1.07×10^{14} s^{-1}	Bulk damping factor

Source: belongs to the author.

Figure 3 – Size dependent permittivity of gold nanospheres. The bulk gold permittivity was taken from (JOHNSON; CHRISTY, 1972). (a) Re$\{\epsilon(\omega)\}$. (b) Im$\{\epsilon(\omega)\}$

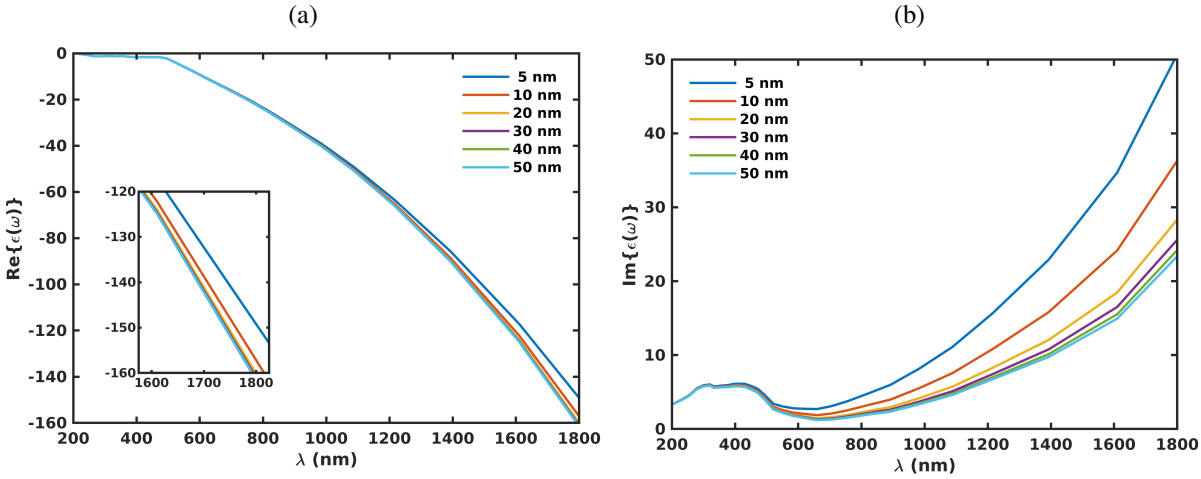

Source: belongs to the author.

2.1.2 Quasi-Static Approximation

A simple way of evaluating what is happening locally when light interacts with nanoparticles is by analyzing the simplest case possible. Due to symmetry, the easier geometry to be analyzed is a sphere. To make matters easier, suppose that the wavelength of incident light is considerably bigger than the sphere diameter d ($\lambda \gg d$). This makes the field interacting with the nanosphere to remain approximately uniform at specific moments, allowing the use of electrostatics techniques. This is the quasi-static approximation, depicted in figure 4. Solving the Laplace equation to a metallic sphere of radius a and permittivity ϵ under the influence of a static electric field of magnitude E_0 embedded in an infinite medium of permittivity ϵ_m, will lead to an internal (E_{in}) and external (E_{ext}) fields given by:

$$\vec{E}_{in} = -\left(\frac{3\epsilon_m}{\epsilon + 2\epsilon_m}\right) E_0 \hat{n}_z \ , \tag{2.5}$$

$$\vec{E}_{ext} = E_0\hat{n}_z + \left(\frac{\epsilon - \epsilon_m}{\epsilon + 2\epsilon_m}\right)\left(\frac{a^3}{r^3}\right)(2cos\theta\hat{n}_r + sin\theta\hat{n}_\theta)\ , \tag{2.6}$$

where *r* and θ are respective the radial and polar spherical coordinates.

Figure 4 – Depiction of the quasi-static approximation.

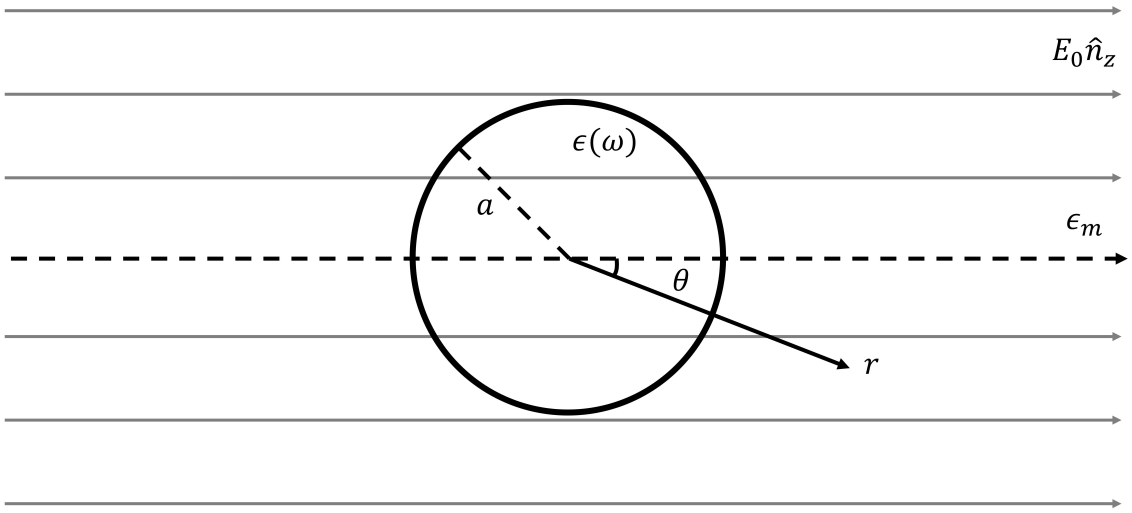

Source: belongs to the author.

The field homogeneity across the particle displaces the electron cloud, inducing a polarization. This polarization created by charge accumulation on the boundaries of the nanoparticle can be described by the dipolar moment $\vec{p} = \epsilon_0\epsilon_m\alpha_p\vec{E}_0$, where α_p, the polarizability, indicating the nanoparticle ability to form instantaneous dipoles. Within the nanoparticle, the electric field is rigorously zero in the static case, since it is cancelled out by the surface charges accumulated on its boundaries. This feature however, no longer holds under harmonic fields (BAFFOU, 2017). To the nanosphere, α_p is given by:

$$\alpha_p = 4\pi a^3\left(\frac{\epsilon - \epsilon_m}{\epsilon + 2\epsilon_m}\right)\ . \tag{2.7}$$

The charge separation due to polarization is responsible for a restoring force between the negative and positive charge centers in the nanosphere, driving the system to return to its original stable configuration. If excited at the proper frequency, this restoring force can be the origin of a resonance effect (BAFFOU, 2017). In fact, as seen in the previous section, the permittivity of metals is frequency dependent, which makes the polarizability of a metallic nanoparticle also frequency dependent. Under specific (resonance) conditions, very high electric field enhancement can be achieved inside and outside the nanoparticle.

2.1.3 Mie Theory

Following the Faraday comments on the behavior of incident light on gold thin films (FARADAY, 1857), Gustav Mie derived a rigorous electromagnetic treatise on the interaction of light with metallic spherical nanoparticles (MIE, 1908). Mie theory differs from the quasi-static approximation by analyzing an incident plane wave, a truly harmonic field, instead of the time-static electric field approximation. Due to the nature of the problem, Mie theory imposes a more complex, but at the same time a more robust tool for plasmonic analysis, yielding results compatible with experimental data.

In its essence, Mie theory deals with the absorption and the scattering of plane electromagnetic waves by uniform isotropic particles embedded in an infinite dispersive medium, that is also isotropic and uniform. It follows that the scattering cross-section and the extinction cross section are respectively given by (BOHREN; HUFFMAN, 1983):

$$\sigma_{sca} = \frac{2\pi}{k^2}\sum_{n=1}^{\infty}(2n+1)(|a_n|^2 + |b_n|^2) \ , \tag{2.8}$$

and

$$\sigma_{ext} = \frac{2\pi}{k^2}\sum_{n=1}^{\infty}(2n+1)Re(|a_n|^2 + |b_n|^2) \ , \tag{2.9}$$

In equations 2.8 and 2.9, *k* is the wavenumber of incident light. Also,

$$a_n = \frac{m_r\psi_n(m_r x)\psi'_n(x) - \psi_n(x)\psi'_n(m_r x)}{m_r\psi_n(m_r x)\xi'_n(x) - \xi_n(x)\psi'_n(m_r x)} \ , \tag{2.10}$$

$$b_n = \frac{\psi_n(m_r x)\psi'_n(x) - m_r\psi_n(x)\psi'_n(m_r x)}{\psi_n(m_r x)\xi'_n(x) - m_r\xi_n(x)\psi'_n(m_r x)} \ , \tag{2.11}$$

with $\psi_n(x)$ and $\xi_n(x)$ the Riccati-Bessel functions with $x = k_m r$. Here, *r* is the nanosphere radius and m_r is the ratio between the complex refractive index of the nanoparticle and the refractive index of the medium. The absorption cross section can be obtained by simply subtracting the scattering cross section from the extinction cross section, as:

$$\sigma_{abs} = \sigma_{ext} - \sigma_{sca} \ . \tag{2.12}$$

The power series expansion in terms of *n* represents the resonant modes of the nanoparticle. The dipole is represented by $n = 1$, the quadrupole by $n = 2$, and so on. Higher order

modes are associated to higher energies and bigger particles. As the excitation energy or particle size increases, higher order modes become more important. Figures 5a, 5b and 5c illustrate respectively the dipolar (n = 1), quadripolar (n = 2) and sextupolar (n = 3) resonant electric modes in an active $SiO_2 - Ag$ core-shell nanocrystal.

Figure 5 – Normalized E-field modes for an active $SiO_2 - Ag$ core-shell nanocrystal. (a) Dipolar (n = 1), (b) quadrupolar (n = 2) and (c) sextupolar (n = 3).

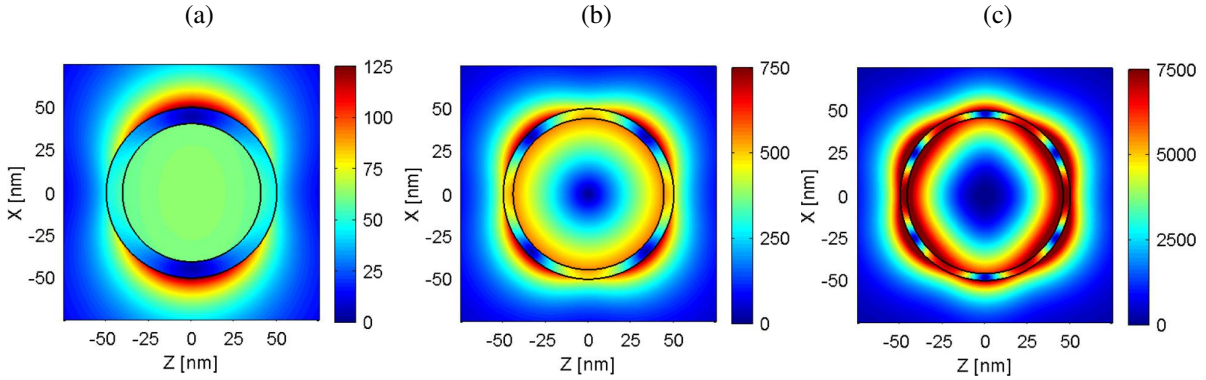

Source: adapted from (LIBERAL et al., 2014).

To particles typically smaller than 30 nm in diameter, only the lowest order contributions are considered. This is equivalent to set a_n, and b_n to zero, except for b_1. This reduces the cross sections to what is known as the Rayleigh approximation. Thus:

$$\sigma_{ext} = k\ Im(\alpha_p)\ , \tag{2.13}$$

$$\sigma_{sca} = \frac{k^4}{6\pi}|\alpha_p|^2\ . \tag{2.14}$$

However, equation 2.13 is accurate only if scattering is much smaller than absorption (BOHREN; HUFFMAN, 1983). Therefore:

$$\sigma_{abs} \approx k\ Im(\alpha_p) \tag{2.15}$$

The validity of the Rayleigh approximation in nanoparticle resonance gives a dipole-like radiation pattern to its scattered fields. As higher modes of oscillation gain more importance, the radiation pattern of their scattered fields becomes more pronounced in certain directions, giving the known forward scattering characteristic that is commonly associated with Mie Theory. This high directivity of scatterd fields can be explored to trap light and increase solar cell efficiency. Also, the lithographic arrangement of nanoparticles arrays over a substrate provides high directivity to such applications (MAITY; ROY, 2013; DEKA et al., 2018).

2.1.4 Localized Surface Plasmon Resonance (LSPR)

To obtain the cross section approximations by means of an electrodynamics approach, one can insert equation 2.7 in the equations 2.14 and 2.15. Representing the complex dielectric function of metals as $\epsilon = \epsilon' + j\epsilon''$, after some algebraic manipulations, one finds that:

$$\sigma_{sca} = \frac{8\pi}{3} a^6 k^4 \frac{(\epsilon' - \epsilon_m)^2 + \epsilon''^2}{(\epsilon' + 2\epsilon_m)^2 + \epsilon''^2} \ , \tag{2.16}$$

$$\sigma_{abs} = k \frac{3\epsilon_m \epsilon''}{(\epsilon' + 2\epsilon_m)^2 + \epsilon''^2} \ , \tag{2.17}$$

By adding equations 2.16 and 2.17, the extinction cross section for spherical nanoparticles can be written as (KUMAR, 2013):

$$\sigma_{ext} = \frac{24\pi^2 a^3 \epsilon_m^{3/2}}{\lambda} \frac{\epsilon''}{(\epsilon' + 2\epsilon_m)^2 + \epsilon''^2} \tag{2.18}$$

The above equations (2.16, 2.17 and 2.18) indicate that all cross sections increase considerably, reaching a peak value when the denominator goes to zero, i.e., $(\epsilon' + 2\epsilon_m)^2 + \epsilon''^2 = 0$. This is known as the Frohlich condition. This condition states that real part of the nanosphere permittivity must be negative $\epsilon' = -2\epsilon_m$, at the same time that ϵ'' must be small. If the Frohlich condition is met, a forced oscillation of the conduction electrons is sustained, giving rise to the Localized Surface Plasmon Resonance (LSPR) (KUMAR, 2013). Figure 6 illustrates the LSPR phenomenon. Figure 7 shows the difference between non-resonant and resonant (Frohlich) conditions in the illumination of a single gold nanosphere embedded in water. The LSPR properties are dependent on three main parameters that are going to be addressed: material, shape and size.

Figure 6 – Excitation of LSPR.

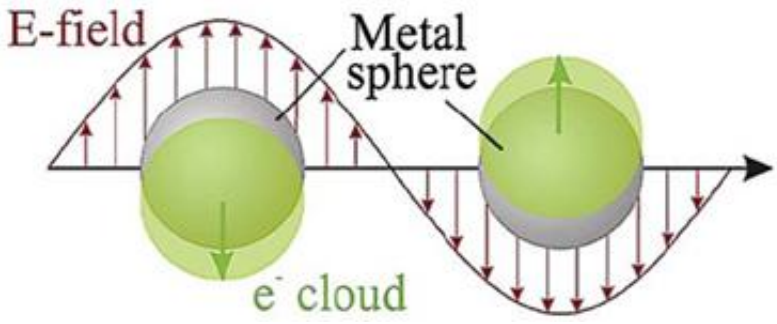

Source: adapted from (KELLY et al., 2003).

Figure 7 – Comparison of the electric-field around a spherical nanoparticle at non-resonant and Frohlich conditions. The color bar represents the magnitude of electric-field enhancement around the nanosphere. (a) Electric-field at off resonance wavelength. (b) Field enhancement at resonant condition.

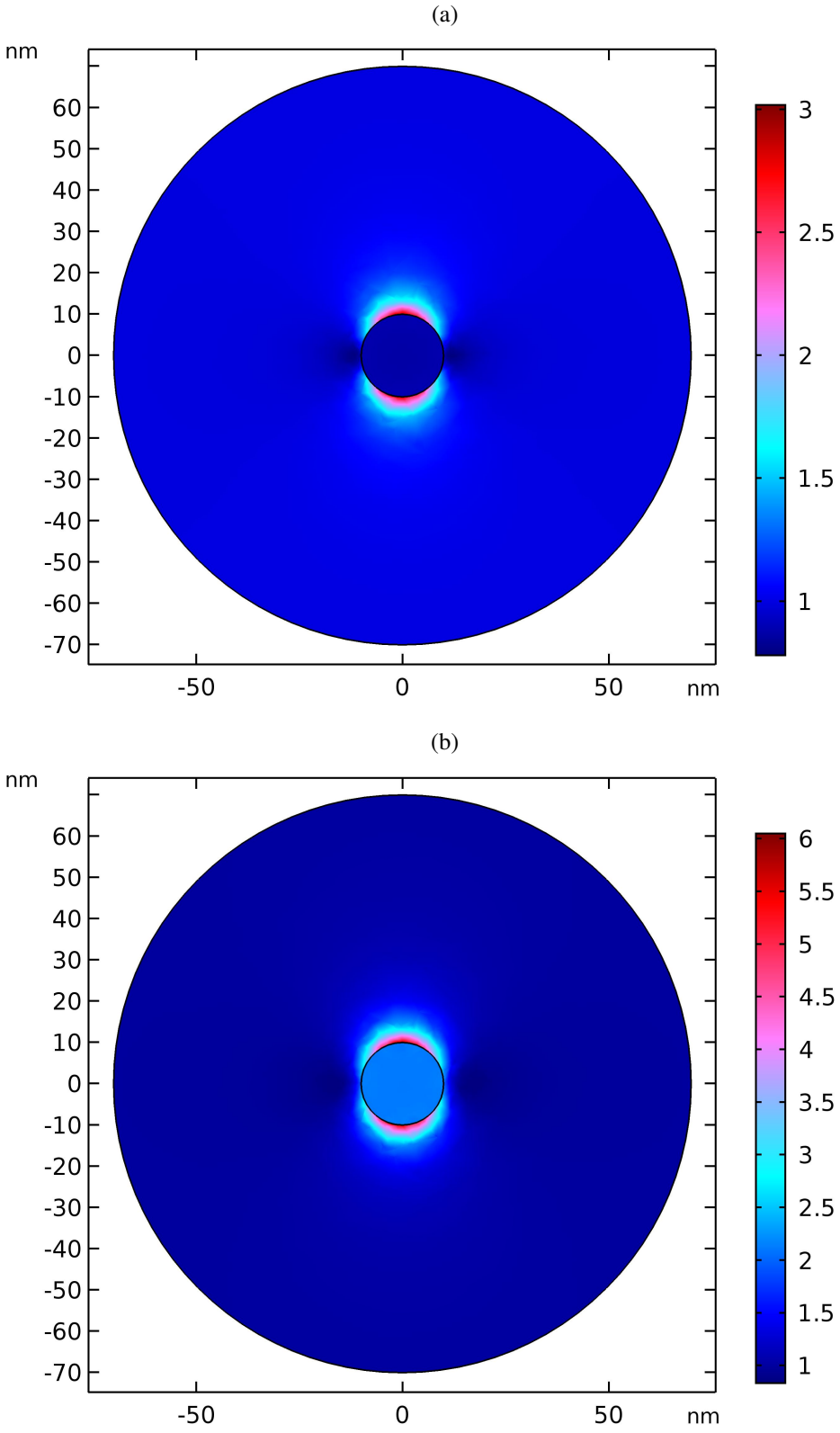

Source: belongs to the author.

2.1.4.1 Material Dependence

Plasmonic properties are highly dependent on material type, since the complex permittivity changes to each element. In order to achieve LSPRs in the visible region, a material with high density of carriers is required. Noble metals such as Cu, Ag and Au constitutes the most commonly studied plasmonic materials. Non-noble metals, such as Pb and Al, present LSPR frequencies in the UV region of the spectrum (BAFFOU, 2017; ROSS; SCHATZ, 2015). These nanoparticles display broader LSPR bands that can be explored in the energy harvesting of light sources with broad spectral response, such as the sun. Due to it's chemical instability, they are also prone to oxidation. Doped semiconductor nanoparticles are promising structures for thermoplasmonic applications, since they present higher thermochemical stability (THAKORE et al., 2018). The active medium provided by doped semiconductor crystals may also be explored in more sophisticated applications. Typically, LSPR of doped semiconductors nanoparticles occur in the infrared. In this case, carrier densities of 10^{25} to 10^{28} m^{-3} are required (KUMAR, 2013). Figure 8 shows the carrier density dependency of LSPR and it spectral regions.

Figure 8 – Carrier density dependency of LSPR and it spectral regions.

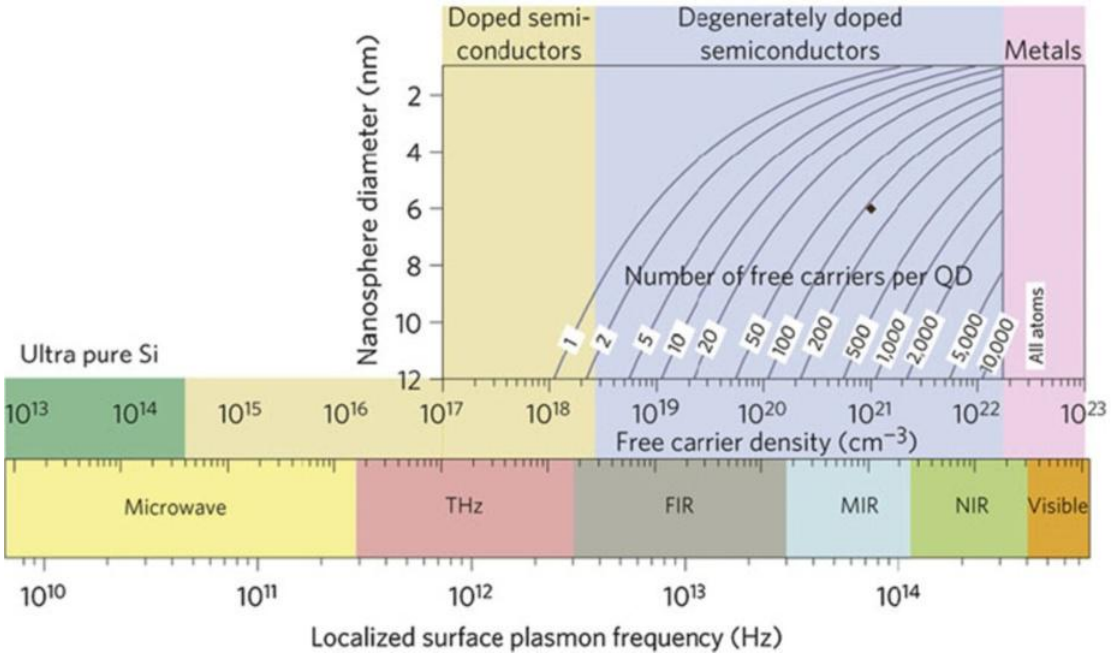

Source: (KUMAR, 2013).

To better illustrate the material dependence of LSPR, the figure 9a shows the difference between the real relative permittivity of Au and Ag. The negative values at which both real permittivities becomes -2 (see equation 2.17) demonstrates the different wavelengths at which LSPR occurs to Ag and Au. Figure 9b shows the absorption cross section of 20 nm Au and Ag nanospheres in water occurring at different wavelengths due to Frohlich condition.

Figure 9 – Material dependence of LSPR. (a) Real permittivity of Ag and Au in the visible region and its Frohlich conditions. (b) Absorption cross section of 20 nm Au and Ag nanospheres in water.

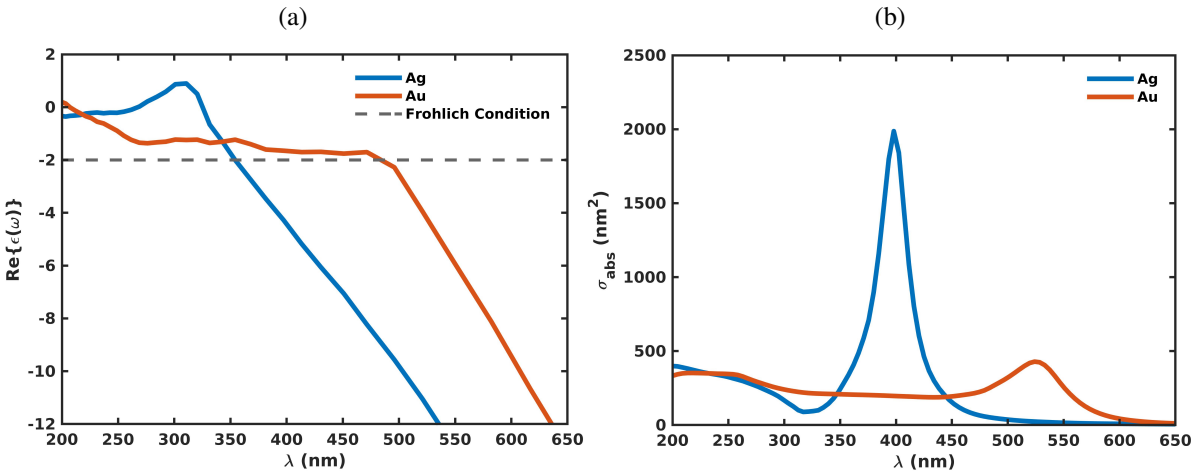

Source: belongs to the author.

2.1.4.2 Shape Dependence

Nanoparticle morphology is another factor that comes into place when evaluating plasmonic properties. Many geometries have been synthesized in the most diversity of shape. For instance, nanocubes (ZHAO et al., 2019; CLARK et al., 2019; YIN et al., 2019; STEWART et al., 2019; SHERRY et al., 2005; JEON; TSALU; HA, 2019), nanocages (ZHAO et al., 2019; GENÇ et al., 2016), nanoprisms (FRANK et al., 2010; HABER; SOKOLOV, 2017), nanorods (ZHUO et al., 2019; CHEN et al., 2013; GUTIÉRREZ; SCARPETTINI, 2019; BECKER et al., 2010), nanodisks (VERRE et al., 2019; ZORIĆ et al., 2011), and nanoshells (LAL et al., 2002; RADLOFF; HALAS, 2004; HUANG et al., 2017) have been tried and explored in various applications recently. Figure 10 illustrates some of the shapes that are possible to be obtained. Those shapes are normally synthesized by chemical methods. High shape control can be obtained by lithographic techniques, although it limits the nanocrystals to be attached to a substrate (TRAN; NGUYEN, 2017).

Figure 10 – Examples of different nanoparticle morphologies.

Source: adapted from (BOLAÑOS; KOGAN; ARAYA, 2019).

Such structures allow the control of absorption and scattering contributions to plasmon spectrum due to their anisotropy. In those cases, different resonant modes can be excited, shifting

LSPR wavelength. Plasmon peak shift behavior is displayed in figure 11.

Figure 11 – LSPR shift due to morphology differences in Ag nanoparticles.

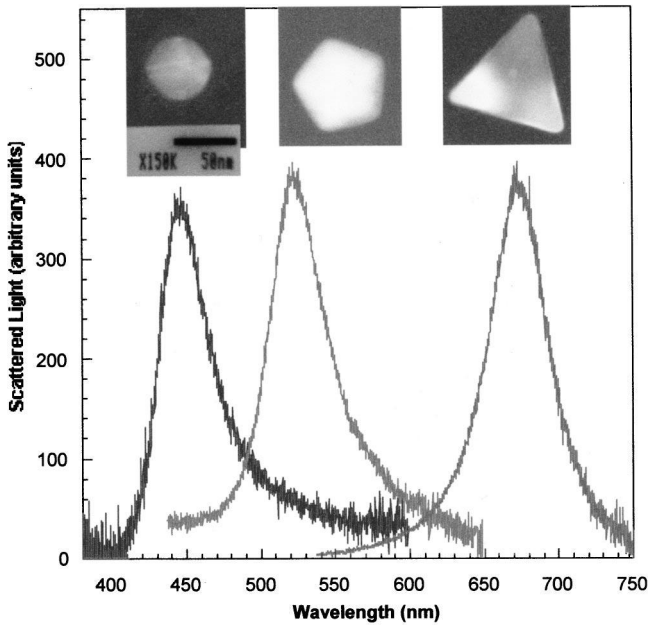

Source: adapted from (MOCK et al., 2002).

2.1.4.3 Size Dependence

As the size of a nanoparticle changes, it plasmon peak shifts. As the particle grows bigger, it cannot be effectively approximated by a dipole anymore. The non-homogeneity of the electric field acting in the nanoparticle induces dephasing to the oscillating electrons, creating a retardation effect. This causes a broadening and red-shift in plasmon peak (BAFFOU, 2017). Also, higher order oscillation modes of the electronic cloud becomes more significant (LINK; EL-SAYED, 2000).

2.1.4.4 Plasmonic Properties of Nanorods

In some cases, a new resonant mode arises due to anisotropy in nanoparticle shape. This is specially true for nanorods, where their size is directly related to its longitudinal mode LSPR tunability (ZULOAGA; PRODAN; NORDLANDER, 2010). The fact that matallic nanorods can present LSPR in the near infrared region when compared to a nanosphere with same volume, makes them exceptionally desirable in biomedical (STONE; JACKSON; WRIGHT, 2010; LOCATELLI; MONACO; FRANCHINI, 2015; JUSTE et al., 2005) and imaging (MA et al., 2013) applications. Figure 12 shows the shift in LSPR to a Au nanosphere and Au nanorod of same volume. It is remarkable the enhancement in absorption caused by change in morphology. The tunability of a nanorod is a function of its aspect ratio (AR). The AR is defined by the ratio of nanorod length to width. The LSPR position red-shifts in direct proportion of its AR, as exhibited by figure 13.

Figure 12 – Absorption spectrum of Au nanosphere (red dotted line) and nanorod of same volume (solid blue line).

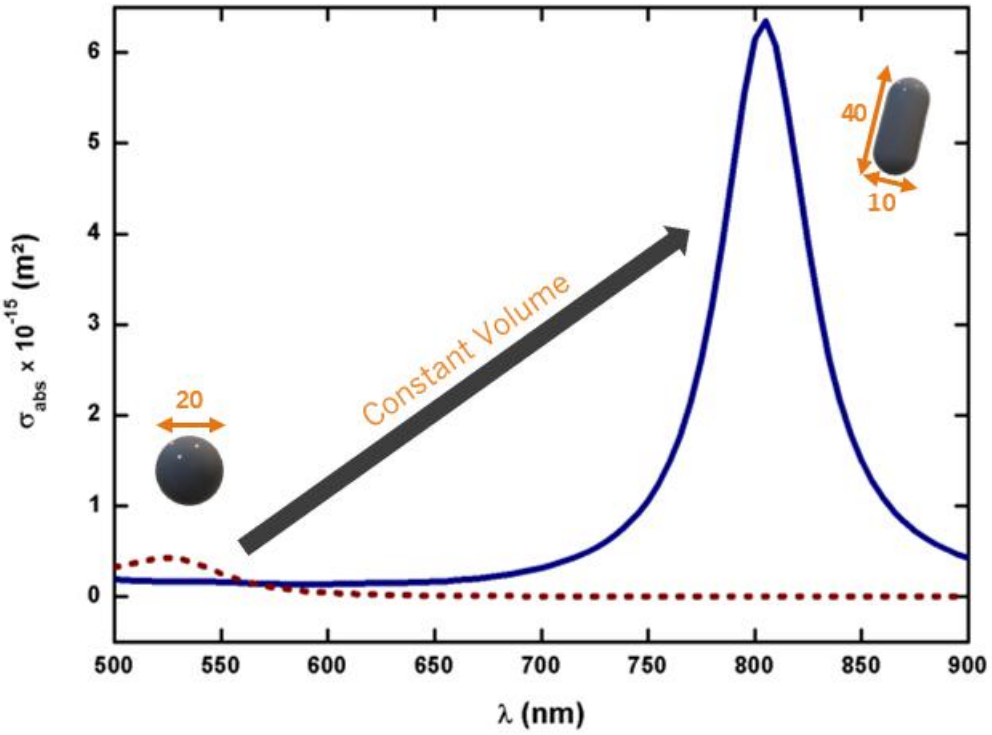

Source: belongs to the author.

Figure 13 – Absorption spectra of Au nanorods for several ARs and different volumes.

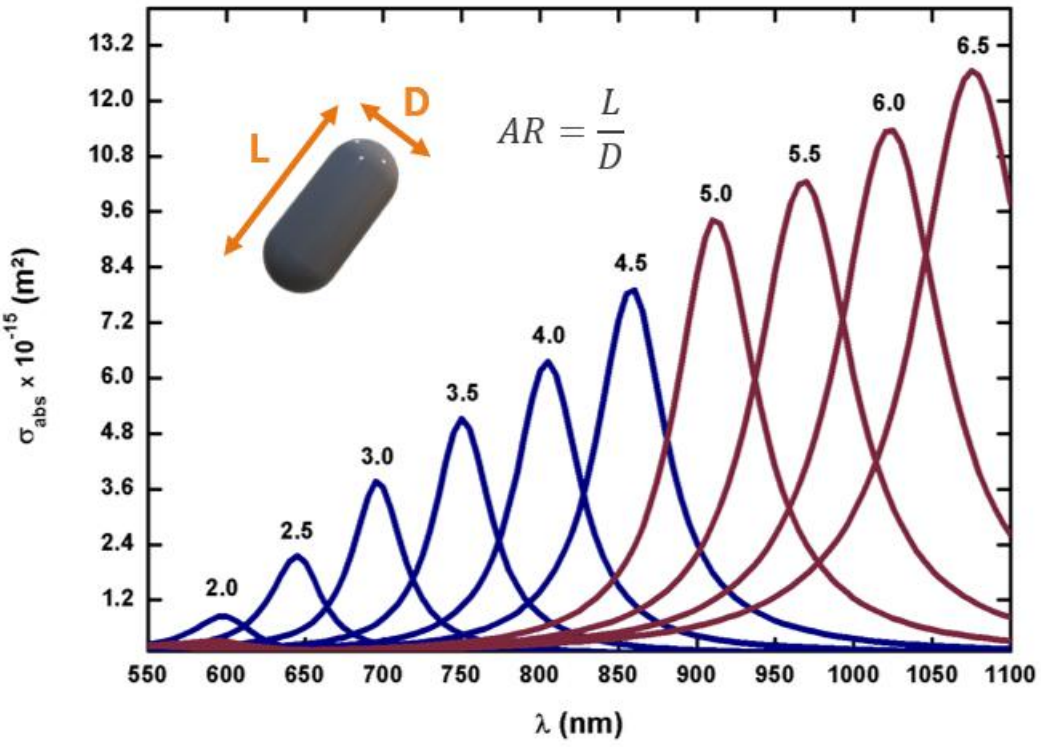

Source: belongs to the author.

2.2 THERMAL PROPERTIES OF METALLIC NANOPARTICLES

As mentioned before, nanoparticles must present good electric properties in order to be employed in heat generation. Heat is generated by the light energy absorbed by the nanoparticle. This process is know as photothermal conversion. An efficient nanoheater must, then, have good thermal characteristics with supporting LSPR modes. Metallic nanoparticles fall into this category, showing good thermal and optical coefficients. After illumination, the conduction electrons of a metallic nanoparticle oscillate in response to the incident excitation field, with the same frequency. The oscillation of this electron cloud inside the nanoparticle is, therefore, an electric current. This current dissipates energy via Joule effect (BAFFOU, 2017), giving rise to a heat power density within the nanoparticle given by

$$q(\vec{r}) = \frac{1}{2}\omega\epsilon_0 Im\{\epsilon(\omega)\}\left|\vec{E}(\vec{r})\right|^2 , \tag{2.19}$$

where ω is the angular frequency of oscillation, $\epsilon(\omega)$ is the frequency dependent complex permittivity of the metal and $\vec{r}$ is the position vector of a location inside the nanoparticle. The total heat power delivered by a nanoparticle can be obtained by integrating equation 2.19 in the spatial domain of the nanostructure. Therefore, the total heat power, P_{abs}, can be written as:

$$P_{abs} = \frac{1}{2}\omega\epsilon_0 Im\{\epsilon(\omega)\}\int_V dV\left|\vec{E}(\vec{r})\right|^2 . \tag{2.20}$$

The heat power density is proportional to the square of the electric field, i.e, is proportional to the intensity of incident light. Equation 2.20 can also be written as $P_{abs} = \sigma_{abs} I$, where *I* is the intensity of the excitation source. This allows the above solutions to be used by arbitrarily shaped nanoparticles. It also enables the determination of optical cross sections by computational methods, such as Discrete Dipole Approximation (DDA) (XU et al., 2012) and Finite Element Method (FEM) (please refer to Appendix B) to be used in thermoplasmonic simulations.

To quantify the nanoparticle performance as a nanoheater, the figure of merit that is most widespread in literature is the Photothermal Conversion Efficiency (η) (ABADEER; MURPHY, 2016), that is defined as the ratio of absorption cross section to extinction cross section:

$$\eta = \frac{\sigma_{abs}}{\sigma_{ext}} = \frac{\sigma_{abs}}{\sigma_{sca} + \sigma_{abs}} . \tag{2.21}$$

A quick inspection of equation 2.21 shows that η quantifies only the percentage of the incident EM field absorbed by the nanostructure. It is readily known that small particles presents very efficient coupling of light, absorbing almost all energy with barely any scattering when illuminated by a plane wave. As the particle grows bigger, both the absorption and scattering

increase, until they reach a threshold where scattering starts to command the interaction. Higher absorption by itself doesn't necessarily means better heat delivery. The ability of a particle to lose heat to its surroundings is related to its surface area and volume. To grant efficient heat loss, the volume must be minimized while surface area maximized. That's where particle morphology becomes relevant on thermoplamonics.

2.2.1 Timescales of Photothermal Phenomena

To better understand the heat delivery of excited nanoparticles, one must comprehend from a solid-state stand point how heat is generated and how long it takes to the generated heat start being transferred to the surroundings. Figure 14 illustrates the timescale of photothermal generation and the Fermi-Dirac distribution of metallic nanoparticles during the process.

Figure 14 – Timescale of photothermal phenomena (upper panels) and F-D distribution of each step (lower panels).

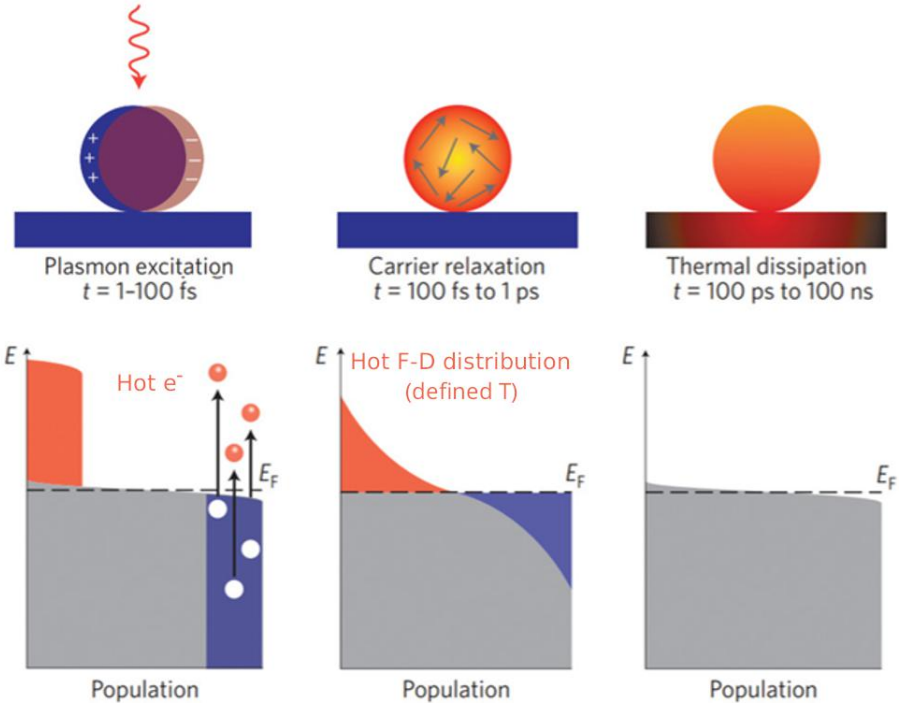

Source: adapted from (BRONGERSMA; HALAS; NORDLANDER, 2015).

When radiation strikes a metallic nanocrystal at the right wavelength and stimulates the LSPR effect, the electron cloud gain enough energy to promote some electrons from a lower energy level to an excited state above the Fermi level, changing the population distribution and leaving holes that are readily occupied by the high density of electrons in the conduction band of the metal. The excited conduction electrons will collide among themselves until they are thermalized. This electron-electron scattering is completely elastic, i.e., the total kinetic energy of the excited carriers remains constant throughout the process. This promotion and thermalization of carriers takes from 1 to 100 fs to occur.

After that, the electrons in the hot F-D distribution start to suffer relaxation by interacting to the lattice of the nanoparticle. This carrier relaxation takes from 100 fs to 1 ps, and the Fermi-Dirac distribution starts to gradually retreat back to a lower temperature state. From 100 ps to the nanosecond scale, thermal dissipation to the surroundings starts to take place, and the nanoparticle starts to lose heat. The processes of thermal dissipation in nanometric scales are the same as the macroscopic case. The thermalization time associated to the thermal conductivity of a typical system of size *d* and thermal diffusivity D_{th} is given by (GOVOROV et al., 2006)

$$\tau \sim \frac{d^2}{D_{th}}. \tag{2.22}$$

To a spherical region containing water with a typical radius of 20 μm, the thermalization time is on the order 3 ms.

2.2.2 Single Nanoparticle Heating under Nanosecond Pulse Excitation

From our previous discussion, one can state that after some nanoseconds from the beginning of plasmonic excitation, all the absorbed energy is stored in the nanoparticle. Moreover, the high thermal conductivity of metals compared to the surrounding materials (usually solvents) allows the consideration that the nanoparticle is an homogeneous heat source. Particle with dimensions in the order of tens of nanometers presents thermalization constants in the order of a few nanoseconds. Figure 15 shows the simulation of a 20 ns excitation pulse with 9 GW/m^2 peak intensity of a gold nanosphere and its thermal response. The pulse was capable of inducing a 20 ^{o}C temperature variation in the nanosphere. Notice the delay between optical excitation and thermal response, and the slow thermal decay due to heat transfer to the surrounding volume.

Figure 15 – Nanosecond pulse excitation and thermal response of single Au nanosphere in water.

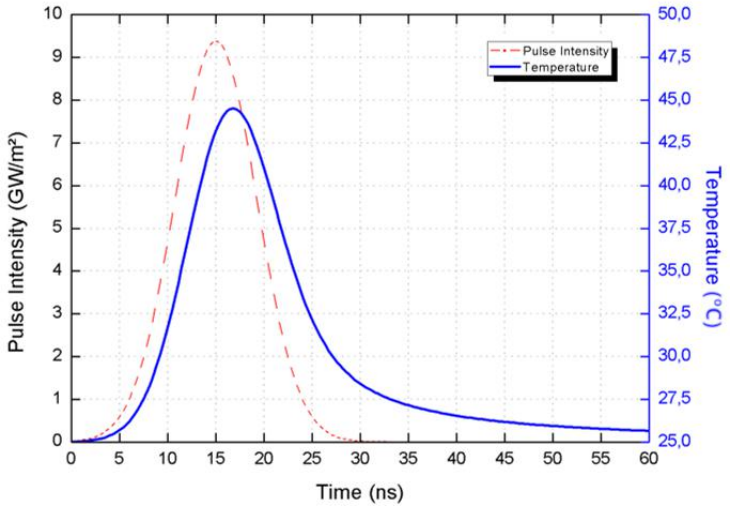

Source: belongs to the author.

For timescales smaller than thermalization time τ, no transport effects are involved on heating the external environment. In nanoparticle heating by pulses with timewidth in the order of τ or shorter, it is possible to safely assume that all the energy absorbed by the nanoparticle will be employed to elevate its temperature, as long as no phase transitions are involved. The energy absorbed by the nanoparticle is given by

$$Q = MC_p\Delta T_{np} = \rho V C_p \Delta T_{np} \ . \tag{2.23}$$

In equation 2.23, *M* is the mass of the nanoparticle, ρ is nanoparticle density, *V* is its volume, C_p is it specific heat, and ΔT_{np} is the temperature variation induced by the nanosecond pulse. Moreover, the energy absorbed by the irradiated nanoparticle can be written as $Q = \sigma_{abs} \int_0^t I(t')dt'$. Thus:

$$\sigma_{abs} \int_0^t I(t')dt' = \rho V C_p \Delta T_{np} \ . \tag{2.24}$$

Rearranging the equation 2.24, it is possible to notice that the temperature variation in the nanoparticle is:

$$\Delta T_{np} = \frac{1}{\rho C_p} \int_0^t I(t')dt' \left(\frac{\sigma_{abs}}{V}\right) \ . \tag{2.25}$$

The temperature variation is directly proportional to the ratio of its absorption cross section to volume.

2.2.2.1 Figure of Merit for Nanosecond Heating: the Joule Number

A way to evaluate the performance of thermoplasmonic structures is by exploring figures of merit. Photothermal Conversion Efficiency, as described before, is an example of figure of merit for thermoplasmonics. Quality Factor and Faraday Number are two more figure of merits examples of that measure respectively spectra linewidth and the field enhancement of a nanostructure (BAFFOU, 2017). Each figure of merit, however, measures a specific characteristic of nanostructes, and not necessarily will be effective to evaluate different parameters. For instance, the Faraday Number is pretty much useless to measure thermoplasmonic capabilities, while η provides inconclusive data.

An effective way of evaluating the ability of nanoparticles to generate heat is the Joule Number (LALISSE et al., 2015), a dimensionless number named after the Joule Effect. By

definition:

$$J_0 = \frac{e\epsilon''}{\sqrt{\epsilon_m}} \left| \frac{\vec{E}_{in}}{\vec{E}_0} \right|^2 , \tag{2.26}$$

where *e* is the ratio of the wavelength equivalent to 1 eV (1240 nm) to the excitation wavelength, $\vec{E}_{in}$ is the internal electric field of the nanoparticle and $\vec{E}_0$ is the incident field. It also can be written as (LALISSE et al., 2015):

$$J_0 = \frac{\lambda_{ref}}{2\pi} \left(\frac{\sigma_{abs}}{V} \right) . \tag{2.27}$$

Here, $\lambda_{ref} \approx 1240$ nm. Comparing equations 2.25 and 2.27, one can see that $\Delta T_{np} \propto J_0$ and, hence, the Joule Number presents itself as a good figure of merit for nanoheater optimization to short pulse applications.

2.2.3 Single Nanoparticle Heating under Continuous Excitation

For excitation times longer then the thermalization constant τ, condutive transport of heat must be taken into account to accurately predict the thermal response of nanostructures. In such cases, the Laplace equation given by:

$$\rho C_p \frac{\partial T(\vec{r},t)}{\partial t} = \kappa \nabla^2 T(\vec{r},t) + q(\vec{r},t) , \tag{2.28}$$

must be solved. In equation 2.28, ρ, C and κ are respectively the density, specific heat and thermal conductivity. In the absence of phase transformations, and considering the single particle a continuous source of energy, the solution of equation 2.28 is known for a spherical nanoparticle of radius *a* (PITSILLIDES et al., 2003). The dynamic heating is relatively fast, which makes the nanoparticle reach half of its maximum temperature in the characteristic thermalization time of the nanoparticle τ_{np}. For times bigger than τ_{np}, the spatial and temporal dependency of the temperature outside the nanoparticle can be described by (GOVOROV et al., 2006):

$$T(r,t) - T_\infty = \frac{P_{abs}}{4\pi\kappa_m r} \left(1 - \frac{1}{\sqrt{\pi t/\tau_m}} \right) , \qquad r \geqslant a \tag{2.29}$$

with κ_m and τ_m being respectively the thermal conductivity and the thermalization constant of the medium, $P_{abs} = \sigma_{abs} I$ is the power absorbed by the structure and T_∞ is the temperature far away from the nanoparticle, i.e., the initial temperature of the system. Thus, equation 2.29

describes the system spatiotemporal temperature variation. For times $t \to \infty$ or $t \gg \tau_m$, the solution of the Laplace equation reaches the steady-state (KEBLINSKI et al., 2006), and the maximum temperature of the nanoparticle at the interface ($r = a$) becomes

$$\Delta T_{np} = \frac{\sigma_{abs} I}{4\pi\kappa_m a} \, . \tag{2.30}$$

To better illustrate the temporal behavior of temperature rise at the nanoparticle interface, figure 16 shows the exact, the approximated solutions and the steady-state value of equation 2.28 to $P_{abs} = 35$ W/cm^2, $I = 4 \times 10^{-14}$ m^2, $\kappa_m = 0.3$ W m^{-1}K^{-1} and $a = 65$ nm (KEBLINSKI et al., 2006). According to the figure, both the approximate and exact solutions exhibit fast heating in the first 100 ns and approach asymptotically the steady-state temperature of 0.06 K (KEBLINSKI et al., 2006). The small value of temperature variation obtained will be discussed in a further chapter.

Figure 16 – Surface temperature during transient heating of a single nanoparticle.

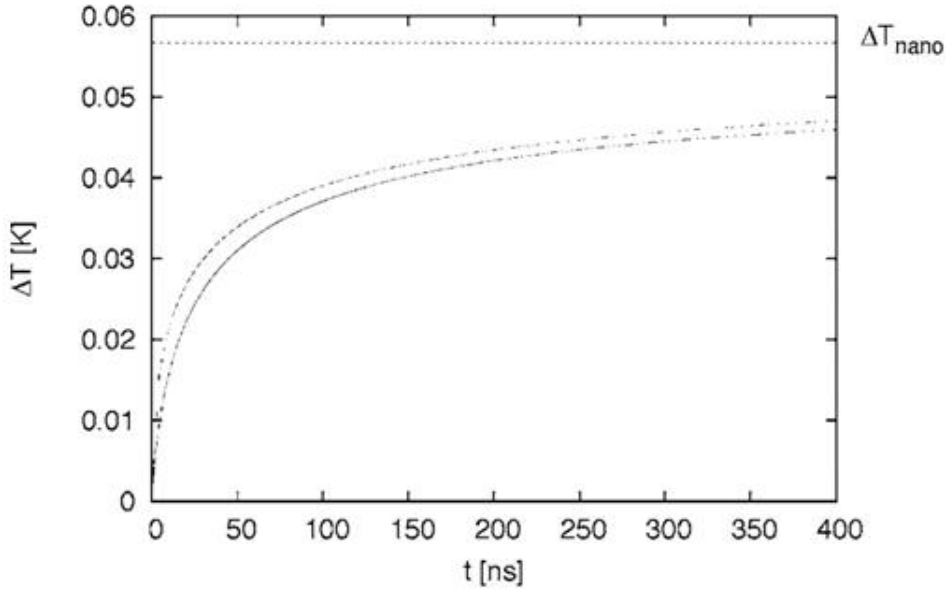

Source: (KEBLINSKI et al., 2006).

2.2.3.1 Figure of Merit for Continuous Heating: the Steady-State Factor

Equations 2.29 and 2.30 describe the dynamics of temperature variation for a spherical nanoparticle embedded in an arbitrary medium. Although these approximations acurately elucidate the thermal behavior of a sphere, they cannot be employed in different nanoparticle shapes. Despite equation 2.28 being well suited for the calculation of any arbitrarily shaped nanosctructure, it may not be possible to obtain the analytical solution for shapes other than the sphere. Approximations for highly symmetrical shapes may be obtained by onerous power series expansions and by computation techniques, but it is somewhat impractical.

The morphology of a nanostructure plays an important role in how it loses energy to its surroundings. The ability to lose heat to external bodies is related to the surface area of the nanostructure, and thus, a higher surface area allows for more efficient conduction of heat outwards. This means that particle morphology defines how fast a shape loses heat in comparison to another. To overcome this difference, an electrostatics analogy can be drawn. To better elucidate the problem, a thermal capacitance can be defined as the ratio between the power absorbed by a nanoparticle and the thermal variation caused by such absorption (BAFFOU; QUIDANT; ABAJO, 2010). Therefore:

$$C_{th} = \frac{P_{abs}}{\Delta T_{np}} \ . \tag{2.31}$$

One can notice that if a particle loses heat quickly to its surroundings, the temperature variation caused by a constant absorbed power is smaller, changing the thermal capacitance. Due to this fact, each nanoparticle shape will present a different thermal capacitance. For a sphere, the thermal capacitance is given by $C_{th}^{sphere} = 4\pi\kappa_m a$ (BAFFOU; QUIDANT; ABAJO, 2010). For non-spherical shapes, the thermal capacitance can be calculated by treating the nanostructure as an equivalent sphere of same volume as the particle with equivalent radius R_{eq}. A dimensionless thermal-capacitance coefficient β is considered to compensate the differences in shape. Then, the thermal capacitance becomes $C_{th} = 4\pi\kappa_m R_{eq}\beta$, and the temperature increase (equation 2.30) can be written as:

$$\Delta T_{np} = \frac{I}{4\pi\kappa_m}\frac{\sigma_{abs}}{R_{eq}\beta} \ . \tag{2.32}$$

Equation 2.32 (BAFFOU; QUIDANT; ABAJO, 2010) shows a clear dependency on particle properties ($\Delta T_{np} \propto \sigma_{abs}/R_{eq}\beta$). The shape factor β, the absorption cross section and the equivalent radius are all a function of nanoparticle shape, and changing its dimensions may increase or reduce the steady-state temperature that a particle can reach. For nanospheres, $\beta = 1$, while for nanorods $\beta \approx 1 + 0.096587\, ln^2(AR)$ (BAFFOU, 2017; BAFFOU; QUIDANT; ABAJO, 2010). Reference (BAFFOU; QUIDANT; ABAJO, 2010) carries a mistake in the β attributed to nanorods. Such inconsistency was rectified in (BAFFOU, 2017). Therefore, a good metric for steady-state heating, the *Steady-State Factor*, can be defined as:

$$S^2F = \frac{\sigma_{abs}}{\beta R_{eq}} \ . \tag{2.33}$$

With the figures of merit of interest established, it is possible to employ them in nanoparticle optimization for heat generation. This procedure is described in the next chapter.

3 NANOHEATER OPTIMIZATION FOR PHOTOTHERMAL THERAPY

In recent years, the use of metallic nanostructures for localized delivery of heat in biomedical endeavors has been the subject of numerous studies and researches (MENDES et al., 2017; HIRSCH et al., 2003; BUCHARSKAYA et al., 2016; ESTELRICH; BUSQUETS, 2018; LIU; CRAWFORD; VO-DINH, 2018; MOON et al., 2018; PHAN et al., 2018; CHEN et al., 2010). The use of nanoparticles as treatment platforms in humans raises concerns regarding accessibility from a clinical standpoint. For instance, the amount of laser energy administrable within safety levels may not be enough to efficiently induce adequate thermal variations, rendering the technique to become impractical (NIEMZ, 2007). In this chapter we appraise the optimization of nanoheaters for application in photothermal therapy.

3.1 PHOTOTHERMAL THERAPY (PTT)

Traditional cancer therapies rely heavily on drug administration (chemotherapy) and radioactive inactivation of tumorous cells. Although such therapies have been proven effective, many collateral effects arise from it (ABADEER; MURPHY, 2016). As an alternative to traditional cancer treatments, electromagnetic radiation has been explored in many different therapeutic applications that require the generation of high temperatures. For instance, microwave heating was used in thermal therapy for prostate tumors (SHERAR et al., 2001) and induced hyperthermia for breast cancer (NGUYEN; ABBOSH; CROZIER, 2017; OKE et al., 2018). PTT is a laser induced hyperthermia based thermal treatment and, thus, light-to-heat conversion plays a significant role in it. Accordingly, photosynthesizers must be administrated to obtain high efficiency photothermal conversion (LUCKY; SOO; ZHANG, 2015). PTT is based on two major components: laser light and absorbing agent. In some cases, a third element, a carrier, becomes necessary (KUMAR; SRIVASTAVA, 2017).

Biological tissues present two optical windows known as Near Infrared (NIR) transparency windows. The first window ranges from 650-950 nm, while the second spans from 1000-1350 nm (HEMMER et al., 2016). On these wavelengths, constituents such as blood, fat and proteins present a valley in their absorption spectrum. The wavelengths between 700 to 980 nm fall in the spectral range where hemoglobin and water are least absorbed by the body. This low attenuation and low scattering enable light to penetrate deeper, and thus, radiation in the NIR region must be employed for a more effective PTT. Figure 17 illustrates both NIR windows of transparency.

The absorbing agent is responsible for light-to-heat conversion. Many photosensitizers, such as organic dyes (indocyanine green and rhodamine 6B, for instance) and carbon quantum-dots have been explored to this task. Despite organic dyes exhibit good absorption of light,

Figure 17 – NIR transparency windows of biological tissues.

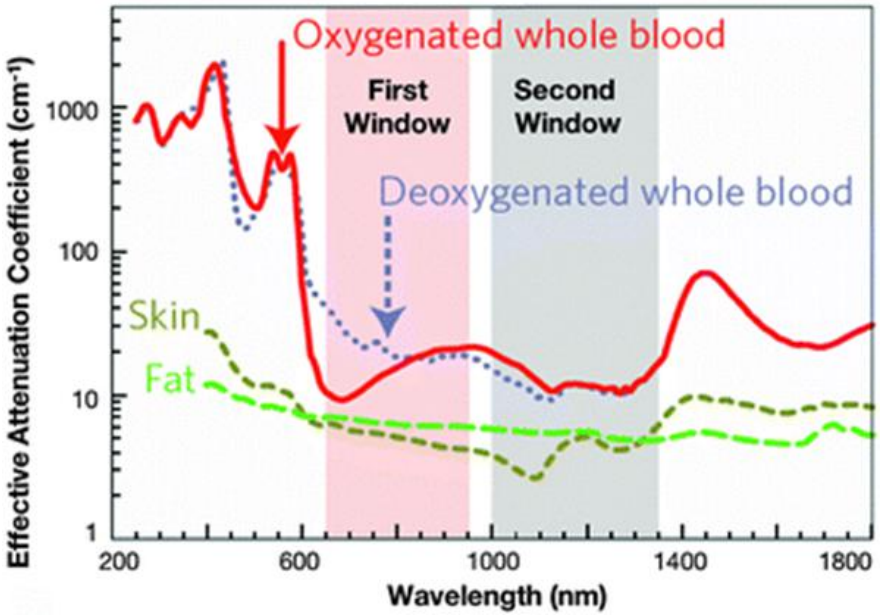

Source: (HEMMER et al., 2016).

plasmonic nanoparticles present higher absorption cross-sections, making them a more suitable PTT agent. Table 2 compares the absorption cross section of photosensitizer types. Gold nanoparticles, in special, present good plasmonic response and biocompatibility (FAN et al., 2009). The tunability of gold nanorods, capable of reaching LSPR in the NIR region and matching the transparency windows makes it a strong candidate for PTT applications (DAI, 2016).

Table 2 – Absorption cross-section of some photosensitizers.

Photosensitizer	σ_{abs} (m^2)	Ref.
Indocyanine Green	10^{-20}	(CHEN et al., 2005; BONI; MENDONÇA, 2010)
Rhodamine 6G	10^{-20}	(DJOROVIĆ et al., 2017)
Au Nanosphere	10^{-15} to 10^{-14}	(JAIN et al., 2006)
Au Nanoshell	10^{-14} to 10^{-13}	(JAIN et al., 2006)
Au Nanorod	10^{-14}	(JAIN et al., 2006)

Source: belongs to the author.

Selective killing of tumorous cells demands a system based on a carrier, usually a targeting ligand capable of attaching to a specific targeted tissue. A good carrier should be bio-compatible, biodegradable and easy to functionalize. Nanoparticle targeting to cancer cells can be either passive or active. Passive targeting may involve intratumoral administration of nanoparticles being injected directly into the particular site of the tumor or involve intravenous administration. Nanoparticles with diameters ranging from 50 and 800 nm are not capable of penetrating blood vessel walls, since the spacing between vascular endothelial cells ranges from 15 to 30 nm. However, the cellular disorganization caused by the quick and deficient generation

of new blood vessels taking place in tumorous cells triggers the formation of fenestrations with spacing up to 200 nm between vascular endothelial cells. Such fact leads to an enhancement in permeability, favoring nanoparticle uptake and accumulation within tumorous tissues near blood vessels. Therefore, passively administered drugs are more prone to accumulate in tumors rather than in healthy tissues. Nevertheless, the presence of a carrier in active targeting renders a more efficient cell uptake. In this case, small molecules such as antibodies are attached to the particles to assist its accumulation in tumors (KUMAR; SRIVASTAVA, 2017).

In some cases, such nanoparticles must be capable of penetrating the cell membrane, allowing accumulation of nanoheaters. This uptake is dependent on nanoparticle morphology and enables a more effective treatment. However, the concentration of nanoparticles administered must not be too high due to the cytotoxicity of gold nanoparticles (PAN; BARTNECK; JAHNEN-DECHENT, 2012; ZHU et al., 2014). Wang (WANG et al., 2013) et al. analyzed the effectiveness of gold nanohexapods in comparison with other nanoparticles in tumor-bearing mice. Figure 18a shows a comparison between localized heat obtained in-vivo in a tumor-bearing mice by the administration of Au nanohexapods, nanorods, nanocages and saline solution. Figure 18b shows the temperature behavior of each administered particle ensemble.

Figure 18 – Comparative study of Au nanostructures for in-vivo photothermal cancer treatment. (a) Localized heat generation. (b) Comparison in temperature evolution.

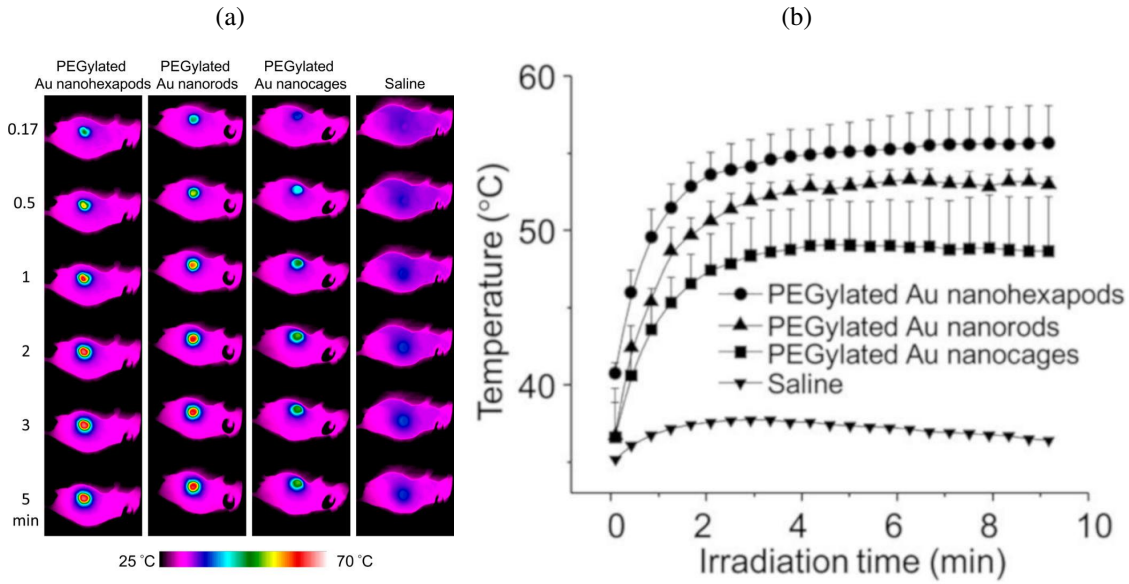

Source: adapted from (WANG et al., 2013).

The highly localized hyperthermia generated as consequence of photothermal conversion leads to membrane disruption or protein denaturation of tumorous cells, resulting in cell death. Cell death can be estimated by Arrhenius Law (NIEMZ, 2002; FENG; ODEN; RYLANDER,

2008; YAKUNIN; AVETISYAN; TUCHIN, 2015), given by

$$ln\frac{C(t)}{C_0} = -A_{rrh}\int_0^t exp\left(-\frac{\Delta E}{R_{gas}T(t')}\right)dt' \ , \tag{3.1}$$

where C_0 is the initial concentration of cells, $C(t)$ is the concentration at a time t, A_{rrh} is Arrhenius' constant and R_{gas} is the universal gas constant. The Arrhenius' constant and ΔE are specific tissue properties (NIEMZ, 2002). Equation 3.1 shows that exposition time plays an important role in cell death and that bulk relaxation time (characteristic thermalization time of the heated volume) is not enough to induce cell damage in photothermal applications (YAKUNIN; AVETISYAN; TUCHIN, 2015; MURPHY; TORSTENSSON, 2013). The time dependent temperature $T(t)$ of the heated region present in Arrhenius' equation is dependent on medium thermal diffusivity. In general, the thermal diffusivity of a tissue is approximately equal to that of water (1.3×10^{-7}m^2/s) (WALSH et al., 2010), so thermal generation measurements performed in water samples may represent a good estimation for nanoparticle based tissue heating in PTT.

3.2 NANOHEATER OPTIMIZATION

As discussed at the beginning of the chapter, the clinical application of PTT assisted by nanoparticles may be harmed by limitations imposed by safety and health standards. Therefore, nanoparticle optimization becomes highly desirable, since it can maximize light-to-heat conversion. Efforts to appraise the best Au nanorod for PTT applications were made by *Mackey et al.*, and it was concluded that a 28 × 8 nm rod is the most effective structure for plasmonic photothermal heat generation (MACKEY et al., 2014). For gold nanoshells, *Harris et al.* found 80 nm diameter (64 nm water core) to be the best heater under solar irradiation, while for irradiation by laser light, maximum efficiency is achieved for 50 nm nanoshells (45 nm water core) (HARRIS; FORD; CORTIE, 2006). These results were based on absorption efficiency analysis, i.e., the ratio of absorption cross-sections to geometrical cross-sections, and by comparison of absorption and scattering magnitudes. Due to heat generation dependency on particle morphology, optimizations based on absorption efficiency tend to restrict particles to small sizes exclusively (where scattering is negligible compared to absorption), imposing limitations on nanoparticle optimization. The methodology described in the following section investigates an approach to overcome such constraints.

3.2.1 Optimization Methodology

The very promising NIR region illustrated by figure 17 shows that low absorption occurs between 650-1350 nm. Thus, Au nanorods with LSPR in this region are preferable for PTT applications. The laser lines of 800 nm and 1064 nm are widespread. The presence of both lines

in laser equipment available in laboratories and hospitals renders its importance. Besides both lines being within NIR region, each one comprises a transparency window: 800 nm in the first, and 1064 nm in the second. The nanorod ARs with longitudinal LSPR on the chosen wavelengths are 4.0 and 6.4 to $\sim$ 800 nm and $\sim$ 1064 nm respectively, as can be noticed in figure 13. By changing nanorod dimensions while maintaining a fixed AR to each case, the peak position of resonance barely moves (within certain size conditions). It becomes convenient, thus, to evaluate the previously discussed figures of merit to each AR. It is important to point out that the current analysis assumes Au nanorods embedded in aqueous medium.

Figure 19 is a colormap that depicts the LSPR as function of nanorod length and diameter. The blue line represents nanorod dimensions with LSPR in 800 nm, while the red line represents nanorod dimensions with LSPR in 1064 nm. The dephasing effect that arises from increasing nanorod length shifts the LSPR peak position. The red-shift becomes more noticeable to voluminous nanorods. The inset of 19 illustrates the process of increasing nanorod size while maintaining a fixed AR.

Figure 19 – LSPR peak position for gold nanorods of different lengths and diameters. The inset figure shows the sweep procedure for a fixed AR.

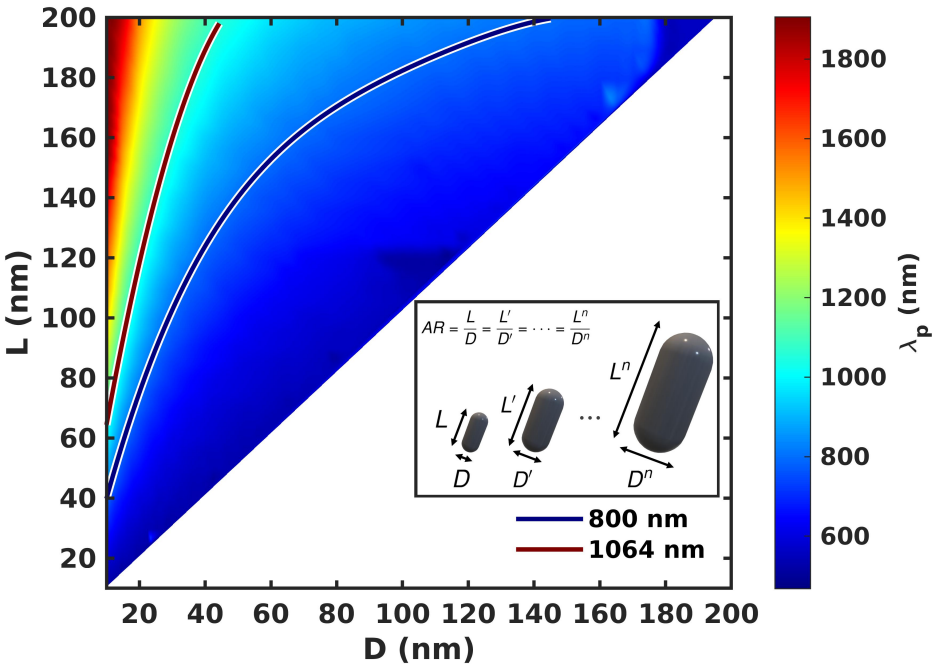

Source: belongs to the author.

Plasmonic properties of a single rod were appraised by means of FEM simulations in COMSOL Multiphysics. The *Electromagnetic Waves, Frequency Domain* module was used to perform the simulations. The simulation models a single gold nanorod of length L and diameter D embedded in water. The nanoparticle permittivity is size-corrected accordingly to the Drude formulation described in chapter 2, while the aqueous medium is assumed to be wavelength

independent. The nanoparticle-water set is surrounded by a spherical *perfectly matched layer* (PML) shell responsible for mimicking an open boundary, and assumes the propagation of a linearly polarized monochromatic plane wave with polarization parallel to the longitudinal axis of the nanorod. A *normal* mesh was used in the PML and nanorod surroundings, while a *finer* mesh was implemented in the nanorod domain. To both aspect ratios, the nanorod length L was swept from 15 nm up to 200 nm. Figure 20 illustrates the cross-section of the meshed simulation setup.

Figure 20 – Meshed simulation setup used for nanorod optimization.

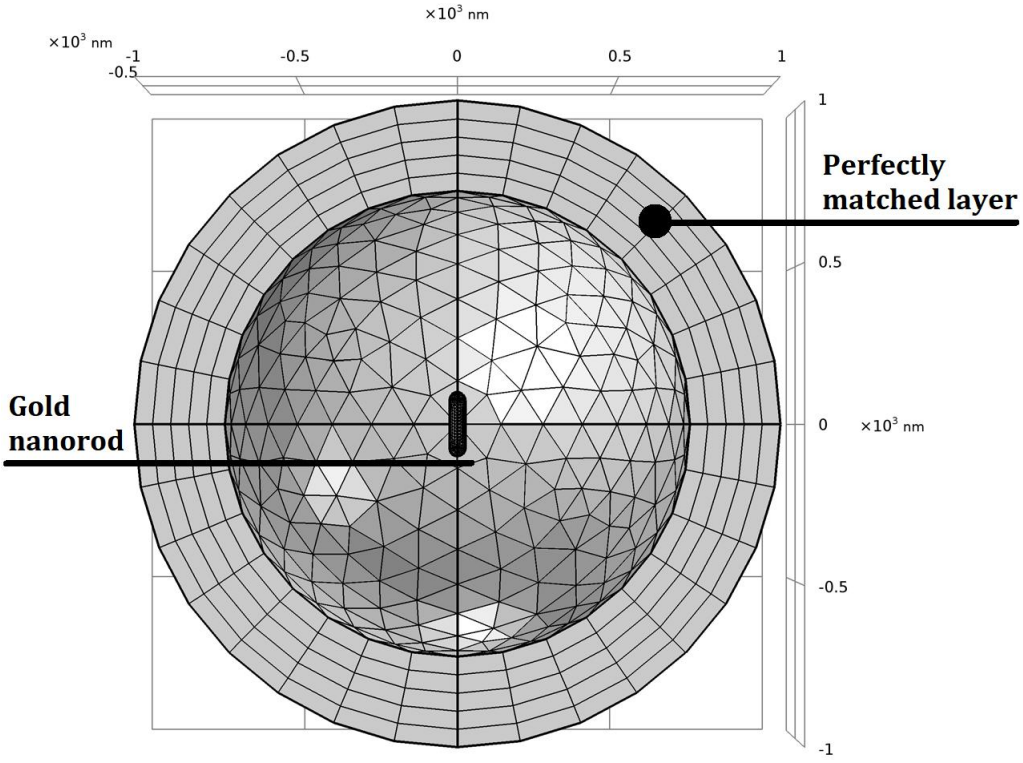

Source: belongs to the author.

3.2.2 Photothermal Conversion Efficiency

The first figure of merit to be evaluated is the Photothermal Conversion Efficiency (η). figure 21a is a colormap that shows how this parameter changes with nanorod dimensions, while figure 21b illustrates the decreasing behavior observed in η, expected for increasing nanoparticle sizes as scattering overcomes absorption. To this analysis alone, it is clear that the extinction of a small nanoparticle results in almost all energy being absorbed and converted into heat. At first, it may be compelling to think that a smaller size is preferable for heat generation. However, since the relation between nanoparticle surface area to nanoparticle volume is a significant element on how energy is transferred to its surroundings, particle morphology turns into a critical parameter, and η becomes an insufficient criterion to evaluate heat generation by plasmonic nanoparticles.

Figure 21 – Photothermal Conversion Efficiency for gold nanorods with LPSR in 800 nm (blue) and 1064 nm (red). (a) Colormap for various gold nanorod lengths and diameters. (b) Photothermal Conversion Efficiency as a function of nanorod length.

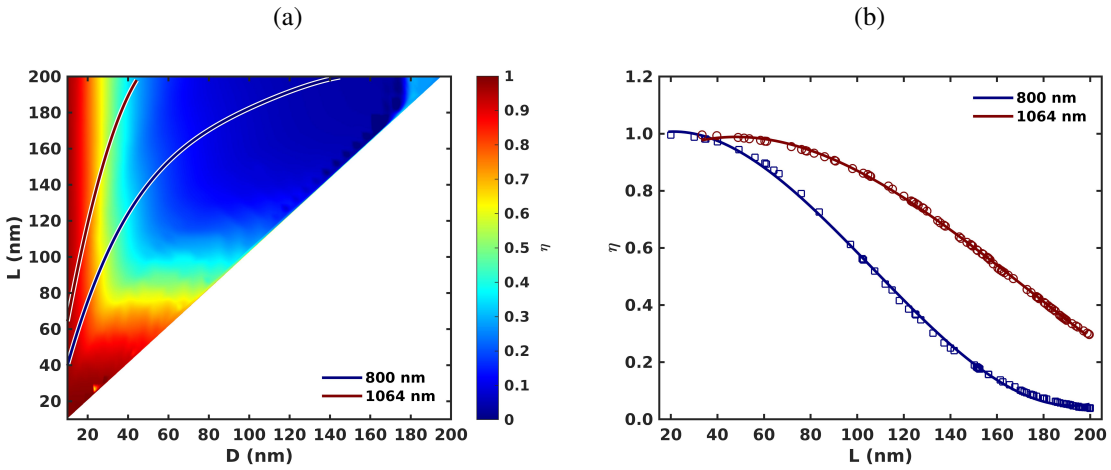

Source: belongs to the author.

3.2.3 Joule Number - Optimization for Nanosecond Pulse Excitation

To nanosecond pulses, the adequate figure of merit for optimization is the Joule Number (equation 2.27). The Joule Number colormap of figure 22a show the J_0 of gold nanorods at the LSPR for various lengths and diameters. The blue and red lines highlight, respectively, the J_0 for LSPR at 800 nm and 1064 nm. Figure 22b transcribes the behavior of J_0 along the blue and red lines as a function of nanorod length. From such figures, it becomes noticeable that, for a fixed LSPR wavelength, there exists an optimal length at which J_0 magnitude is maximized. As nanoparticle size increases, J_0 magnitude grows, until it reaches a maximum value and starts to decrease. This result contradicts the expectations caused by η analysis alone. A quick inspection of equation 2.27 shows that the heat generation capacity of a nanoparticle is proportional to its absorption cross-section and is inversely related to its volume (σ_{abs}/V). As the particle grows bigger, so do both contributions. However, absorption and volume grows at different rates, depending mainly on particle morphology. This fosters the existence of a threshold dimension at which the volume contribution overcomes absorption.

To nanorods with AR 4.0, presenting LSPR peak at around 800 nm, the higher J_0 value occurs for a length of 45 nm ($\sim$ 11 nm diameter). This indicates that nanorods with dimensions L = 45 nm and D = 11 nm are the most suitable gold rod-like particles for photothermal heat generation at 800 nm concerning nanosecond excitation. Similarly, for nanorods with LSPR around 1064 nm, the ideal dimensions to maximize J_0 magnitude are a length of 60 nm and $\sim$ 9 nm diameter. The localized heat generated internally by such nanorods under single nanosecond pulse excitation yields an optimal value of maximum temperature variation that may be explored in PTT.

Figure 22 – Joule Number for gold nanorods with LPSR in 800 nm (blue) and 1064 nm (red). (a) Joule number colormap for various gold nanorod lengths and diameters. (b) J_0 as function of nanorod length for LSPR at 800 nm and 1064 nm.

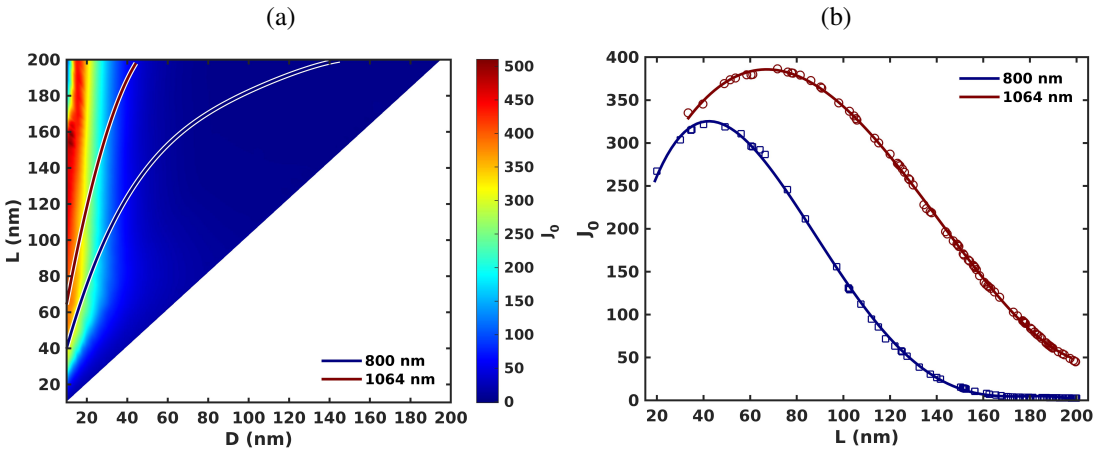

Source: belongs to the author.

3.2.4 Steady-State Factor - Optimization for Continuous Excitation

In this case, the *de-facto* heat generation optimization is exerted by the Steady-State Factor (equation 2.33). Figure 23a depicts the S^2F of gold nanorods at the LSPR for various lengths and diameters. The blue and red lines highlight, respectively, the S^2F for LSPR at 800 nm and 1064 nm. Figure 23b transcribes the behavior of S^2F along the blue and red lines as a function of nanorod length. In figure 23b, one can notice a substantial increase in S^2F as the nanorod grows larger. Similarly to what happens in the case of J_0, the existence of a maximum value at which S^2F magnitude peaks is also apparent. Differently from J_0, where the morphology dependency isn't explicit in its equation, equation 2.33 highlights shape dependency by introducing the shape factor β. Nanoparticle volume dependency is indirectly represented by an equivalent radius, rendering the figure of merit S^2F a unit of length. The maximum S^2F value happens at longer nanorod lengths when compared to the single nanosecond pulse case.

The behavior of steady-state factor values as function of the nanorod length is shown in figure 23b. The blue line show that the best gold nanorod with LSPR in 800 nm to undergo continuous excitation photothermal conversion has length L = 105 nm and diameter D = 26 nm, while continuous excitation heat generation at 1064 nm is optimized at dimensions L = 180 nm and D = 28 nm. The red-shift caused by dephasing of conduction electrons in bigger structures is more significant here due to the exploration of longer nanorod sizes necessary to achieve maximum S^2F. At such sizes scattering plays an important role in light extinction and may reduce the penetration depth of light in PTT assays comprising of bigger nanoparticles.

Figure 23 – Steady-State Factor for gold nanorods with LPSR in 800 nm (blue) and 1064 nm (red). (a) S^2F colormap for various gold nanorod lengths and diameters. (b) S^2F as function of nanorod length for LSPR at 800 nm and 1064 nm.

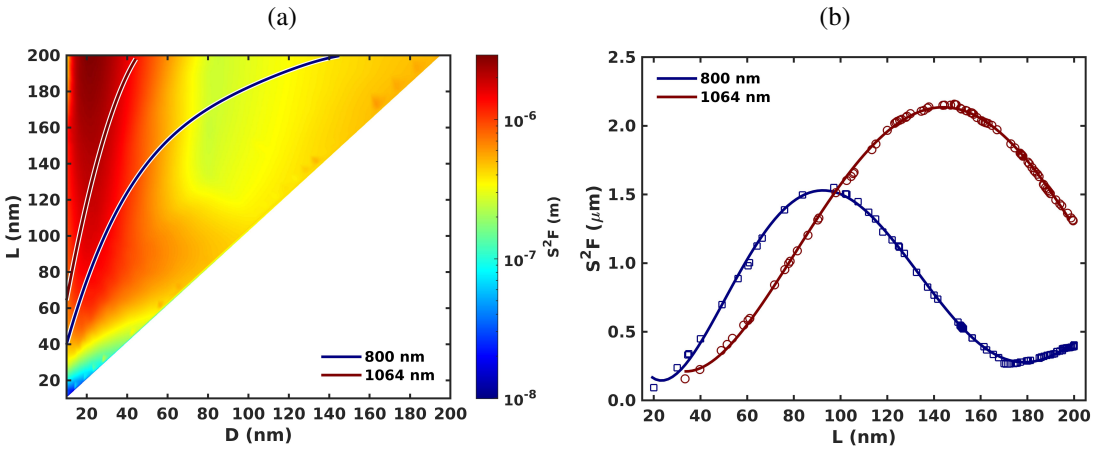

Source: belongs to the author.

3.2.5 Practical Concerns

Each particle morphology will provide a different behavior to Joule number and steady-state factor, shifting the optimal points to longer or shorter nanoparticle sizes. Morphology is an important aspect on the field of thermoplasmonics. As discussed before, blood vessel fenestrations impose an upper limit on nanoparticle size, and large nanoparticles may not be absorbed by tumorous tissues. Moreover, for PTT applications, attention must be given to post treatment excretion of nanoparticles, since its accumulation in the kidney may lead to complications. The nanoparticle shape, surface chemistry, and charge may lead to distinct renal handling of such structures. In general, nanoparticles with diameters smaller than 5 nm can undergo renal clearance (CHOI et al., 2007; LONGMIRE; CHOYKE; KOBAYASHI, 2008). For larger nanoparticles, surface charge and chemistry can optimize this excretion pathway (CHOI et al., 2007; LONGMIRE; CHOYKE; KOBAYASHI, 2008). Renal excretion represents a desirable pathway for nanoparticle removal with minimal catabolism, avoiding the possible side effects (CHOI et al., 2007; LONGMIRE; CHOYKE; KOBAYASHI, 2008). To overcome such problem, the use of charge-coupled (CCP) and charge-transfer structures (CTP) may be considered. CCP and CTP structures are dimers comprised of two nanoparticles closely connected by a bridging material. The bridging material keeps both nanoparticles close within nanometric distance, and is made of a dielectric material (CCP dimer) or a metal (CTP dimer). Under light irradiation, the near field of both nanoparticles superimpose, generating a high intensity electric field in the bridge. Due to this interaction, the field enhancement seen in the LSPR condition is more pronounced in dimers when compared to single nanoparticles. Also, due to tunneling effects between nanoparticles, the electrons see a longer nanostructure, red-shifting the LSPR to infrared wavelengths (FONTANA et al., 2016; FONTANA et al., 2017).

4 CHARACTERIZATION OF METALLIC NANOPARTICLE COLLOIDS BY THERMAL LENS MEASUREMENT

Evaluate the performance of nanoparticles as nanoheaters is a fundamental step to the development of efficient platforms and techniques that rely on either distributed or localized heat generation. The assessment of temperature response enables the development and use of high performance nanoparticles to an effective heat generation.

A possible method to analyze temperature variation around a nanostructure is by means of nanothermometry, where a fluorescent nanocrystal is used to measure temperature by assessing changes in fluorescent emission. There are two ways of conducting nanothermometrical measurements: by looking at peak shifts on fluorescent emission (SCHRUM et al., 1994; ROSAL et al., 2016) or by fluctuations in fluorescence intensity (JAQUE; VETRONE, 2012). To conduct a nanothermometrical essay on a plasmonic nanoparticle, it is necessary to bind a fluorescent nanocrystal to the metallic nanoparticle. For instance, Quintanilla et al. described a way to appraise the heating of single gold nanostars by combining it with $CaF_2 : Y^{3+}$ and $CaF_2 : Nd^{3+}$ nanoparticles, two common near-infrared fluorescent nanothermometers (QUINTANILLA et al., 2019). Despite allowing measurements where conventional methods are ineffective, nanothermometry imposes experimental difficulties in sample preparation. Similarly complex sensors were developed to estimate temperature variation in metallic nanoparticles (CARLSON; KHAN; RICHARDSON, 2011), where gold nanoparticles were placed on an fluorescent substrate. Microscopic thermal imaging have also been explored (BAFFOU et al., 2012; BAFFOU; GIRARD; QUIDANT, 2010) to map heat generation, but such techniques are as complex as the aforementioned.

Simpler and more widespread methods in temperature evaluation, such as thermocouples (RICHARDSON et al., 2006; RICHARDSON et al., 2009) and thermal cameras (WONG et al., 2013; LÓPEZ-VARELA et al., 2018) are somewhat limited. Thermocouples present bad accuracy (0.5-5.0 ^{o}C) and slow response (0.1-10 s), while thermal cameras have small dynamic range, fixed focus, time response in the order of the second and low spatial resolution, relying upon a CCD/CMOS sensor and signal processing to create an image in addition to the much smaller array of thermal sensors. For instance, Richardson et al. explored thermocouples to measure the laser heating (280 mW @ 532 nm) of a droplet containing a colloidal solution of 20 nm gold nanospheres. The droplet is formed at the tip of a thermocouple, and temperature variations induced in the sample are measured by it. Figure 24a illustrates the thermocouple assessment. Varela et al. shows the use of thermal camera to sense temperature variation in a skin-equivalent sample, caused by multibranched gold nanoparticles present in the material, as can be seen in figure 24b. The irradiation of 150 mW @ 785 nm laser light induced a thermal variation of 4.5 ^{o}C, for sample concentration of 5.2×10^8 mL^{-1}.

Figure 24 – Methods of measuring temperature evaluation of colloids. (a) Thermocouple measuring photothermal effects in a drop. (b) Thermal camera assessment of heat generation.

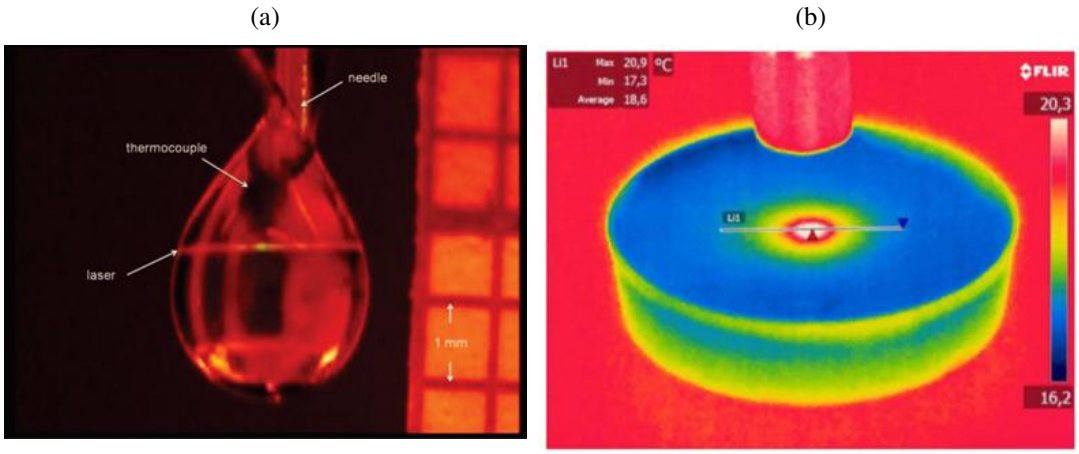

Source: adapted from (RICHARDSON et al., 2009) and (LÓPEZ-VARELA et al., 2018).

A new strategy to assess thermal-optical properties of metallic nanoparticle colloids is required. This chapter introduces the use of Thermal Lens measurement to establish a middle ground betwixt macro (global) and nano assessment of temperature on nanoheater characterization.

4.1 HEATING OF A NANOPARTICLE ENSEMBLE

Here, it will be analyzed the heating phenomenon of a macroscopic ensemble of particles embedded in a solvent, and its relation to each individual nanoscopic heat source. Differently from what happens in steady-state heating of a single particle, as illustrated in figure 16, sustained heating of a large number of dispersed nanostructures can produce a significant global temperature rise, even if the local temperature rise at each particle is negligible (KEBLINSKI et al., 2006).

To global temperature analysis, both the time scale needed for thermal fields from neighboring particles to overlap and the time scale for thermalization across the entire volume of the colloid must be considered. The global thermalization time can be obtained by the use of equation 2.22. Keblinski et al. (KEBLINSKI et al., 2006) systematized a simulation to obtain the global temperature as the superposition of the temperature fields given by the exact solution Laplace equation (2.28) originated from the contribution of all nanoheaters. To do so, he considered the heating of a spherical medium with 1 mm of radius and limited the problem to an ensemble of 5000 randomly dispersed nanoheaters. The nanoparticle radius was 65 nm and each particle acted as a power source of 1.4×10^{-14} W (KEBLINSKI et al., 2006). The assumed volumetric concentration of particles was 10^{15} m^{-3}. Figure 25 shows the obtained result of reference (KEBLINSKI et al., 2006).

Figure 25 – Temperature rise near the surface of a nanoparticle as a function of heating time to an ensemble of nanoheaters.

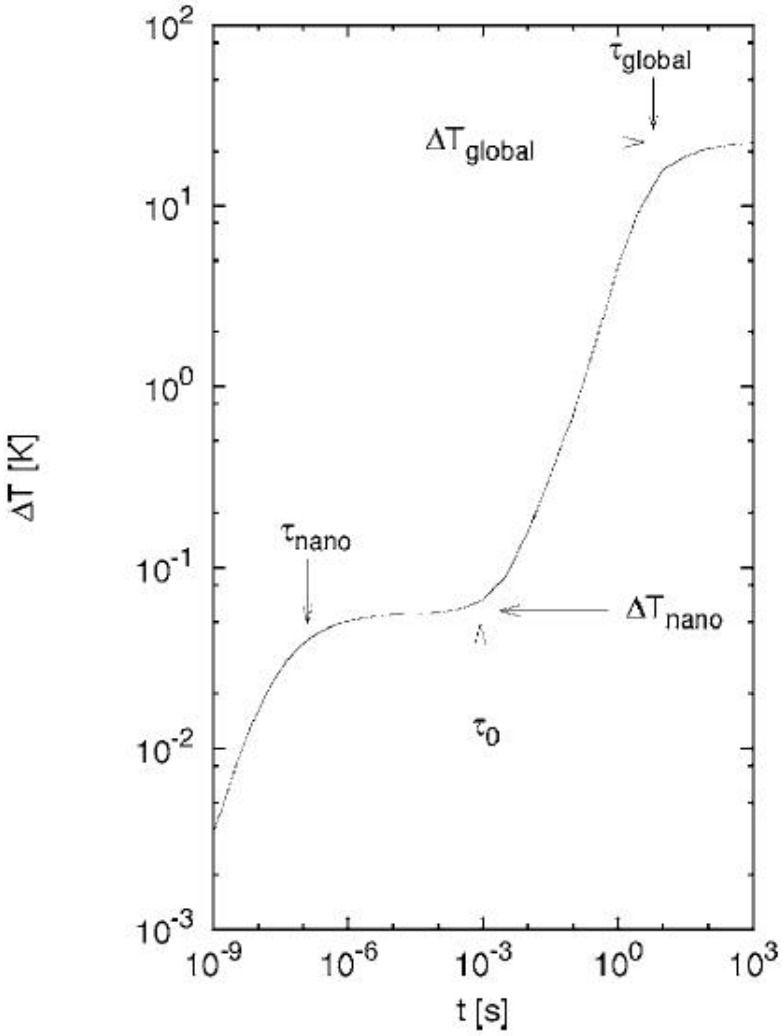

Source: adapted from (KEBLINSKI et al., 2006).

The temperature rise is limited to the nanoparticle itself, until it reaches the nanoparticle steady-state at τ_{nano}. Thereafter, as the temperature fields of the surrounding particles reaches the particle in analysis (τ_0), this intermediate steady-state is surpassed and the global temperature rise dominates the total temperature change. The global steady-state is reached at τ_{global}. The ratio between the final global temperature and the initial localized steady-state ($\Delta T_{global}/\Delta T_{nano}$) can be several orders of magnitude higher (KEBLINSKI et al., 2006), depending on nanoparticle concentration.

The superposition effect can be described by the equation 4.1:

$$\Delta T_{global} = \sum_{i=1}^{N_p} \frac{\sigma_{abs} I}{4\pi\kappa_m \beta |\vec{r} - \vec{r}_i|} \ , \tag{4.1}$$

Here, ΔT_{global} represents the global temperature variation and N_p the number of nanoparticles.

For excitation times longer than τ_{global}, an analogy with electrostatics can be drawn, and one can replace the nanoparticles by a homogeneous heat source distributed throughout the entire heated region (KEBLINSKI et al., 2006). Assuming that the global volume is thermalyzed, it is possible to rewrite equation 4.1 as a volume integral. Therefore, a temperature analysis at the center of the system can be done without loss of generality. Solving the "*thermal potential*" integral for a cylindrical region of length ℓ, radius w_0 and nanoparticle concentration C_{np}, one gets

$$\Delta T_{global} = \pi w_0^2 \, C_{np} R_{eq} \ln\left(\frac{2\ell}{w_0}\right) \Delta T_{np} \, . \tag{4.2}$$

One can notice that the global to nanoparticle temperature ratio is independent from administered power. A depiction of global heating induced by plasmonic nanoparticles can be seen in figure 26. Here, the incident radiation (reddish arrow) excites a sample. The black dashed circle symbolizes the limits of the region of radius w_0 containing the nanoparticle ensemble to undergo photothermal generation. The small yellow dots represents the randomly dispersed nanoheaters, and the circles that surrounds it are regarded as the time dependent range of the "heat front" generated by each nanoparticle. When all individual heat fronts overlap, the region bounded by black dashes can be considered to be completely thermalyzed.

Figure 26 – Global heating induced by plasmonic nanoparticles.

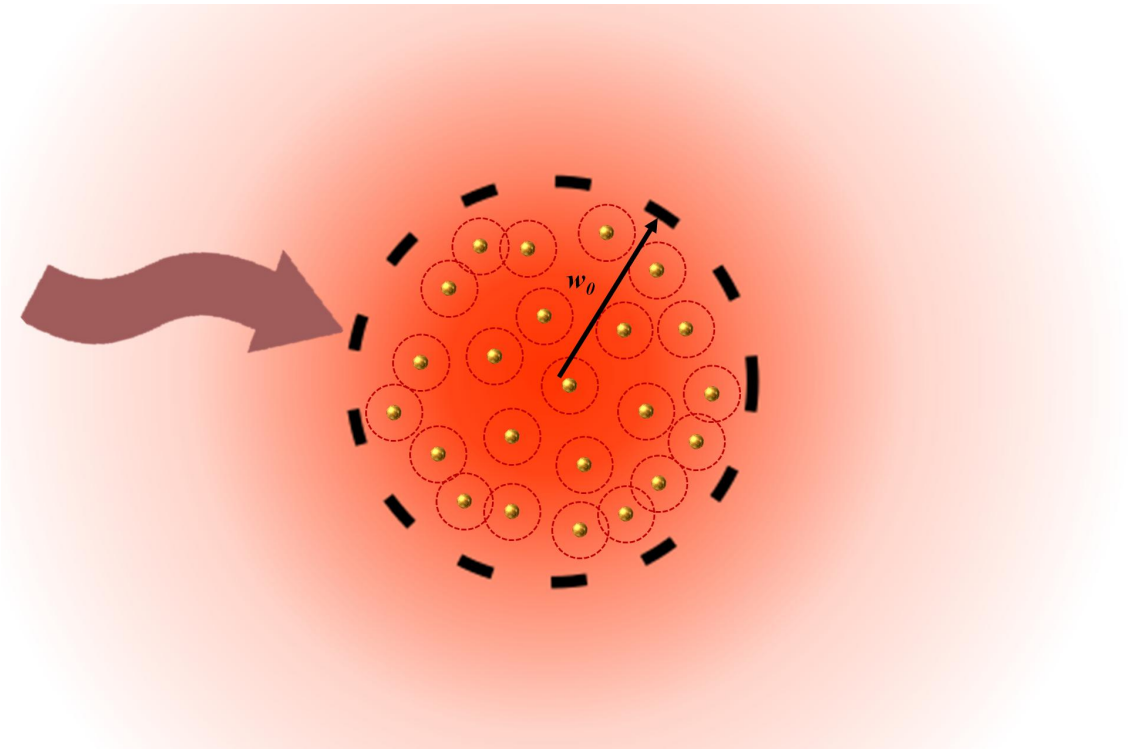

Source: belongs to the author.

4.2 TEMPERATURE ASSESSMENT BY THERMAL LENS TECHNIQUE

On roads, during some of the hottest days of the year, it may look as if some sort of liquid has been spilled over the pavement, mirroring in a wobbling fashion the objects that pass through it. In such hot conditions, the asphalt exposed to the sun easily reaches temperatures higher then the air above it, and convective effects help the formation of a gradient in air density, consequently changing the refractive index of air. This phenomenon is called *inferior mirage*, and leads to a smooth refraction of light, continuously bending it. Figure 27 illustrates the inferior mirage effect. As the refractive index of the air near the pavement is smaller (due to a smaller air density), part of the light coming from the sky that would not reach observer eyes in normal conditions suffers refraction, reaching the observer from below. As sky light is reaching the observer from the bottom up simultaneously with the direct light from other objects that are not affected by the refractive index gradient (sky, truck and road), the sky seen from below is interpreted as a mirror or puddle.

Figure 27 – Mirage formation due to refractive index gradient.

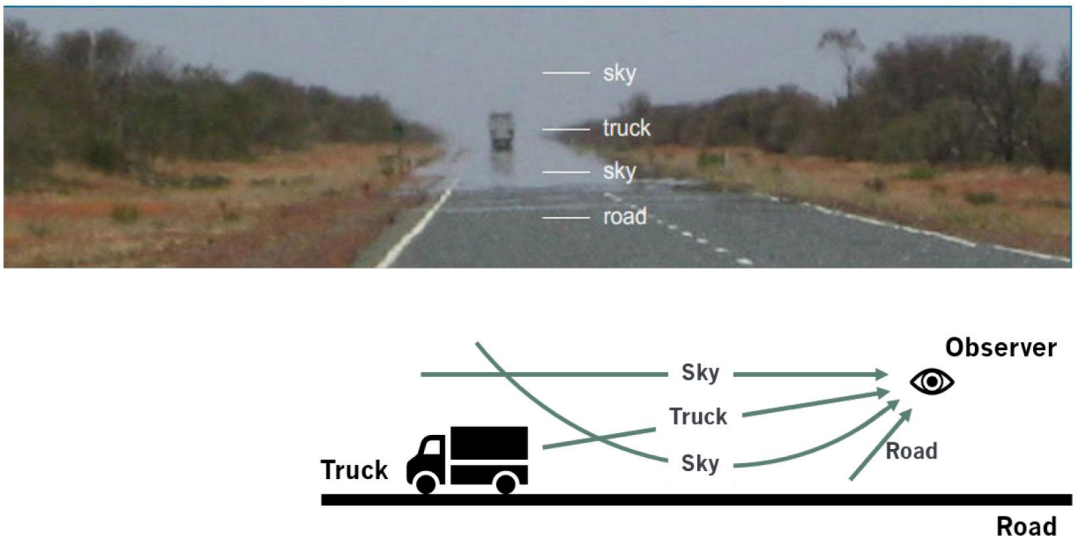

Source: adapted from (SYDNEY AUSTRALIA, 2009).

A gradient in refractive index effect may arise during the propagation of a light beam in a transparent medium. Laser energy may be absorbed by the sample, and the temperature gradient that appears in the material due to non-radiative relaxation causes a refractive index gradient, as a divergent lens, that can be exploited to measure optical and thermal properties of liquids and solids. This phenomenon is known as *thermal lensing*. The thermal lens effect (TL) was accidentally discovered by the insertion of liquid samples inside a *He-Ne* laser resonator (GORDON et al., 1965), and was readily noticed that the insertion caused long-transient effects in laser build-up. This effect has since been used to measure low absorption liquid samples (GORDON et al., 1965; LEITE; MOORE; WHINNERY, 1964; WHINNERY, 1974; DOVICHI; HARRIS, 1979; LEACH; HARRIS, 1981).

Among TL applications, it is worth mentioning its use to measure thermal diffusivity of liquids and glasses (BAESSO; SHEN; SNOOK, 1992; BERNAL-ALVARADO et al., 2003; COMEAU; HACHÉ; MELIKECHI, 2003), its use in chromatographic analysis (BUFFETT; MORRIS, 1982), and application in fluorescence/quantum-yield measurements (CRUZ; PILLA; CATUNDA, 2010; ESTUPIÑÁN-LÓPEZ; DOMINGUEZ; ARAUJO, 2013). TL theory has also seen applicability in thermally controlled reconfigurable focal length lenses (D. et al., 2016) and the thermal management of high-repetition rate measurements of non-linear optical parameters by Z-Scan (FALCONIERI, 1999; GOMES et al., 2007; GNOLI; RAZZARI; RIGHINI, 2005). A TL spectrophotometer was also developed using a xenon lamp to determine the absorption spectra of scattering samples (MARCANO et al., 2014). More recent efforts to improve the sensibility of TL measurements were performed by Marcano (MARCANO; LOPER; MELIKECHI, 2002), and ultra sensitive TL measurements of water were conducted (CRUZ et al., 2009).

The TL measurement is an example of time-resolved spectroscopy (FARR et al., 2018), and is based on the analysis of the temporal evolution of light intensity transmitted through a sample. This intensity profile presents the peculiar feature of using laser light to either pump and probe TL effects. In single-beam TL, pumping and probing are performed by a single laser exciting and sensing thermally induced effects. On a dual beam TL measurements, pumping is achieved by an interacting wavelength laser beam and probing is accomplished by a second laser of non-resonant wavelength. In both cases, the thermally induced phase delay on laser wavefront is measured by a photodetector. The phase-shift nature of such measurements renders the accuracy of TL assessments comparable to interferometric methods (MARCANO; LOPER; MELIKECHI, 2002), being able to perform measurements of refractive-index variations as low 10^{-8}, which is associated to temperature variations of 10^{-5} ^{o}C (HU; WHINNERY, 1973). Besides that, the essay requires a minimum amount of material when compared to sample volumes demanded by the thermal camera method, and shows a faster response when compared to thermocouple measurements.

4.2.1 Single Beam TL Technique (STL)

The STL experiment comprises a relatively simple experimental setup. A chopped and collimated laser beam with Gaussian profile, wavelength λ and power P_{exc} passes through a focusing lens *f*, acquiring a beam waist w_0 at the focus of Rayleigh lenght z_R. A thin absorptive sample of size $\ell < z_R$ and absorption coefficient α is then placed within the confocal parameter *b* (focus depth) of the focused beam at a certain position *z*. After interacting with the sample, the beam travels a long distance before reaching a small aperture in the far-field. The aperture size $\Sigma = 1 - e^{-2(r/w_0)^2}$, the aperture linear transmittance in the absence of a sample (where *r* is the aperture radius), is important, and must be treated in accordance to Sheik-Bahae (SHEIK-BAHAE et al., 1990). The use of $\Sigma \approx 0.7$ is a good compromise between having a large signal which averages possible beam nonuniformities (ARAÚJO; GOMES; BOUDEBS, 2016). The light intensity transmitted by the aperture is then measured by a photodetector (SHELDON;

KNIGHT; THORNE, 1982). Figure 28 illustrates the concept.

Figure 28 – Basic setup of a STL experiment.

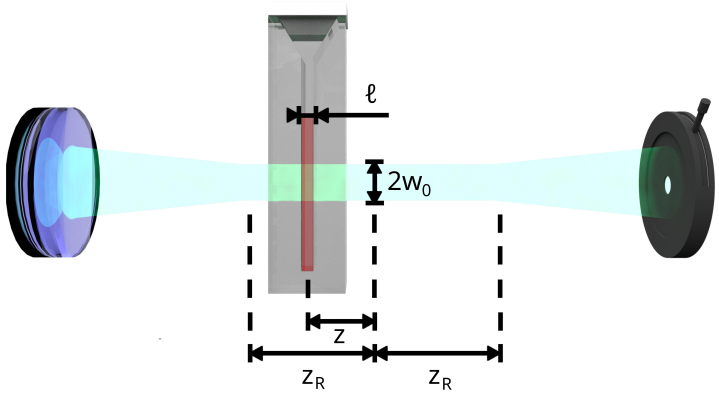

Source: belongs to the author.

The small spot area within z_R ensures a high laser intensity at the sample. The energy of the beam is partially absorbed by the sample and converted into heat. The heat generation in the illuminated region will follow the beam intensity profile, and thus the temperature variation will also be Gaussian. The radial characteristic of temperature will induce a volumetric expansion in the heated region, generating a refractive index gradient. If ℓ is smaller or has the same order of z_R, heat generation can be considered bi-dimensional. The induced phase shift caused by the sample can be written as (SHELDON; KNIGHT; THORNE, 1982):

$$\Delta\Phi = \frac{2\pi\ell}{\lambda}\Delta n \ . \tag{4.3}$$

In equation 4.3, $\Delta n = n(T) - n_0$ is the thermally induced refractive index difference and n_0 is the refractive index of a relaxed sample. To better represent the temperature dependent variation of refractive index, it can be expanded in Taylor Series as:

$$n(T) = n_0 + \left(\frac{dn}{dT}\right)\Delta T + \frac{1}{2}\left(\frac{d^2n}{dT^2}\right)(\Delta T)^2 + \dots \ , \tag{4.4}$$

where ΔT is the induced temperature variation, dn/dT is the *thermo-optic coefficient* and d^2n/dT^2 is the *second-order thermo-optic coefficient*. To most liquids, the first order approximation is sufficient to represent thermally induced changes in refractive index. It is possible, thus, to rewrite equation 4.3 as:

$$\Delta\Phi = -\frac{2\pi\ell}{\lambda}\left(\frac{dn}{dT}\right)\Delta T \ . \tag{4.5}$$

To most regular solvents, dn/dT is negative, which means that refractive index decreases as the temperature rises. Figure 29 qualitatively illustrates this behavior.

Figure 29 – Temperature and refractive index gradient profiles.

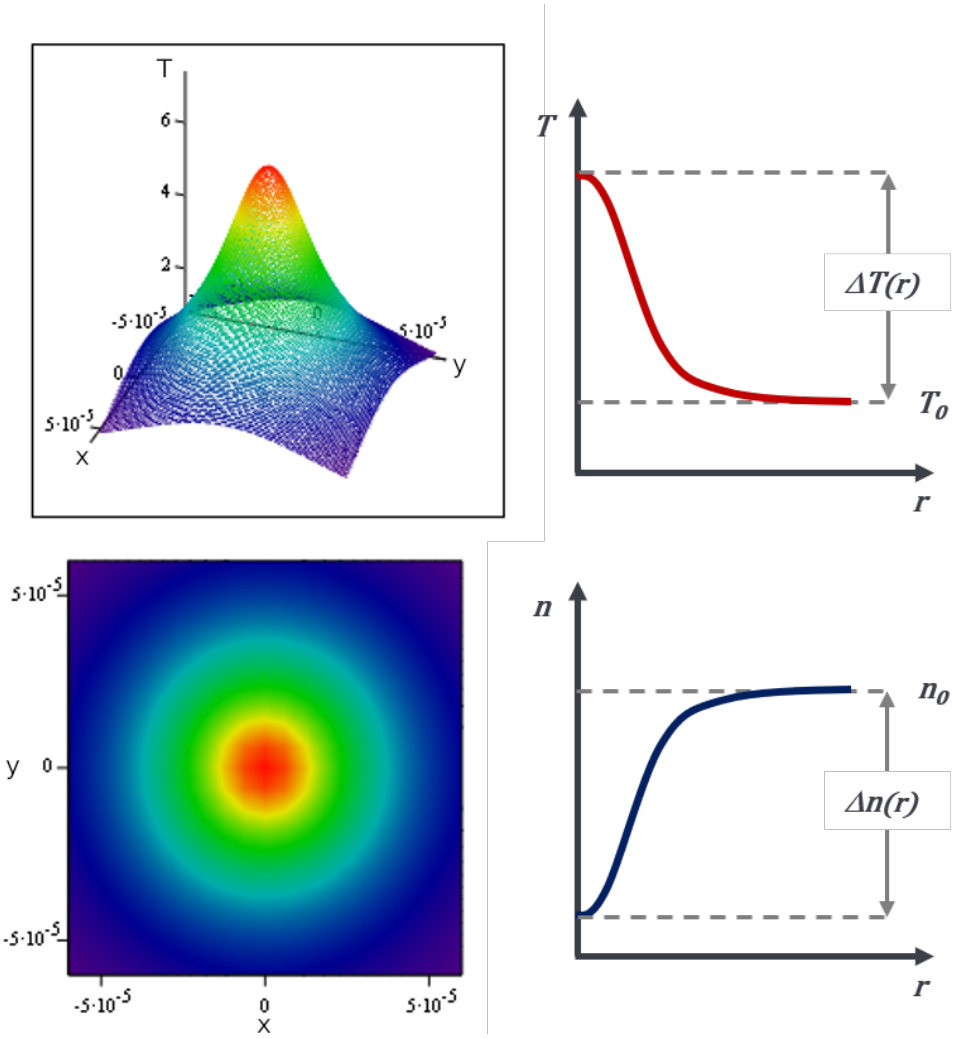

Source: belongs to the author.

The top-left figure shows the Gaussian temperature variation induced in the sample by the laser, while the top-right graph illustrates the temperature profile as a function of the radial distance from laser beam center. The bottom-left image depicts the thermally induced refractive index variation at the sample, while the bottom-right graph indicates how refractive index changes with radial distance from laser beam axis. Such figures illustrate the optical and thermal behavior of a sample with negative thermo-optic coefficient. For instance, if the thermo-optic coefficient of the sample is positive, the refractive index would increase with the temperature, generating a decreasing refractive index profile with radial distance from laser beam axis. Such refractive index behavior supports the formation of a converging thermal lens. The change of this parameter depends mainly on the change in density caused by the coefficient of thermal expansion.

By solving the Laplace equation, obtaining ΔT and solving the diffraction problem, the evolution of TL signal measured by the photodetector over time, $I(V,t)$, can be expressed as (SHEN; LOWE; SNOOK, 1992):

$$\frac{I(V,t)}{I(V,0)} = \left\{1 - \frac{\theta}{2} tan^{-1}\left[\frac{2V}{(9+V^2)\frac{t_c}{2t} + 3 + V^2}\right]\right\}^2 . \tag{4.6}$$

Here, $I(V,0)$ is the measured signal before heating, and $t_c = w_0^2/4D_{th}$ is the lens formation characteristic time, with D_{th} being the thermal diffusivity of the medium. The thermal lens strength and normalized sample position are respectively $\theta = -\frac{P_{exc}\alpha\ell}{\kappa_m\lambda}\frac{dn}{dT}$ and $V = z/z_R$. The $\ln$ term present in equation 4.6 was dropped for interpolation reasons accordingly to Shen et al. (SHEN; LOWE; SNOOK, 1992).

4.2.2 Dual Beam Mode-Mismatched TL Technique (DTL)

The dual beam TL experiment presents many similarities to the STL approach. The only substantial difference when compared to the technique previously presented is the requirement of a second laser (probe beam) with wavelength λ_p. The method allows the measurement of thermal effects induced by a pump beam, by means of a probing beam. The probing beam Rayleigh length z_{op} must be longer than the pump Rayleigh length to allow off-axis optical probing. The probe waist w_p must also be bigger than the pump waist w_{ex}. Such fact means that for a fixed pump waist, the characteristic time $t_c = w_p^2/4D_{th}$ associated to the DTL experiment must be longer than the characteristic times seen in the STL experiment.

The difference between pump and probe beam waists requires a reformulation of equation 4.6, introducing the mode-matching factor *m*. The mode-matching factor accounts for the spatial matching of the electric field distributions of both pump and probe laser beams, and is given by $m = (w_p/w_{ex})^2$. The two beams are said to be mode-matched if m = 1, and are said to be mode-mismatched if m $>$ 1. Therefore, the DTL signal is described by (SHEN; LOWE; SNOOK, 1992):

$$\frac{I(V,t)}{I(V,0)} = \left\{1 - \frac{\theta}{2} tan^{-1}\left[\frac{2mV}{((1+2m)^2+V^2)\frac{t_c}{2t} + 1 + 2m + V^2}\right]\right\}^2 , \tag{4.7}$$

with

$$\theta = -\frac{P_{exc}\alpha L}{\kappa_m\lambda_p}\frac{dn}{dT} , \tag{4.8}$$

and

$$V = \frac{z}{z_{op}} + \frac{z_{op}}{z_2}\left[1 + \left(\frac{z}{z_{op}}\right)^2\right] . \tag{4.9}$$

Here, z_2 is the distance between sample and photodetector. If m = 1, equation 4.7 restores equation 4.6, as expected. Again, the $\ln$ term present in equation 4.7 was dropped for interpolation reasons as reported by Shen et al. (SHEN; LOWE; SNOOK, 1992). Here, z_2 is the distance between sample and photodetector. If m = 1, equation 4.7 restores equation 4.6, as expected. Again, the $\ln$ term present in equation 4.7 was dropped for interpolation reasons as reported by Shen et al. (SHEN; LOWE; SNOOK, 1992). The implementation of the DTL experiment introduce many advantages in comparison to the STL method. Due to a probe beam waist wider than the pump beam waist, the DTL experiment take advantage of the overall thermal contribution induced by the pump beam, testing a larger volume when compared to STL measurements (MARCANO; LOPER; MELIKECHI, 2002). Thus, the mode matching factor magnifies the thermally induced phase-shift by a factor of *m* (SHEN; LOWE; SNOOK, 1992):

$$\Delta\Phi = m\ (2\pi\ell/\lambda_p)\Delta n\ . \tag{4.10}$$

Since equation 4.10 is related to system sensibility, the use of the DTL experiment allows the measurement of temperature variations that are imperceptible to the STL setup. Another advantage of the DTL technique, is the prospect of measuring the thermal relaxation response in time, as the probe beam is not required to be chopped. The method also enables spectroscopic measurements by changing pumping beam wavelength. As long as the sample remains transparent to the probe beam, the same probe-photodetector arrangement can be used in spectroscopic analysis, removing the need for broadband photodetectors. The figure 30 illustrates DTL technique details.

Figure 30 – Ilustration of DTL setup at the focal region. The position z of a sample of thickness ℓ and the photodetector distance z_2 are described, as well as pump and probe waists (w_{ex} and w_p).

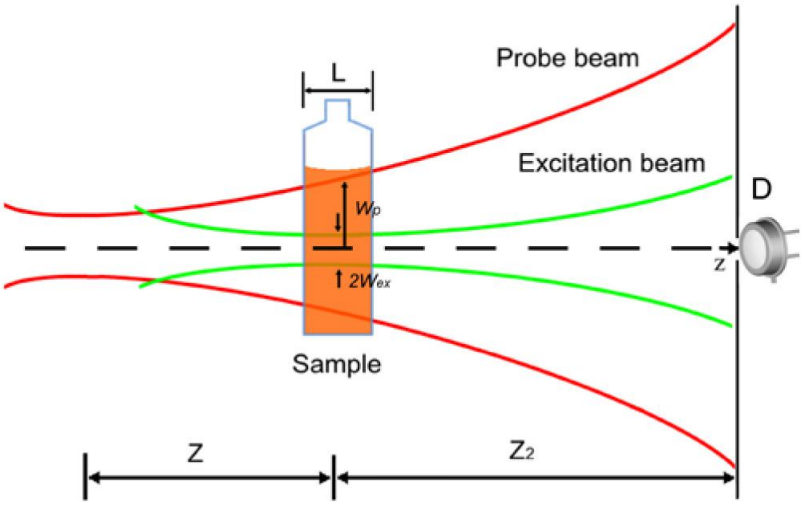

Source: adapted from (ESTUPIÑÁN-LÓPEZ; DOMINGUEZ; ARAUJO, 2013).

4.2.3 Temperature Measurements by TL Methods

The development of TL techniques to temperature analysis provides a useful non invasive tool to acquire the global temperatures of liquids and transparent solids in many applications. The model for laser induced mode-mismatched DTL published by Shen (SHEN; LOWE; SNOOK, 1992) describes the spatial-temporal dependence of temperature variation as:

$$\Delta T(r,t) = \frac{2P_{ext}\alpha}{\pi C_p \rho w_{ex}^2} \int_0^t \frac{1}{1+2t'/t_c} exp\left(-\frac{2r^2/w_{ex}^2}{1+2t/t_c}\right) dt' \ . \tag{4.11}$$

The temperature variation is completely induced by the pump beam, and the characteristic time t_c is obtained by interpolation of equation 4.7. Using the relation 4.8, one can write the above equation as a function of θ (also acquired by interpolation of equation 4.7). Expanding the exponential term in Taylor series $\left(e^{-x} = \sum_{\mu=0}^{\infty}(-x)^{\mu}/\mu!\right)$, the equation 4.11 can be rewritten as:

$$\Delta T(r,t) = -\frac{\theta\kappa_m\lambda}{(dn/dT)} \frac{2}{\pi C_p \rho \ell w_{ex}^2} \int_0^t \sum_{\mu=0}^{\infty} \frac{(-1)^{\mu}(2r^2/w_{ex}^2)^{\mu}}{\mu!} \left(\frac{1}{1+2t'/t_c}\right)^{\mu+1} dt' \ . \tag{4.12}$$

where $\lambda = \lambda_{ex}$ (in case of performing the STL experiment) or $\lambda = \lambda_p$ (in case of performing the DTL experiment). Separating the terms for $\mu = 0$ and $\mu > 0$ and integrating, it is possible to obtain the following equation:

$$\begin{aligned}\Delta T(r,t) = -\frac{\theta\kappa_m\lambda}{(dn/dT)} \frac{t_c}{\pi C_p \rho \ell w_{ex}^2} \left\{ ln\left(1+\frac{2t}{t_c}\right) + \right. \\ \left. \sum_{\mu=1}^{\infty} \frac{(-1)^{\mu}(2r^2/w_{ex}^2)^{\mu}}{\mu.\mu!} \left[1 - \left(\frac{1}{1+2t/t_c}\right)^{\mu}\right] \right\} \ .\end{aligned} \tag{4.13}$$

One can notice that the thermal diffusivity of the sample D_{th} is given by $D_{th} = \kappa_m/C_p\rho$. In addition, the pump beam characteristic time is described by $t_c = w_{ex}^2/4D_{th}$. Hence, equation 4.13 can be written as:

$$\begin{aligned}\Delta T(r,t) = -\frac{\theta\lambda}{4\pi\ell(dn/dT)} \left\{ ln\left(1+\frac{2t}{t_c}\right) + \right. \\ \left. \sum_{\mu=1}^{\infty} \frac{(-2r^2/w_{ex}^2)^{\mu}}{\mu.\mu!} \left[1 - \left(\frac{1}{1+2t/t_c}\right)^{\mu}\right] \right\} \ .\end{aligned} \tag{4.14}$$

Equation 4.14 describes the heat profile that arises from TL experiments. In space, the equation 4.14 describes an almost Gaussian distribution, while in time it increases logarithmically

until saturation (steady-state) is reached. Defining the global temperature of the heated region as the volumetric average temperature of a cylindrical region of radius w_p and length ℓ and applying the *mean value theorem* in equation 4.14, it is possible to obtain:

$$\Delta T_{global} \approx -\frac{(\theta/m)\,\lambda}{4\pi\ell(dn/dT)}\left\{ln\left(1+\frac{2t}{t_c}\right)+\sum_{\mu=1}^{\infty}\frac{(-2)^{\mu}}{\mu(\mu+1)!}\left[1-\left(\frac{1}{1+2t/t_c}\right)^{\mu}\right]\right\}\ . \quad (4.15)$$

For STL measurements, $m = 1$. This is equivalent to take the volumetric average of a cylindrical region of radius w_{ex} (same beam for pumping and probing). If enough time has elapsed, $t \gg t_c$, and equation 4.15 can be approximated as:

$$\Delta T_{global} \approx -\frac{(\theta/m)\,\lambda}{4\pi\ell(dn/dT)}\left[ln\left(\frac{2t}{t_c}\right)+\sum_{\mu=1}^{\infty}\frac{(-2)^{\mu}}{\mu(\mu+1)!}\right]\ . \quad (4.16)$$

Since the summation of equation 4.16 converges to approximately -0.75160 and we can reduce it to:

$$\Delta T_{global} \approx -\frac{(\theta/m)\,\lambda}{4\pi\ell(dn/dT)}\left[ln\left(\frac{2t}{t_c}\right)-\frac{3}{4}\right]\ . \quad (4.17)$$

4.2.4 Associated Heat Loss Measurement

One experimental difficulty one can envisage throughout the measurement of small temperature variations is the loss of energy to the environment. All steady-states discussed so far are a local equilibrium where the influx and outflux of energy from a system cancels out. One way of measuring energy loss of a closed system is by the assessment of decay rate. The rate at which the temperature of a system evolves depends on its energy balance. If its gains are bigger than its losses, the temperature increases with time. If the opposite is true, the temperature decreases. The energy balance is described as:

$$\sum_i m_i C_{p\,i}\frac{dT}{dt} = \sum_i P_{abs\,i} - P_{loss}\ , \quad (4.18)$$

where $P_{abs\,i}$ is the power absorbed by each nanoheater and P_{loss} is the total outflow of energy (dissipated by transfer to an external reservoir). The left-hand side of equation 4.18 represents every mass contribution and its respective heat capacities. If only conductive heat transfer is considered, the dissipated power can be represented as boundary of surface area *S* and heat transfer coefficient *h*, therefore:

$$P_{loss} = hS\Delta T\ . \quad (4.19)$$

Thus, the equation 4.18 can be recast as

$$\frac{d\,(\Delta T)}{dt} = G - B\,(\Delta T)\ . \tag{4.20}$$

Here, *G* is the rate of temperature change (energy absorption) and *B* is the rate constant associated with heat loss. By comparison between equations 4.18 and 4.20, *B* can be written as

$$B = \frac{hS}{\sum_i m_i C_{p\,i}} = \frac{h}{\rho C_p}\frac{S}{V} \tag{4.21}$$

to a domain of overall volume *V*, density ρ and heat capacity C_p. If the laser is turned off, the influx of energy is null (*G* = 0), and the rate constant of heat loss from the system domain to an external reservoir (*B*) is determined by

$$T(t) = T_0 + \Delta T_{max} e^{-Bt} \tag{4.22}$$

One can notice that the temperature decay happens in a characteristic time $\tau = B^{-1}$, reaching the ambient temperature T_0. ΔT_{max} is the temperature when laser excitation ceases. The parameter *B* may be written as $B = -ln[(T(t) - T_0)/\Delta T_{max}]/t$ (RICHARDSON et al., 2009).

Figure 31 describes the thermal behavior of a laser heated gold nanoparticle colloidal sample described by Richardson *et al.* (RICHARDSON et al., 2009). In such experiments, a droplet of a absorbing solution was placed at a thermocouple tip, and temperature increase and relaxation were monitored. The red dashed lines of figure 31 illustrates the interpolation temperature increase data in the droplet. The dashed blue decay line displays the interpolation of thermal relaxation data. The the associated heat loss is obtained by interpolation of equation 4.22.

4.3 EXPERIMENTAL RESULTS

Although thermal-lens techniques have been extensively used to measure a variety of optical and thermal properties in materials, it has never been directly employed as temperature probe. This section presents the results obtained in experimental essays regarding the employment of STL and DTL to measure temperature variations induced in a colloidal sample of gold nanoparticles. The experimental setup is described in figure 32. The experiment comprises of a pump laser (Coherent Compass 215M-20, 20 mW CW @ 532 nm) and a *He-Ne* probe laser (6.5 mW CW @ 633 nm). The pump laser is chopped and passes through a beam expander (f_{L1} = 35 mm and L_2 = 100 mm). After collimation, the pump beam passes through focusing lens

Figure 31 – Thermal excitation (red) and relaxation (blue) obtained by Richardson et al.

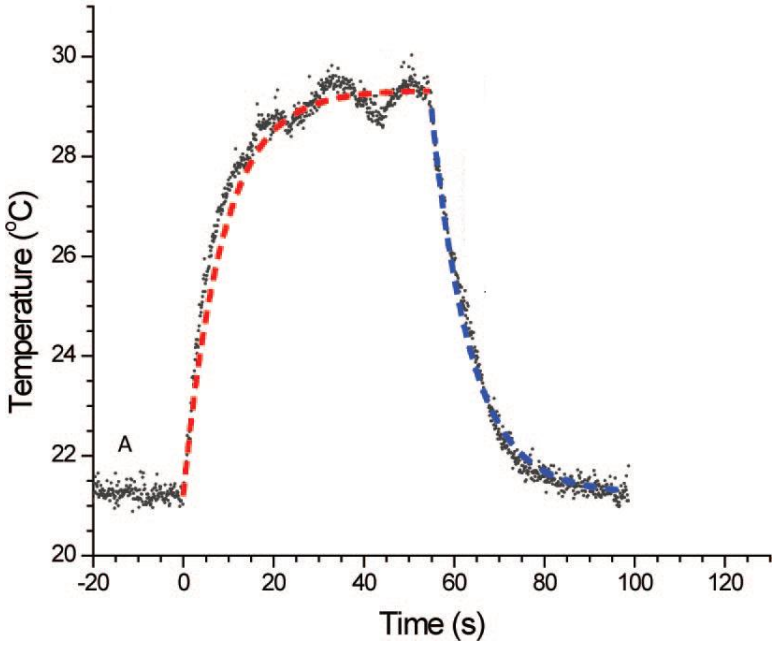

Source: adapted from (RICHARDSON et al., 2009).

(f_{L3} = 150 mm) and is focused at the sample. After interaction with the sample, the pump beam is partially blocked by an aperture before reaching the photodiode PD_1 (*Vishay BPW21R*) for acquisition of STL data. The probe beam travels through a different beam expander (f_{L4} = 25.4 mm and f_{L5} = 45 mm) and is focused at the sample (f_{L6} = 300 mm) and reaches it at an angle of approximately 5° with reference to the pump beam. After the sample, the probe beam suffers attenuation from a neutral density filter and is partially blocked by an aperture before reaching the photodiode PD_2 (*VTB8440BH*).

Figure 32 – Experimental TL setup.

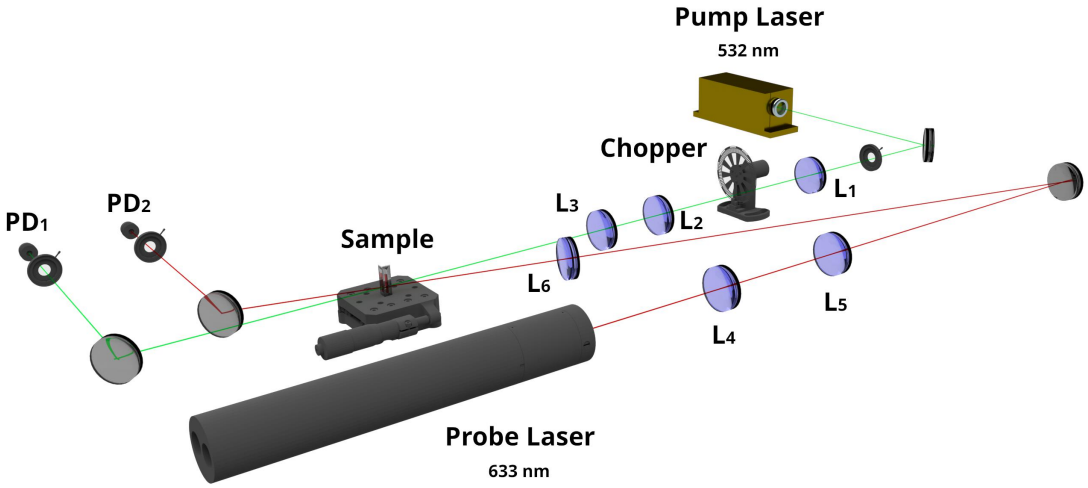

Source: belongs to the author.

TL measurements were performed on a 0.05 mg/mL gold nanospheres (50 nm diameter) aqueous solution from NanoComposix, placed in a cuvette with 2 mm length. The TL setup explores different pump powers, ranging from 3.5 to 14.0 mW. The chopper was operated at 5 Hz with 50% duty cycle, achieving an optical window of 100 ms. The samples included 4 different colloid concentrations, from 0.5 to 2.1 $\times 10^{16}$ m^{-3} with 500 μL each. The waist measurement of the pump and probe beams were carried-out by the knife-edge method (SUZAKI; TACHIBANA, 1975), and waist sizes of $w_{ex} = 20$ μm and $w_p = 74$ μm were obtained, yielding a mode-mismatched factor of about 13.5.

The samples were spectroscopically examined before and after the experiments were performed to assure that the thermal assessment didn't influence nanoparticle stability. The spectra were analyzed by the *Ocean Optics USB2000* spectrometer, capable of performing visible and NIR spectroscopy. Figure 33a depicts the normalized absorbance spectrum of 50 nm gold nanosphere colloidal sample with concentration of 2.1×10^{16} m^{-3}. The graph shows a peak around 530 nm, compared to the 528 nm maximum specified by the manufacturer (NANOCOMPOSIX, 2016). To assure the influence of absorbing nanoparticles on the induction of thermal lens effect, a sample containing distilled water was placed in the experimental setup and its thermal response was evaluated. Water is notable for presenting low thermal-optic effects, and thus its TL signal confers very low excursion as shown in figure 33b. The distilled water sample was excited by 14.2 mW, yielding a global thermal variation of 0.01 ^{o}C in the pump beam region.

Figure 33 – Sample characteristics. (a) Normalized absorbance spectrum of colloidal sample with 50 nm Au nanospheres. (b) Dual thermal lens signal induced in distilled water sample.

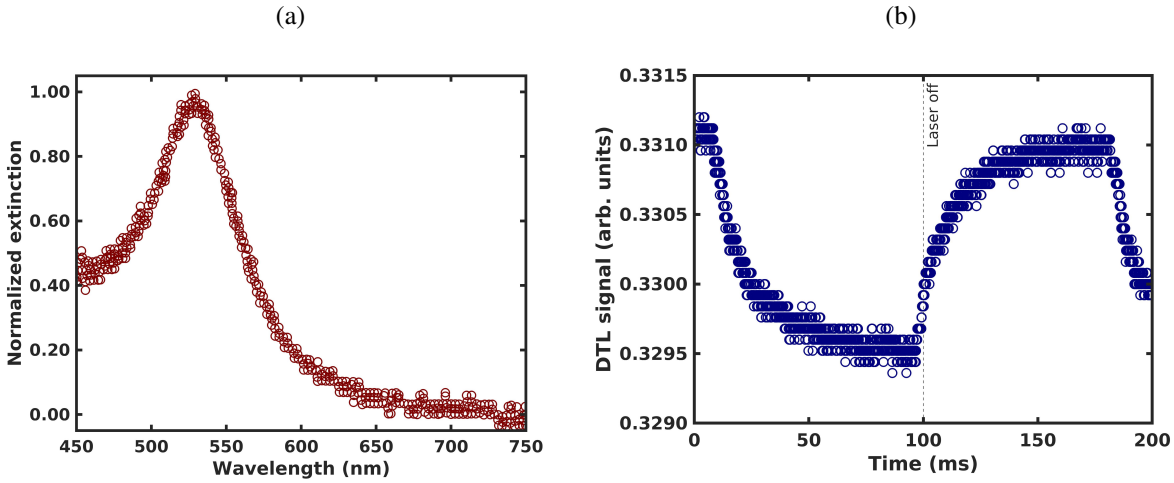

Source: belongs to the author.

In the TL experiment, as the thermally induced refractive index gradient is formed, a time dependent divergent lens effect arises due to the negative nature of the thermo-optic coefficient. The signal that reaches the photodetectors can thus be interpreted as the interaction of the pump

beam with two lenses: the beam focusing lens and the thermal lens induced at the sample. Sample placement after the focusing lens focal position confers a decreasing beam intensity at the photodetector as the lens effect takes place. When the pump laser beam is blocked, the thermal effect relaxes and the probe beam intensity at the detection plane rises, returning to its initial value. Figure 34 depicts the dynamics of the measured TL signal in the single beam experiment.

Figure 34 – STL experimental data (scatter plot) for $C_{np} = 2.1 \times 10^{16}$ m^{-3} and $P_{exc} = 14$ mW. The solid line depicts the best fit to the experimental data.

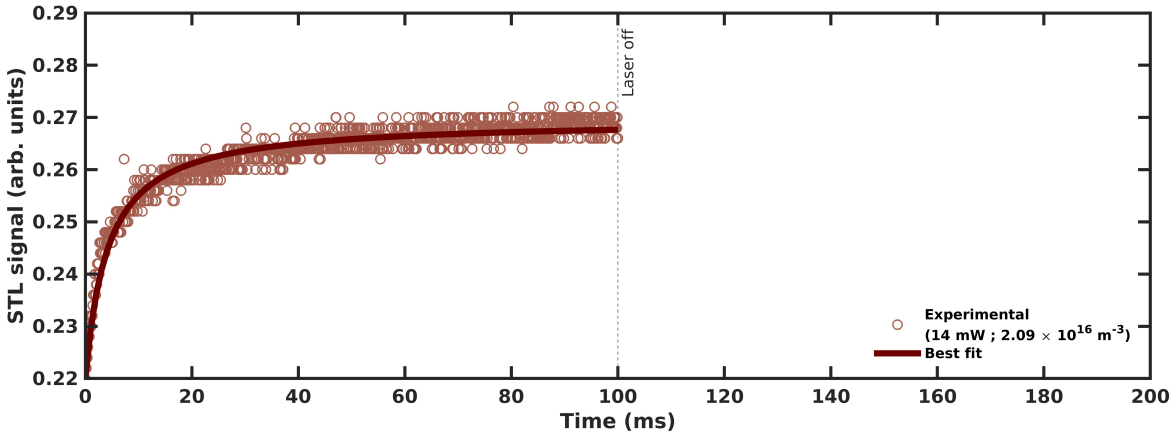

Source: belongs to the author.

The interpolating the experimental data using equation 4.6, it's possible to obtain θ and t_c. This allows the determination of the averaged time dependent global temperature variation of the colloidal sample employing equation 4.16. Figure 35a shows the experimental behavior of the global temperature variation for sample concentration of 2.1 $\times 10^{16}$ m^{-3} and various pumping powers. Figure 35b shows the experimental global temperature variation in the steady-state ($t = 100$ ms) obtained for different pumping powers and several NP concentrations. As expected, higher temperatures are obtained increasing excitation power. The dashed lines in Figure 35b indicates the theoretical values obtained from equation 4.1. Figure 35c is a colormap depicting the theoretical global temperature variation expected from equation 4.15 and the experimental values obtained from STL evaluation (circles) at $t = 100$ ms. The circles are filled with the color representing its experimental temperature variation (see colorbar), which indicates a good agreement between the experimental and theoretical values.

The experimental values shows good agreement with the theory, and the measurement error associated to temperature variation was $\pm$ 0.04 ºC for sample concentration of 2.1 $\times$ 10^{16} m^{-3} and $\pm$ 0.01 ºC for sample concentrations of 1.2 $\times$ 10^{16} m^{-3} and 0.8 $\times$ 10^{16} m^{-3}. The temperatures values obtained with the 0.5 $\times$ 10^{16} m^{-3} NP concentration sample showed an error of $\pm$ 0.03 ºC.

Figure 36 illustrates the TL signal acquired in the dual beam setup. From it, it is possible

Figure 35 – Temperature measurement by single beam TL technique. (a) Averaged global temperature variation for the 2.1 $\times 10^{16}$ m^{-3} colloidal sample concentration at various laser excitation powers. (b) Averaged temperature variation as function of pumping power for several NP concentrations, at 100 ms. (c) Theoretical averaged global temperature variation colormap, at 100 ms. The experimental data are denoted by the scattered circles..

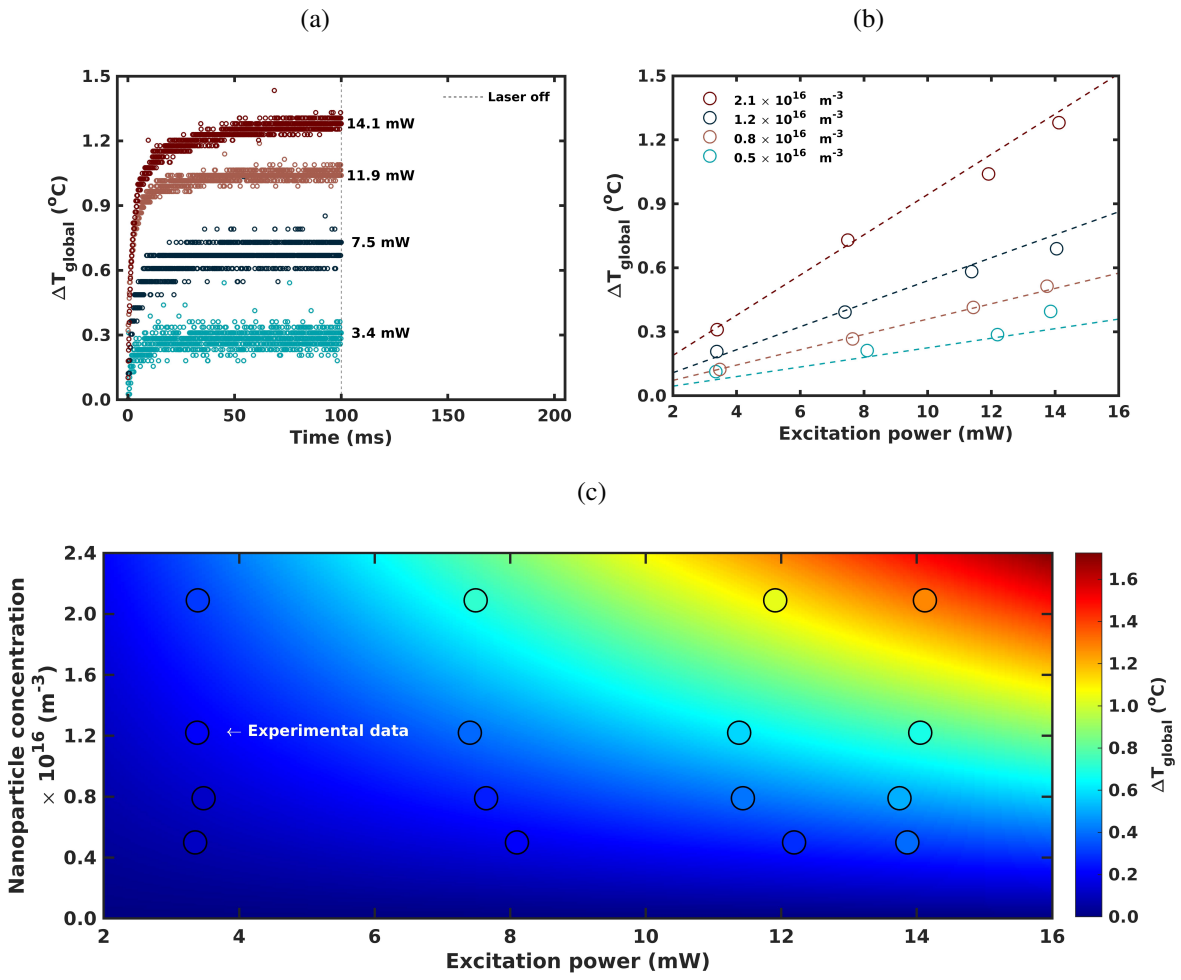

Source: belongs to the author.

to notice that the DTL experiment confers a larger TL signal excursion, which also leads to a larger signal-to-noise ratio. Furthermore, the DTL setup allows the assessment of thermal relaxation in the sample. The solid line is the best fit of the thermal lens formation process.

Figure 36 – DTL experimental data (scatter plot) for $C_{np} = 2.1 \times 10^{16}$ m^{-3} and $P_{exc} = 14$ mW. The solid line depicts the best fit to the experimental data during thermal lens formation.

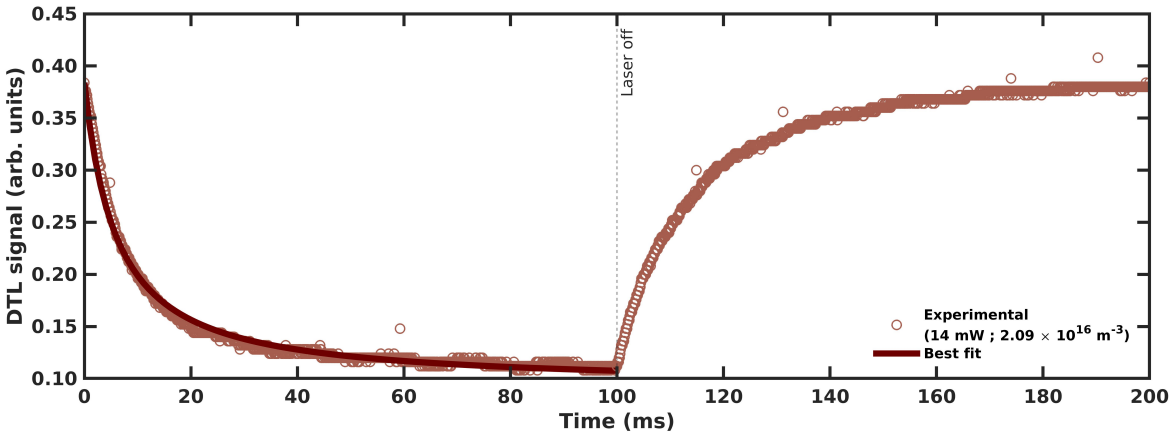

Source: belongs to the author.

The process of temperature acquisition by DTL follows a four-step transformation from DTL signal to temperature profile. First TL formation signal is separated from the TL relaxation signal. The signal obtained within pump excitation time is then fitted by equation 4.7 to produce the thermal lens parameters θ and t_c. From the acquired TL parameters, equation 4.16 can be explored to obtain the thermal response of the sample. Similarly to the STL case, Figure 37a shows the experimental behavior of the global temperature variation for sample concentration of 2.1 $\times 10^{16}$ m^{-3} and various pumping powers. Notice the presence of the thermal relaxation dynamics. Again, Figure 37b shows the experimental global temperature variation in the steady-state ($t = 100$ ms) obtained for different pumping powers and several NP concentrations with the dashed lines depicting the theoretical values obtained from equation 4.1. Figure 37c is a colormap showing the theoretical global temperature variation expected from equation 4.15 and the experimental values obtained from DTL evaluation (circles) at $t = 100$ ms. The circles are filled with the color representing its experimental temperature variation (see colorbar).

The experimental values aren't as good as the obtained by the STL technique, even though good agreement with theoretical values is achieved. Here, the measurement error associated to temperature variation was $\pm$ 0.02 ^{o}C for sample concentration of 2.1 $\times$ 10^{16} m^{-3} and $\pm$ 0.07 ^{o}C for sample concentrations of 1.2 $\times$ 10^{16} m^{-3}. For temperatures values obtained with 0.8 $\times$ 10^{16} m^{-3} and 0.5 $\times$ 10^{16} m^{-3} NP concentrations the error was $\pm$ 0.01 ^{o}C. In both cases, global temperature variations up to 1.28 ^{o}C were observed. Also, the assessment of the TL technique shows that the temperature variation of the colloidal sample and excitation power are linearly dependent, in accordance with theoretical expectations.

Figure 37 – Temperature measurement by dual beam TL technique. (a) Averaged global temperature variation for the 2.1 $\times 10^{16}$ m^{-3} colloidal sample concentration at various laser excitation powers. (b) Averaged temperature variation as function of pumping power for several NP concentrations, at 100 ms. (c) Theoretical averaged global temperature variation colormap, at 100 ms. The experimental data are denoted by the scattered circles.

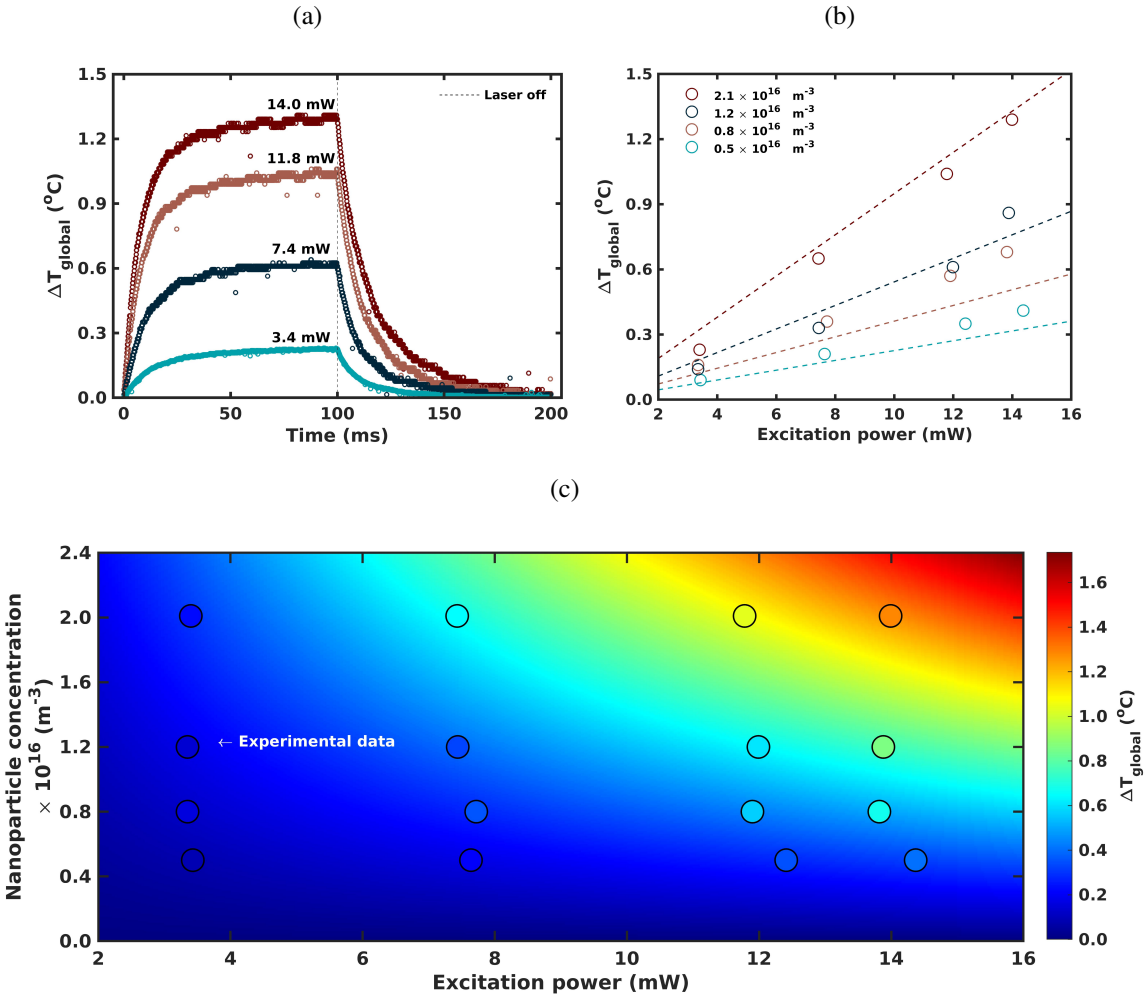

Source: belongs to the author.

The assessment of sample thermal relaxation through temperature decay rate is associated to the heat lost by convection to the surrounding medium and can be explored in dual beam TL experiments. Interpolating experimental temperature relaxation curves using equation 4.22 yields the heat loss parameter B. Since the beam diameter in the sample is very small in comparison to the cuvette dimensions, it is safe to assume that convection occurs only in the faces where the laser beam enters and exits the sample. For all measurements, the rate of constant heat loss to the surroundings averages $B = 68.3\ \mathrm{s}^{-1}$. In systems where high temperatures are achieved, convective heat loss becomes important since it is proportional to temperature variation between the sample and surrounding medium. The heat loss parameter, thus, is decisive in estimating the temperatures achievable by the sample in the steady-state.

From the global temperature variation, it is possible to estimate the intermediate steady-state temperature variation of each nanoparticle (ΔT_{np}) using equation 4.2, since the steady-state global temperature variation (ΔT_{global}) is established by the contribution of each individual nanoheater. Using the experimental global temperature data obtained from experimental TL measurements with known sample and laser parameters, the average NP temperature variation $\langle \Delta T_{np} \rangle$ can be obtained experimentally for different excitation powers. Since the intermediate steady-state temperature variation is independent of NP concentration (see equation 4.1), the ΔT_{np} values were averaged for the different colloidal sample concentrations available. Figures 38a and 38b depicts the average intermediate steady-state temperature variation of individual NPs (before collective heating) for various excitation powers. The faint stripe indicates the error, considering the experimental ΔT_{global} values obtained with different NP sample concentrations. The dashed line in figures 38a and 38b correspond to theoretical ΔT_{np} results, and demonstrates accordance with experimental findings. As expected, the nanoparticle temperature rises linearly as excitation power increases.

Figure 38 – Average intermediate steady-state temperature variation of individual NPs. (a) From STL measurements. (b) From DTL measurements.

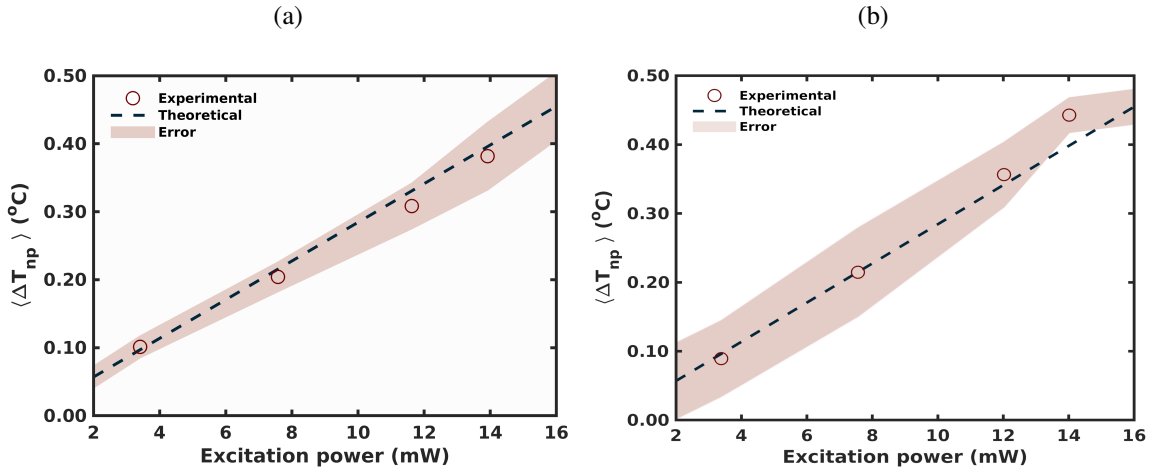

Source: belongs to the author.

It is important to notice that despite TL setups being capable of measuring only small temperature changes on optically-heated metallic colloids, our alternative approach employing TL measurements introduce a new thermometric technique capable of obtaining the localized temperature variation of nanoheaters with low cost and good thermal resolution. Thereafter, we establish a technique to analyze the thermo-optic performance of optically transparent samples containing metallic colloids.

5 CONCLUSIONS AND FUTURE PROSPECTS

5.1 CONCLUSIONS

The implementation of optimal metallic nanoparticles for heat generation can provide a substantial increase in the effectiveness of photothermal therapies. A new methodology to optimize heat generation by nanoparticle means was described, and gold nanorods were optimized to both nanosecond pulse and continuous excitation. Two figures of merit were identified to nanosecond and continuous pumping. The Joule Number (J_0) and the Steady-state Factor (S^2F) are adequate for most nanoparticle morphologies and material compositions. The results obtained by FEM simulations show that for nanosecond pulses, the optimal nanorod dimensions are D = 11 nm and L = 45 nm (AR $\approx$ 4.0) for the 800 nm laser line located at the first biological transparency window, and D = 9 nm and L = 60 nm (AR $\approx$ 6.4) for the 1064 nm laser line located at the second biological transparency window. For continuous excitation, however, the S^2F indicated the use of nanostructures with longer lengths (volume), which conveys an increase in the steady state temperature reachable by the nanorod. The optimal dimensions of gold nanorods found for the continuous excitation regime were L = 105 nm (D = 26 nm) for optimal heating generation at 800 nm and L = 180 nm (D = 28 nm) in case of optimal heating generation at 1064 nm.

Therefore, both figures of merit presents substantial potential and may be applied to optimize nanoheaters other than gold nanorods. The use of optimal nanoheaters may imply a reduction in the amount of assimilated nanoparticles required to produce a significant temperature variation enough to induce cell death in PTT applications. The administration of a dose containing smaller amounts of nanoparticles may lead to less cytotoxicity, while simultaneously requiring smaller tumor uptake of nanoheaters. Such factors may be capable of reducing the risks associated to renal clearance and shorten the way for clinical applications of metallic nanoparticle mediated thermal therapies.

A new and simple method to characterize the thermal-optical properties of metallic nanoparticle colloids was described. The single beam and dual-beam mode-mismatched thermal lens technique are good and simple methods to optical heating of nanoparticle colloids. This technique presents high accuracy, being able to detect temperature variations as low as 0.01 ^{o}C. The mode-mismatched DTL method also enables the the assessment of parameters beyond thermal variations. For instance, its pump-probe configuration allows for real-time appraisal of heat lost to the surrounding medium. The global temperature variation obtained by this approach can be employed to estimate the steady-state localized temperature reached by a single nanoheater before thermalization of the pumped region, yielding a practical procedure to quantify the Steady-state Factor. Moreover, measurement of the transient heat loss factor *B* is

an interesting tool for the evaluation of temperature dynamics in in-vitro essays. Such analysis allows a better estimation of the temperatures reached by nanoparticle mediated heating in in-vivo systems.

In this work, it was possible to measure average global temperature variations up to 1.28 ºC in the laser pumped region. The experimental bulk temperature variations presented a linear dependence on either the incident pump power and metallic colloidal solution concentration, as predicted by the theoretical thermal-lens and heating of a nanoparticle ensemble models. Such results indicate that STL and DTL can be explored as a powerful tool for thermal analysis of nanoheaters. Concerning themo-optical conversion of energy, in comparison to thermal imaging cameras and thermocouples, TL methods presents higher accuracy and a fast response that allows real-time sample evaluation. Additionally, the technique bestow the capacity of undergoing refinements, allowing its applications on a larger variety of samples and optical regimes of excitation.

5.2 FUTURE PROSPECTS

In possession of the two figures of merit for nanoheater selection, the optimization of different gold nanoparticles morphologies, such as spherical nanoshells, nanocages, nanodisks and nanoprisms must be performed to yield the best dimensions suitable to high performance heat generation and photothermal therapy applications. Moreover, the figures of merit must also be extended for non-metallic nanoheaters, such as semiconductor nanoparticles and other materials that presents radiative damping.

Although the figures of optimization delivers the best nanoparticle dimensions for heat generation to a given morphology, it does not assure that the optimal nanoparticle sizes can undergo renal clearance in clinical applications. The exploration of different nanostructures with distinct surface charges may allow a better excretion of nanoparticles. Charged coupled plasmon (CCP) and charged transfer plasmon (CTP) structures can be investigated to the development of human-friendly nanoplataforms for photothermal therapies. CCP and CTP crystals can present absorption cross-sections comparable to bigger particles, while simultaneously showing plasmon peak at the NIR region, rendering a convenient morphology for PTT applications. The possibility of breaking CCP and CTP nanocrystals into smaller fragments is another encouraging feature that may lead to breakthrough in PTT.

Even though thermal-lens techniques have seen extensive use to measure a variety of optical and thermal properties in materials, it has never been directly employed as temperature probe. An electronic compact device device to perform automatic nanoparticle colloid temperature measurements employing STL is already under development. The DTL technique can be modified to evaluate the temperature dynamics at the nanosecond scale. Such feat would allow the use of DTL to experimentally appraise the Joule number of nanoheaters, as well as the emergence of superheating phenomena around a nanoparticle. The appearance of superheating in

plasmonic particles excited by nanosecond laser pulses can lead to a further reduction in energy density needed to induce cell death. The DTL model for the assessment of thermal variations can be easily modified to account for quantum yield in radiative samples, providing a technique suitable for non-metallic colloidal nanoparticle solutions.

TL measurements will be employed to experimentally analyze the thermo-optic characteristics of optimal and non-optimal Au nanorods described in this work.

5.3 CONGRESS CONTRIBUTIONS

- **T. L. Pedrosa**, C. E. E. Lopez, R. E. de Araujo. Characterization of Metallic Nanoparticle Colloids by Thermal Lens Spectroscopy, *XIV Simpósio de Lasers e suas Aplicações*, Recife-PE, Brazil, 2019.
- **T. L. Pedrosa**, S. Farooq and R. E. de Araujo. Selecting High Performance Plasmonic Nanostructures for Photothermal Therapy, *2020 OSA Biophotonics Congress: Biomedical Optics*, Fort Lauderdale-FL, USA. (*Accepted*)

BIBLIOGRAPHY

ABADEER, N. S.; MURPHY, C. J. Recent progress in cancer thermal therapy using gold nanoparticles. **The Journal of Physical Chemistry C**, American Chemical Society (ACS), v. 120, n. 9, p. 4691–4716, fev. 2016. Disponível em: <https://doi.org/10.1021/acs.jpcc.5b11232>. Citado 2 vezes nas páginas 39 and 46.

ARAÚJO, C. B. de; GOMES, A. S. L.; BOUDEBS, G. Techniques for nonlinear optical characterization of materials: a review. **Reports on Progress in Physics**, IOP Publishing, v. 79, n. 3, p. 036401, fev. 2016. Disponível em: <https://doi.org/10.1088/0034-4885/79/3/036401>. Citado na página 60.

ASHCROFT, N. W.; MERMIN, N. D. **Solid State Physics**. Cengage Learning, 2011. 1-27 p. ISBN 9788131500521. Disponível em: <https://books.google.com.br/books?id=x_s_YAAACAAJ>. Citado na página 27.

BAESSO, M.; SHEN, J.; SNOOK, R. D. Time-resolved thermal lens measurement of thermal diffusivity of soda—lime glass. **Chemical Physics Letters**, v. 197, p. 255–258, 09 1992. Citado na página 60.

BAFFOU, G. **Thermoplasmonics Heating Metal Nanoparticles Using Light**. [S.l.]: Cambridge University Press, 2017. Citado 6 vezes nas páginas 30, 35, 37, 39, 42, and 45.

BAFFOU, G. et al. Thermal imaging of nanostructures by quantitative optical phase analysis. **ACS Nano**, American Chemical Society (ACS), v. 6, n. 3, p. 2452–2458, fev. 2012. Disponível em: <https://doi.org/10.1021/nn2047586>. Citado na página 55.

BAFFOU, G.; GIRARD, C.; QUIDANT, R. Mapping heat origin in plasmonic structures. **Physical Review Letters**, American Physical Society (APS), v. 104, n. 13, abr. 2010. Disponível em: <https://doi.org/10.1103/physrevlett.104.136805>. Citado na página 55.

BAFFOU, G. et al. Super-heating and micro-bubble generation around plasmonic nanoparticles under CW illumination. **The Journal of Physical Chemistry C**, American Chemical Society (ACS), v. 118, n. 9, p. 4890–4898, jan. 2014. Disponível em: <https://doi.org/10.1021/jp411519k>. Citado na página 23.

BAFFOU, G.; QUIDANT, R.; ABAJO, J. G. de. Nanoscale control of optical heating in complex plasmonic systems. **ACS nano**, v. 4, p. 709–16, 02 2010. Citado na página 45.

BECKER, J. et al. The optimal aspect ratio of gold nanorods for plasmonic bio-sensing. **Plasmonics**, v. 5, p. 161–167, 06 2010. Citado na página 36.

BERCIAUD, S. et al. Observation of intrinsic size effects in the optical response of individual gold nanoparticles. **Nano Letters**, American Chemical Society (ACS), v. 5, n. 3, p. 515–518, mar. 2005. Disponível em: <https://doi.org/10.1021/nl050062t>. Citado na página 28.

BERNAL-ALVARADO, J. et al. Thermal diffusivity measurements in vegetable oils with thermal lens technique. **Review of Scientific Instruments**, AIP Publishing, v. 74, n. 1, p. 697–699, jan. 2003. Disponível em: <https://doi.org/10.1063/1.1517726>. Citado na página 60.

BEVERSLUIS, M. R.; BOUHELIER, A.; NOVOTNY, L. Continuum generation from single gold nanostructures through near-field mediated intraband transitions. **Physical Review B**, American Physical Society (APS), v. 68, n. 11, set. 2003. Disponível em: <https://doi.org/10.1103/physrevb.68.115433>. Citado na página 27.

BOHREN, C.; HUFFMAN, D. R. **Absorption and Scattering of Light by Small Particles**. [S.l.]: Wiley Science Paperback Series, 1983. Citado 2 vezes nas páginas 31 and 32.

BOLAÑOS, K.; KOGAN, M. J.; ARAYA, E. Capping gold nanoparticles with albumin to improve their biomedical properties. **International Journal of Nanomedicine**, Informa UK Limited, Volume 14, p. 6387–6406, ago. 2019. Disponível em: <https://doi.org/10.2147/ijn.s210992>. Citado na página 36.

BONI, L. D.; MENDONÇA, C. R. Study of absorption spectrum and dynamics evaluation of the indocyanine-green first singlet excited state. **Journal of Physical Organic Chemistry**, Wiley, v. 24, n. 8, p. 630–634, nov. 2010. Disponível em: <https://doi.org/10.1002/poc.1800>. Citado na página 47.

BORGIA, I. et al. Heterogeneous distribution of metal nanocrystals in glazes of historical pottery. **Applied Surface Science**, v. 185, p. 206–216, 01 2002. Citado 2 vezes nas páginas 21 and 22.

BOUTOPOULOS, C.; BERGERON, E.; MEUNIER, M. Cell perforation mediated by plasmonic bubbles generated by a single near infrared femtosecond laser pulse. **Journal of Biophotonics**, Wiley, v. 9, n. 1-2, p. 26–31, jul. 2015. Disponível em: <https://doi.org/10.1002/jbio.201500135>. Citado na página 23.

BRONGERSMA, M. L.; HALAS, N. J.; NORDLANDER, P. Plasmon-induced hot carrier science and technology. **Nature Nanotechnology**, Springer Science and Business Media LLC, v. 10, n. 1, p. 25–34, jan. 2015. Disponível em: <https://doi.org/10.1038/nnano.2014.311>. Citado na página 40.

BUCHARSKAYA, A. et al. Towards effective photothermal/photodynamic treatment using plasmonic gold nanoparticles. **International Journal of Molecular Sciences**, MDPI AG, v. 17, n. 8, p. 1295, ago. 2016. Disponível em: <https://doi.org/10.3390/ijms17081295>. Citado na página 46.

BUFFETT, C. E.; MORRIS, M. D. Thermal lens detection for liquid chromatography. **Anal. Chem. (Wash.); ISSN 0003-2700; USA; DA. 1982; Vol. 54; No 11; PP. 1824-1825; Bibl. 11 Ref.**, 1982. Citado na página 60.

CAMARA, A. R. et al. Dengue immunoassay with an LSPR fiber optic sensor. **Optics Express**, The Optical Society, v. 21, n. 22, p. 27023, out. 2013. Disponível em: <https://doi.org/10.1364/oe.21.027023>. Citado na página 23.

CARATTINO, A.; CALDAROLA, M.; ORRIT, M. Gold nanoparticles as absolute nanothermometers. **Nano Letters**, American Chemical Society (ACS), v. 18, n. 2, p. 874–880, jan. 2018. Disponível em: <https://doi.org/10.1021/acs.nanolett.7b04145>. Citado na página 26.

CARLSON, M. T.; GREEN, A. J.; RICHARDSON, H. H. Superheating water by CW excitation of gold nanodots. **Nano Letters**, American Chemical Society (ACS), v. 12, n. 3, p. 1534–1537, fev. 2012. Disponível em: <https://doi.org/10.1021/nl2043503>. Citado na página 23.

CARLSON, M. T.; KHAN, A.; RICHARDSON, H. H. Local temperature determination of optically excited nanoparticles and nanodots. **Nano Letters**, American Chemical Society (ACS), v. 11, n. 3, p. 1061–1069, mar. 2011. Disponível em: <https://doi.org/10.1021/nl103938u>. Citado na página 55.

CHEN, H. et al. Gold nanorods and their plasmonic properties. **Chem. Soc. Rev.**, Royal Society of Chemistry (RSC), v. 42, n. 7, p. 2679–2724, 2013. Disponível em: <https://doi.org/10.1039/c2cs35367a>. Citado na página 36.

CHEN, J. et al. Gold nanocages as photothermal transducers for cancer treatment. **Small**, Wiley, v. 6, n. 7, p. 811–817, abr. 2010. Disponível em: <https://doi.org/10.1002/smll.200902216>. Citado na página 46.

CHEN, J. et al. Gold nanocages: bioconjugation and their potential use as optical imaging contrast agents. **Nano Letters**, American Chemical Society (ACS), v. 5, n. 3, p. 473–477, fev. 2005. Disponível em: <https://doi.org/10.1021/nl047950t>. Citado na página 47.

CHEN, Y.; MUNECHIKA, K.; GINGER, D. S. Dependence of fluorescence intensity on the spectral overlap between fluorophores and plasmon resonant single silver nanoparticles. **Nano Letters**, American Chemical Society (ACS), v. 7, n. 3, p. 690–696, mar. 2007. Disponível em: <https://doi.org/10.1021/nl062795z>. Citado na página 22.

CHOI, H. S. et al. Renal clearance of quantum dots. **Nature Biotechnology**, Springer Science and Business Media LLC, v. 25, n. 10, p. 1165–1170, set. 2007. Disponível em: <https://doi.org/10.1038/nbt1340>. Citado na página 54.

CLARK, B. D. et al. Aluminum nanocubes have sharp corners. **ACS Nano**, American Chemical Society (ACS), v. 13, n. 8, p. 9682–9691, ago. 2019. Disponível em: <https://doi.org/10.1021/acsnano.9b05277>. Citado na página 36.

CLIMENT-FONT, A. Commentary: Luster ceramics: a 9th century ad nanotechnology. **Journal of Nanophotonics**, v. 6, p. 0501–, 10 2012. Citado na página 21.

COLOMBAN, P. The use of metal nanoparticles to produce yellow, red and iridescent colour, from bronze age to present times in lustre pottery and glass: Solid state chemistry, spectroscopy and nanostructure. **Journal of Nano Research**, v. 8, p. 109–132, 07 2010. Citado na página 20.

COMEAU, D.; HACHÉ, A.; MELIKECHI, N. Reflective thermal lensing and optical measurement of thermal diffusivity in liquids. **Applied Physics Letters**, AIP Publishing, v. 83, n. 2, p. 246–248, jul. 2003. Disponível em: <https://doi.org/10.1063/1.1589199>. Citado na página 60.

COMSOL. **The Finite Element Method (FEM)**. 2016. <https://br.comsol.com/multiphysics/finite-element-method>. [Online; accessed 04-January-2019]. Citado na página 104.

CORONADO, E.; SCHATZ, G. Surface plasmon broadening for arbitrary shape nanoparticles: A geometrical probability approach. **The Journal of Chemical Physics**, v. 119, p. 3926–3934, 08 2003. Citado na página 28.

CRUZ, R. et al. Ultra-sensitive thermal lens spectroscopy of water. **Optics Letters**, v. 34, p. 1882–4, 07 2009. Citado na página 60.

CRUZ, R. A.; PILLA, V.; CATUNDA, T. Quantum yield excitation spectrum (UV-visible) of CdSe/ZnS core-shell quantum dots by thermal lens spectrometry. **Journal of Applied Physics**, AIP Publishing, v. 107, n. 8, p. 083504, abr. 2010. Disponível em: <https://doi.org/10.1063/1.3343517>. Citado na página 60.

D., K. et al. Thermal lens in a liquid sample with focal length controllable by bulk temperature. **Applied Physics B**, Springer Science and Business Media LLC, v. 122, n. 5, maio 2016. Disponível em: <https://doi.org/10.1007/s00340-016-6429-5>. Citado na página 60.

DAI, Z. (Ed.). **Advances in Nanotheranostics I**. Springer Berlin Heidelberg, 2016. Disponível em: <https://doi.org/10.1007/978-3-662-48544-6>. Citado na página 47.

DEKA, N. et al. Enhancing solar cell efficiency with plasmonic behavior of double metal nanoparticle system. **Vacuum**, Elsevier BV, v. 152, p. 285–290, jun. 2018. Disponível em: <https://doi.org/10.1016/j.vacuum.2018.03.026>. Citado na página 32.

DERKACHOVA, A.; KOLWAS, K.; DEMCHENKO, I. Dielectric function for gold in plasmonics applications: Size dependence of plasmon resonance frequencies and damping rates for nanospheres. **Plasmonics**, v. 11, n. 3, p. 941–951, Jun 2016. ISSN 1557-1963. Disponível em: <https://doi.org/10.1007/s11468-015-0128-7>. Citado na página 27.

DING, X. et al. Surface plasmon resonance enhanced light absorption and photothermal therapy in the second near-infrared window. **Journal of the American Chemical Society**, American Chemical Society (ACS), v. 136, n. 44, p. 15684–15693, out. 2014. Disponível em: <https://doi.org/10.1021/ja508641z>. Citado na página 22.

DJOROVIĆ, A. et al. Accurate modeling of the polarizability of dyes for electromagnetic calculations. **ACS Omega**, American Chemical Society (ACS), v. 2, n. 5, p. 1804–1811, maio 2017. Disponível em: <https://doi.org/10.1021/acsomega.7b00171>. Citado na página 47.

DOUGHTY, A. et al. Nanomaterial applications in photothermal therapy for cancer. **Materials**, MDPI AG, v. 12, n. 5, p. 779, mar. 2019. Disponível em: <https://doi.org/10.3390/ma12050779>. Citado na página 26.

DOVICHI, N. J.; HARRIS, J. M. Laser induced thermal lens effect for calorimetric trace analysis. **Analytical Chemistry**, American Chemical Society (ACS), v. 51, n. 6, p. 728–731, maio 1979. Disponível em: <https://doi.org/10.1021/ac50042a034>. Citado na página 59.

DRUDE, P. Zur Elektronentheorie der Metalle. **Annalen der Physik**, Wiley, v. 306, n. 3, p. 566–613, 1900. Disponível em: <https://doi.org/10.1002/andp.19003060312>. Citado na página 26.

ESTELRICH, J.; BUSQUETS, M. Iron oxide nanoparticles in photothermal therapy. **Molecules**, MDPI AG, v. 23, n. 7, p. 1567, jun. 2018. Disponível em: <https://doi.org/10.3390/molecules23071567>. Citado na página 46.

ESTUPIÑÁN-LÓPEZ, C.; DOMINGUEZ, C. T.; ARAUJO, R. E. de. Eclipsing thermal lens spectroscopy for fluorescence quantum yield measurement. **Optics Express**, The Optical Society, v. 21, n. 15, p. 18592, jul. 2013. Disponível em: <https://doi.org/10.1364/oe.21.018592>. Citado 2 vezes nas páginas 60 and 64.

FALCONIERI, M. Thermo-optical effects in z -scan measurements using high-repetition-rate lasers. **Journal of Optics A: Pure and Applied Optics**, IOP Publishing, v. 1, n. 6, p. 662–667, set. 1999. Disponível em: <https://doi.org/10.1088/1464-4258/1/6/302>. Citado na página 60.

FAN, J. H. et al. Biocompatibility study of gold nanoparticles to human cells. In: **IFMBE Proceedings**. Springer Berlin Heidelberg, 2009. p. 870–873. Disponível em: <https://doi.org/10.1007/978-3-540-92841-6_214>. Citado na página 47.

FARADAY, M. X. the bakerian lecture. —experimental relations of gold (and other metals) to light. **Philosophical Transactions of the Royal Society of London**, The Royal Society, v. 147, p. 145–181, jan. 1857. Disponível em: <https://doi.org/10.1098/rstl.1857.0011>. Citado 2 vezes nas páginas 22 and 31.

FAROOQ, S. et al. Engineering a plasmonic sensing platform for candida albicans antigen identification. **Journal of Nanophotonics**, SPIE-Intl Soc Optical Eng, v. 12, n. 03, p. 1, maio 2018. Disponível em: <https://doi.org/10.1117/1.jnp.12.033003>. Citado na página 23.

FARR, E. P. et al. Introduction to time-resolved spectroscopy: Nanosecond transient absorption and time-resolved fluorescence of eosin b. **Journal of Chemical Education**, American Chemical Society (ACS), v. 95, n. 5, p. 864–871, mar. 2018. Disponível em: <https://doi.org/10.1021/acs.jchemed.7b00941>. Citado na página 60.

FENG, Y.; ODEN, J. T.; RYLANDER, M. N. A two-state cell damage model under hyperthermic conditions: Theory and in vitro experiments. **Journal of Biomechanical Engineering**, ASME International, v. 130, n. 4, jun. 2008. Disponível em: <https://doi.org/10.1115/1.2947320>. Citado 2 vezes nas páginas 48 and 49.

FONTANA, J. et al. Rise of the charge transfer plasmon: Programmable concatenation of conductively linked gold nanorod dimers. **ACS Photonics**, American Chemical Society (ACS), v. 3, n. 5, p. 904–911, maio 2016. Disponível em: <https://doi.org/10.1021/acsphotonics.6b00184>. Citado na página 54.

FONTANA, J. et al. Widely tunable infrared plasmonic nanoantennas using directed assembly. **Advanced Optical Materials**, Wiley, v. 5, n. 21, p. 1700335, ago. 2017. Disponível em: <https://doi.org/10.1002/adom.201700335>. Citado na página 54.

FRANK, A. J. et al. Synthesis of silver nanoprisms with variable size and investigation of their optical properties: A first-year undergraduate experiment exploring plasmonic nanoparticles. **Journal of Chemical Education**, American Chemical Society (ACS), v. 87, n. 10, p. 1098–1101, out. 2010. Disponível em: <https://doi.org/10.1021/ed100166g>. Citado na página 36.

FREESTONE, I. et al. The lycurgus cup-a roman nanotechnology. **Gold Bulletin**, v. 40, p. 270–277, 12 2007. Citado 2 vezes nas páginas 20 and 21.

GENÇ, A. et al. Hollow metal nanostructures for enhanced plasmonics: synthesis, local plasmonic properties and applications. **Nanophotonics**, Walter de Gruyter GmbH, v. 6, n. 1, p. 193–213, set. 2016. Disponível em: <https://doi.org/10.1515/nanoph-2016-0124>. Citado na página 36.

GNOLI, A.; RAZZARI, L.; RIGHINI, M. Z-scan measurements using high repetition rate lasers: how to manage thermal effects. **Optics Express**, The Optical Society, v. 13, n. 20, p. 7976, 2005. Disponível em: <https://doi.org/10.1364/opex.13.007976>. Citado na página 60.

GOMES, A. S. L. et al. Thermally managed eclipse Z-scan. **Optics Express**, The Optical Society, v. 15, n. 4, p. 1712, fev. 2007. Disponível em: <https://doi.org/10.1364/oe.15.001712>. Citado na página 60.

GORDON, J. P. et al. Long-transient effects in lasers with inserted liquid samples. **Journal of Applied Physics**, AIP Publishing, v. 36, n. 1, p. 3–8, jan. 1965. Disponível em: <https://doi.org/10.1063/1.1713919>. Citado na página 59.

GOVOROV, A. O. et al. Gold nanoparticle ensembles as heaters and actuators: melting and collective plasmon resonances. **Nanoscale Research Letters**, Springer Science and Business Media LLC, v. 1, n. 1, p. 84–90, jul. 2006. Disponível em: <https://doi.org/10.1007/s11671-006-9015-7>. Citado 2 vezes nas páginas 41 and 43.

GUTIÉRREZ, M. V.; SCARPETTINI, A. F. Kinetic and plasmonic properties of gold nanorods adsorbed on glass substrates. **Colloid and Interface Science Communications**, Elsevier BV, v. 33, p. 100213, nov. 2019. Disponível em: <https://doi.org/10.1016/j.colcom.2019.100213>. Citado na página 36.

HABER, J.; SOKOLOV, K. Synthesis of stable citrate-capped silver nanoprisms. **Langmuir**, American Chemical Society (ACS), v. 33, n. 40, p. 10525–10530, set. 2017. Disponível em: <https://doi.org/10.1021/acs.langmuir.7b01362>. Citado na página 36.

HARRIS, N.; FORD, M. J.; CORTIE, M. B. Optimization of plasmonic heating by gold nanospheres and nanoshells. **The Journal of Physical Chemistry B**, American Chemical Society (ACS), v. 110, n. 22, p. 10701–10707, jun. 2006. Disponível em: <https://doi.org/10.1021/jp0606208>. Citado na página 49.

HEMMER, E. et al. Exploiting the biological windows: current perspectives on fluorescent bioprobes emitting above 1000 nm. **Nanoscale Horizons**, Royal Society of Chemistry (RSC), v. 1, n. 3, p. 168–184, 2016. Disponível em: <https://doi.org/10.1039/c5nh00073d>. Citado 2 vezes nas páginas 46 and 47.

HERRERA, L. J. M. et al. Determination of plasma frequency, damping constant, and size distribution from the complex dielectric function of noble metal nanoparticles. **Journal of Applied Physics**, AIP Publishing, v. 116, n. 23, p. 233105, dez. 2014. Disponível em: <https://doi.org/10.1063/1.4904349>. Citado na página 27.

HIRSCH, L. R. et al. Nanoshell-mediated near-infrared thermal therapy of tumors under magnetic resonance guidance. **Proceedings of the National Academy of Sciences**, Proceedings of the National Academy of Sciences, v. 100, n. 23, p. 13549–13554, nov. 2003. Disponível em: <https://doi.org/10.1073/pnas.2232479100>. Citado na página 46.

HU, C.; WHINNERY, J. R. New thermooptical measurement method and a comparison with other methods. **Applied Optics**, The Optical Society, v. 12, n. 1, p. 72, jan. 1973. Disponível em: <https://doi.org/10.1364/ao.12.000072>. Citado na página 60.

HUANG, L. et al. Plasmonic silver nanoshells for drug and metabolite detection. **Nature Communications**, Springer Science and Business Media LLC, v. 8, n. 1, ago. 2017. Disponível em: <https://doi.org/10.1038/s41467-017-00220-4>. Citado na página 36.

HUSSEIN, A. Applications of nanotechnology to enhance the performance of the direct absorption solar collectors. **Journal of Thermal Engineering**, v. 2, 03 2015. Citado na página 26.

JAIN, P. K. et al. Calculated absorption and scattering properties of gold nanoparticles of different size, shape, and composition: applications in biological imaging and biomedicine. **The Journal of Physical Chemistry B**, American Chemical Society (ACS), v. 110, n. 14, p.

7238–7248, abr. 2006. Disponível em: <https://doi.org/10.1021/jp057170o>. Citado na página 47.

JAQUE, D.; VETRONE, F. Luminescence nanothermometry. **Nanoscale**, Royal Society of Chemistry (RSC), v. 4, n. 15, p. 4301, 2012. Disponível em: <https://doi.org/10.1039/c2nr30764b>. Citado na página 55.

JEON, H. B.; TSALU, P. V.; HA, J. W. Shape effect on the refractive index sensitivity at localized surface plasmon resonance inflection points of single gold nanocubes with vertices. **Scientific Reports**, Springer Science and Business Media LLC, v. 9, n. 1, set. 2019. Disponível em: <https://doi.org/10.1038/s41598-019-50032-3>. Citado na página 36.

JIN, H. et al. Nanoparticles enabled pump-free direct absorption solar collectors. **Renewable Energy**, Elsevier BV, v. 145, p. 2337–2344, jan. 2020. Disponível em: <https://doi.org/10.1016/j.renene.2019.07.108>. Citado na página 26.

JOHNSON, P. B.; CHRISTY, R. W. Optical constants of the noble metals. **Physical Review B**, American Physical Society (APS), v. 6, n. 12, p. 4370–4379, dez. 1972. Disponível em: <https://doi.org/10.1103/physrevb.6.4370>. Citado 3 vezes nas páginas 9, 28, and 29.

JONES, S. et al. Ultrafast modulation of thermoplasmonic nanobubbles in water. **Nano Letters**, American Chemical Society (ACS), v. 19, n. 11, p. 8294–8302, out. 2019. Disponível em: <https://doi.org/10.1021/acs.nanolett.9b03895>. Citado na página 26.

JUSTE, J. P. et al. Gold nanorods: Synthesis, characterization and applications. **Coordination Chemistry Reviews**, Elsevier BV, v. 249, n. 17-18, p. 1870–1901, set. 2005. Disponível em: <https://doi.org/10.1016/j.ccr.2005.01.030>. Citado na página 37.

KEBLINSKI, P. et al. Limits of localized heating by electromagnetically excited nanoparticles. **Journal of Applied Physics**, AIP Publishing, v. 100, n. 5, p. 054305, set. 2006. Disponível em: <https://doi.org/10.1063/1.2335783>. Citado 4 vezes nas páginas 44, 56, 57, and 58.

KELLY, K. L. et al. The optical properties of metal nanoparticles: the influence of size, shape, and dielectric environment. **The Journal of Physical Chemistry B**, American Chemical Society (ACS), v. 107, n. 3, p. 668–677, jan. 2003. Disponível em: <https://doi.org/10.1021/jp026731y>. Citado na página 33.

KREIBIG, U.; VOLLMER, M. Introduction. In: **Optical Properties of Metal Clusters**. Springer Berlin Heidelberg, 1995. p. 1–12. Disponível em: <https://doi.org/10.1007/978-3-662-09109-8_1>. Citado na página 28.

KUMAR, C. (Ed.). **UV-VIS and Photoluminescence Spectroscopy for Nanomaterials Characterization**. Springer Berlin Heidelberg, 2013. Disponível em: <https://doi.org/10.1007/978-3-642-27594-4>. Citado 2 vezes nas páginas 33 and 35.

KUMAR, P.; SRIVASTAVA, R. **Nanomedicine for Cancer Therapy**. Springer International Publishing, 2017. Disponível em: <https://doi.org/10.1007/978-3-319-45826-7>. Citado 2 vezes nas páginas 46 and 48.

LAL, S. et al. Light interaction between gold nanoshells plasmon resonance and planar optical waveguides. **The Journal of Physical Chemistry B**, American Chemical Society (ACS), v. 106, n. 22, p. 5609–5612, jun. 2002. Disponível em: <https://doi.org/10.1021/jp014154s>. Citado na página 36.

LALISSE, A. et al. Quantifying the efficiency of plasmonic materials for near-field enhancement and photothermal conversion. **The Journal of Physical Chemistry C**, American Chemical Society (ACS), v. 119, n. 45, p. 25518–25528, out. 2015. Disponível em: <https://doi.org/10.1021/acs.jpcc.5b09294>. Citado 2 vezes nas páginas 42 and 43.

LEACH, R. A.; HARRIS, J. M. Thermal lens calorimetry: Application to chromatographic detection. **Journal of Chromatography A**, Elsevier BV, v. 218, p. 15–19, nov. 1981. Disponível em: <https://doi.org/10.1016/s0021-9673(00)82041-5>. Citado na página 59.

LEE, J. et al. Highly sensitive localized surface plasmon resonance immunosensor for label-free detection of HIV-1. **Nanomedicine: Nanotechnology, Biology and Medicine**, Elsevier BV, v. 9, n. 7, p. 1018–1026, out. 2013. Disponível em: <https://doi.org/10.1016/j.nano.2013.03.005>. Citado na página 23.

LEITE, R. C. C.; MOORE, R. S.; WHINNERY, J. R. Low absorption measurements by means of the thermal lens effect using an He–Ne laser. **Applied Physics Letters**, AIP Publishing, v. 5, n. 7, p. 141–143, out. 1964. Disponível em: <https://doi.org/10.1063/1.1754089>. Citado na página 59.

LI, J.; LI, C.; AROCA, R. F. Plasmon-enhanced fluorescence spectroscopy. **Chemical Society Reviews**, Royal Society of Chemistry (RSC), v. 46, n. 13, p. 3962–3979, 2017. Disponível em: <https://doi.org/10.1039/c7cs00169j>. Citado na página 22.

LIBERAL, I. et al. Optical trapping in the presence of higher order mode sources and interactions. **Journal of Optics**, v. 16, p. 114024, 11 2014. Citado na página 32.

LINK, S. et al. Laser photothermal melting and fragmentation of gold nanorods: energy and laser pulse-width dependence. **The Journal of Physical Chemistry A**, American Chemical Society (ACS), v. 103, n. 9, p. 1165–1170, mar. 1999. Disponível em: <https://doi.org/10.1021/jp983141k>. Citado na página 23.

LINK, S.; EL-SAYED, M. Shape and size dependence of radiative, non-radiative and photothermal properties of gold nanocrystals. **International Reviews in Physical Chemistry**, v. 19, p. 409 – 453, 07 2000. Citado na página 37.

LINK, S.; WANG, Z. L.; EL-SAYED, M. A. How does a gold nanorod melt? **The Journal of Physical Chemistry B**, American Chemical Society (ACS), v. 104, n. 33, p. 7867–7870, ago. 2000. Disponível em: <https://doi.org/10.1021/jp0011701>. Citado na página 23.

LIU, Y.; CRAWFORD, B. M.; VO-DINH, T. Gold nanoparticles-mediated photothermal therapy and immunotherapy. **Immunotherapy**, Future Medicine Ltd, v. 10, n. 13, p. 1175–1188, set. 2018. Disponível em: <https://doi.org/10.2217/imt-2018-0029>. Citado na página 46.

LOCATELLI, E.; MONACO, I.; FRANCHINI, M. C. Surface modifications of gold nanorods for applications in nanomedicine. **RSC Advances**, Royal Society of Chemistry (RSC), v. 5, n. 28, p. 21681–21699, 2015. Disponível em: <https://doi.org/10.1039/c4ra16473c>. Citado na página 37.

LONGMIRE, M.; CHOYKE, P. L.; KOBAYASHI, H. Clearance properties of nano-sized particles and molecules as imaging agents: considerations and caveats. **Nanomedicine**, Future Medicine Ltd, v. 3, n. 5, p. 703–717, out. 2008. Disponível em: <https://doi.org/10.2217/17435889.3.5.703>. Citado na página 54.

LÓPEZ-VARELA, K. A. et al. Dynamic infrared thermography of nanoheaters embedded in skin-equivalent phantoms. **Journal of Nanomaterials**, Hindawi Limited, v. 2018, p. 1–8, 2018. Disponível em: <https://doi.org/10.1155/2018/3847348>. Citado 2 vezes nas páginas 55 and 56.

LUCKY, S. S.; SOO, K. C.; ZHANG, Y. Nanoparticles in photodynamic therapy. **Chemical Reviews**, American Chemical Society (ACS), v. 115, n. 4, p. 1990–2042, jan. 2015. Disponível em: <https://doi.org/10.1021/cr5004198>. Citado na página 46.

MA, Z. et al. Applications of gold nanorods in biomedical imaging and related fields. **Chinese Science Bulletin**, Springer Science and Business Media LLC, v. 58, n. 21, p. 2530–2536, maio 2013. Disponível em: <https://doi.org/10.1007/s11434-013-5720-7>. Citado na página 37.

MACKEY, M. A. et al. The most effective gold nanorod size for plasmonic photothermal therapy: Theory and in vitro experiments. **The Journal of Physical Chemistry B**, American Chemical Society (ACS), v. 118, n. 5, p. 1319–1326, jan. 2014. Disponível em: <https://doi.org/10.1021/jp409298f>. Citado na página 49.

MAHDI, N.; FARSINEZHAD, S.; SHANKAR, K. Plasmon-enhanced SERS detection of small molecules: Au nanoparticle-embedded TiO_2 nanotubes as high Q-factor sensor substrates. In: **2017 IEEE SENSORS**. IEEE, 2017. Disponível em: <https://doi.org/10.1109/icsens.2017.8233873>. Citado na página 22.

MAITY, S.; ROY, S. Silver nanoparticles to enhance the efficiency of silicon solar cells. **International Journal of Engineering Science Invention**, v. 2, p. 101–104, 01 2013. Citado na página 32.

MARCANO, A. et al. White light photothermal lens spectrophotometer for the determination of absorption in scattering samples. **Applied Spectroscopy**, SAGE Publications, v. 68, n. 6, p. 680–685, jun. 2014. Disponível em: <https://doi.org/10.1366/13-07385>. Citado na página 60.

MARCANO, A.; LOPER, C.; MELIKECHI, N. Pump–probe mode-mismatched thermal-lens Z scan. **Journal of the Optical Society of America B**, The Optical Society, v. 19, n. 1, p. 119, jan. 2002. Disponível em: <https://doi.org/10.1364/josab.19.000119>. Citado 2 vezes nas páginas 60 and 64.

MASUDA, S. et al. High-resolution imaging of a cell-attached nanointerface using a gold-nanoparticle two-dimensional sheet. **Scientific Reports**, Springer Science and Business Media LLC, v. 7, n. 1, jun. 2017. Disponível em: <https://doi.org/10.1038/s41598-017-04000-4>. Citado na página 22.

MENDES, R. et al. Photothermal enhancement of chemotherapy in breast cancer by visible irradiation of gold nanoparticles. **Scientific Reports**, Springer Science and Business Media LLC, v. 7, n. 1, set. 2017. Disponível em: <https://doi.org/10.1038/s41598-017-11491-8>. Citado na página 46.

MIE, G. Beiträge zur Optik trüber Medien, speziell kolloidaler Metallösungen. **Annalen der Physik**, Wiley, v. 330, n. 3, p. 377–445, 1908. Disponível em: <https://doi.org/10.1002/andp.19083300302>. Citado na página 31.

MOCK, J. J. et al. Shape effects in plasmon resonance of individual colloidal silver nanoparticles. **The Journal of Chemical Physics**, AIP Publishing, v. 116, n. 15, p. 6755–6759, abr. 2002. Disponível em: <https://doi.org/10.1063/1.1462610>. Citado na página 37.

MOON, H. J. et al. Implantable photothermal agents based on gold nanorods-encapsulated microcube. **Scientific Reports**, Springer Science and Business Media LLC, v. 8, n. 1, set. 2018. Disponível em: <https://doi.org/10.1038/s41598-018-31793-9>. Citado na página 46.

MUHAMMAD, M. et al. The use of nanofluids for enhancing the thermal performance of stationary solar collectors: A review. **Renewable and Sustainable Energy Reviews**, v. 63, p. 226–236, 09 2016. Citado na página 26.

MURPHY, M. J.; TORSTENSSON, P. A. Thermal relaxation times: an outdated concept in photothermal treatments. **Lasers in Medical Science**, Springer Science and Business Media LLC, v. 29, n. 3, p. 973–978, out. 2013. Disponível em: <https://doi.org/10.1007/s10103-013-1445-8>. Citado na página 49.

NANOCOMPOSIX. **50 nm Gold Nanospheres, Citrate, NanoXact™**. [S.l.], 2016. Rev. 1. Citado na página 69.

NEVES, W. W. et al. Development of a localized surface plasmon resonance platform for candida albicans antigen identification. In: **2015 SBMO/IEEE MTT-S International Microwave and Optoelectronics Conference (IMOC)**. IEEE, 2015. Disponível em: <https://doi.org/10.1109/imoc.2015.7369224>. Citado na página 23.

NGUYEN, P. T.; ABBOSH, A.; CROZIER, S. Three-dimensional microwave hyperthermia for breast cancer treatment in a realistic environment using particle swarm optimization. **IEEE Transactions on Biomedical Engineering**, Institute of Electrical and Electronics Engineers (IEEE), v. 64, n. 6, p. 1335–1344, jun. 2017. Disponível em: <https://doi.org/10.1109/tbme.2016.2602233>. Citado na página 46.

NIEMZ, M. H. **Laser-Tissue Interactions**. Springer Berlin Heidelberg, 2002. Disponível em: <https://doi.org/10.1007/978-3-662-04717-0>. Citado 2 vezes nas páginas 48 and 49.

NIEMZ, M. H. Laser safety. In: **Biological and Medical Physics, Biomedical Engineering**. Springer Berlin Heidelberg, 2007. p. 249–263. Disponível em: <https://doi.org/10.1007/978-3-540-72192-5_5>. Citado 2 vezes nas páginas 24 and 46.

OKE, S. I. et al. Radiative microwave heating of hyperthermia therapy on breast cancer in a porous medium. **Preprints**, MDPI AG, out. 2018. Disponível em: <https://doi.org/10.20944/preprints201810.0313.v1>. Citado na página 46.

PAN, Y.; BARTNECK, M.; JAHNEN-DECHENT, W. Cytotoxicity of gold nanoparticles. In: **Methods in Enzymology**. Elsevier, 2012. p. 225–242. Disponível em: <https://doi.org/10.1016/b978-0-12-391858-1.00012-5>. Citado na página 48.

PARK, T. J. et al. Development of label-free optical diagnosis for sensitive detection of influenza virus with genetically engineered fusion protein. **Talanta**, Elsevier BV, v. 89, p. 246–252, jan. 2012. Disponível em: <https://doi.org/10.1016/j.talanta.2011.12.021>. Citado na página 23.

PATTANI, V. et al. Role of apoptosis and necrosis in cell death induced by nanoparticle-mediated photothermal therapy. **Journal of Nanoparticle Research**, v. 17, 01 2015. Citado na página 26.

PETROVA, H. et al. On the temperature stability of gold nanorods: comparison between thermal and ultrafast laser-induced heating. **Phys. Chem. Chem. Phys.**, Royal Society of Chemistry (RSC), v. 8, n. 7, p. 814–821, 2006. Disponível em: <https://doi.org/10.1039/b514644e>. Citado na página 23.

PHAN, T. T. V. et al. Photoacoustic imaging-guided photothermal therapy with tumor-targeting HA-FeOOH@PPy nanorods. **Scientific Reports**, Springer Science and Business Media LLC, v. 8, n. 1, jun. 2018. Disponível em: <https://doi.org/10.1038/s41598-018-27204-8>. Citado na página 46.

PITSILLIDES, C. M. et al. Selective cell targeting with light-absorbing microparticles and nanoparticles. **Biophysical Journal**, Elsevier BV, v. 84, n. 6, p. 4023–4032, jun. 2003. Disponível em: <https://doi.org/10.1016/s0006-3495(03)75128-5>. Citado na página 43.

PRENTICE, P. et al. Membrane disruption by optically controlled microbubble cavitation. **Nature Physics**, v. 1, p. 107, 11 2005. Citado na página 26.

PYYKKO, P.; DESCLAUX, J. P. Relativity and the periodic system of elements. **Accounts of Chemical Research**, American Chemical Society (ACS), v. 12, n. 8, p. 276–281, ago. 1979. Disponível em: <https://doi.org/10.1021/ar50140a002>. Citado na página 27.

QUINTANILLA, M. et al. Thermal monitoring during photothermia: hybrid probes for simultaneous plasmonic heating and near-infrared optical nanothermometry. **Theranostics**, Ivyspring International Publisher, v. 9, n. 24, p. 7298–7312, 2019. Disponível em: <https://doi.org/10.7150/thno.38091>. Citado na página 55.

RADLOFF, C.; HALAS, N. J. Plasmonic properties of concentric nanoshells. **Nano Letters**, American Chemical Society (ACS), v. 4, n. 7, p. 1323–1327, jul. 2004. Disponível em: <https://doi.org/10.1021/nl049597x>. Citado na página 36.

REIBOLD, M. et al. Materials - carbon nanotubes in an ancient damascus sabre. **Nature**, v. 444, p. 286, 12 2006. Citado 2 vezes nas páginas 21 and 22.

RICHARDSON, H. H. et al. Experimental and theoretical studies of light-to-heat conversion and collective heating effects in metal nanoparticle solutions. **Nano Letters**, American Chemical Society (ACS), v. 9, n. 3, p. 1139–1146, mar. 2009. Disponível em: <https://doi.org/10.1021/nl8036905>. Citado 4 vezes nas páginas 55, 56, 67, and 68.

RICHARDSON, H. H. et al. Thermooptical properties of gold nanoparticles embedded in ice: characterization of heat generation and melting. **Nano Letters**, American Chemical Society (ACS), v. 6, n. 4, p. 783–788, abr. 2006. Disponível em: <https://doi.org/10.1021/nl060105l>. Citado na página 55.

ROSAL, B. del et al. In vivo luminescence nanothermometry: from materials to applications. **Advanced Optical Materials**, Wiley, v. 5, n. 1, p. 1600508, out. 2016. Disponível em: <https://doi.org/10.1002/adom.201600508>. Citado na página 55.

ROSS, M.; SCHATZ, G. Radiative effects in plasmonic aluminum and silver nanospheres and nanorods. **Journal of Physics D: Applied Physics**, v. 48, 05 2015. Citado 2 vezes nas páginas 28 and 35.

SCHRUM, K. F. et al. Molecular fluorescence thermometry. **Analytical Chemistry**, American Chemical Society (ACS), v. 66, n. 17, p. 2788–2790, set. 1994. Disponível em: <https://doi.org/10.1021/ac00089a030>. Citado na página 55.

SHEIK-BAHAE, M. et al. Sensitive measurement of optical nonlinearities using a single beam. **IEEE Journal of Quantum Electronics**, Institute of Electrical and Electronics Engineers (IEEE), v. 26, n. 4, p. 760–769, abr. 1990. Disponível em: <https://doi.org/10.1109/3.53394>. Citado na página 60.

SHELDON, S. J.; KNIGHT, L. V.; THORNE, J. M. Laser-induced thermal lens effect: a new theoretical model. **Applied Optics**, The Optical Society, v. 21, n. 9, p. 1663, maio 1982. Disponível em: <https://doi.org/10.1364/ao.21.001663>. Citado na página 61.

SHEN, J.; LOWE, R. D.; SNOOK, R. D. A model for CW laser induced mode-mismatched dual-beam thermal lens spectrometry. **Chemical Physics**, Elsevier BV, v. 165, n. 2-3, p. 385–396, set. 1992. Disponível em: <https://doi.org/10.1016/0301-0104(92)87053-c>. Citado 3 vezes nas páginas 63, 64, and 65.

SHERAR, M. D. et al. Interstitial microwave thermal therapy for prostate cancer: Method of treatment and results of a phase i/ii trial. **Journal of Urology**, Ovid Technologies (Wolters Kluwer Health), v. 166, n. 5, p. 1707–1714, nov. 2001. Disponível em: <https://doi.org/10.1016/s0022-5347(05)65658-3>. Citado na página 46.

SHERRY, L. et al. Localized surface plasmon resonance spectroscopy of single silver nanocubes. **Nano Letters**, v. 5, p. 2034–8, 11 2005. Citado na página 36.

SöNNICHSEN, C. et al. Drastic reduction of plasmon damping in gold nanorods. **Physical Review Letters**, American Physical Society (APS), v. 88, n. 7, jan. 2002. Disponível em: <https://doi.org/10.1103/physrevlett.88.077402>. Citado na página 28.

STEWART, J. W. et al. Ultrafast pyroelectric photodetection with on-chip spectral filters. **Nature Materials**, Springer Science and Business Media LLC, nov. 2019. Disponível em: <https://doi.org/10.1038/s41563-019-0538-6>. Citado na página 36.

STONE, J.; JACKSON, S.; WRIGHT, D. Biological applications of gold nanorods. **Wiley Interdisciplinary Reviews: Nanomedicine and Nanobiotechnology**, Wiley, v. 3, n. 1, p. 100–109, out. 2010. Disponível em: <https://doi.org/10.1002/wnan.120>. Citado na página 37.

SUZAKI, Y.; TACHIBANA, A. Measurement of the μm sized radius of gaussian laser beam using the scanning knife-edge. **Applied Optics**, The Optical Society, v. 14, n. 12, p. 2809, dez. 1975. Disponível em: <https://doi.org/10.1364/ao.14.002809>. Citado na página 69.

SYDNEY AUSTRALIA, U. S. o. P. **Mirages and the green flash**. 2009. <https://www.animations.physics.unsw.edu.au/jw/light/mirages-green-flash-sky-colours.htm>. [Online; accessed 09-January-2020]. Citado na página 59.

TAKEMURA, K. et al. A localized surface plasmon resonance-amplified immunofluorescence biosensor for ultrasensitive and rapid detection of nonstructural protein 1 of zika virus. **PLOS ONE**, Public Library of Science (PLoS), v. 14, n. 1, p. e0211517, jan. 2019. Disponível em: <https://doi.org/10.1371/journal.pone.0211517>. Citado na página 23.

TAYLOR, A. B.; SIDDIQUEE, A. M.; CHON, J. W. M. Below melting point photothermal reshaping of single gold nanorods driven by surface diffusion. **ACS Nano**, American Chemical Society (ACS), v. 8, n. 12, p. 12071–12079, nov. 2014. Disponível em: <https://doi.org/10.1021/nn5055283>. Citado na página 23.

THAKORE, V. et al. Thermoplasmonic response of semiconductor nanoparticles: A comparison with metals. **Advanced Theory and Simulations**, Wiley, v. 2, n. 1, p. 1800100, out. 2018. Disponível em: <https://doi.org/10.1002/adts.201800100>. Citado na página 35.

TRAN, K. T. M.; NGUYEN, T. D. Lithography-based methods to manufacture biomaterials at small scales. **Journal of Science: Advanced Materials and Devices**, Elsevier BV, v. 2, n. 1, p. 1–14, mar. 2017. Disponível em: <https://doi.org/10.1016/j.jsamd.2016.12.001>. Citado na página 36.

USUKURA, E. et al. LSPR-mediated high axial-resolution fluorescence imaging on a silver nanoparticle sheet. **PLOS ONE**, Public Library of Science (PLoS), v. 12, n. 12, p. e0189708, dez. 2017. Disponível em: <https://doi.org/10.1371/journal.pone.0189708>. Citado na página 22.

VERRE, R. et al. Transition metal dichalcogenide nanodisks as high-index dielectric mie nanoresonators. **Nature Nanotechnology**, Springer Science and Business Media LLC, v. 14, n. 7, p. 679–683, maio 2019. Disponível em: <https://doi.org/10.1038/s41565-019-0442-x>. Citado na página 36.

WALSH, J. T. et al. Pulsed laser tissue interaction. In: **Optical-Thermal Response of Laser-Irradiated Tissue**. Springer Netherlands, 2010. p. 617–649. Disponível em: <https://doi.org/10.1007/978-90-481-8831-4_15>. Citado na página 49.

WANG, Y. et al. Comparison study of gold nanohexapods, nanorods, and nanocages for photothermal cancer treatment. **ACS Nano**, American Chemical Society (ACS), v. 7, n. 3, p. 2068–2077, fev. 2013. Disponível em: <https://doi.org/10.1021/nn304332s>. Citado na página 48.

WANG, Y.; DELLAGO, C. Structural and morphological transitions in gold nanorods: a computer simulation study. **The Journal of Physical Chemistry B**, American Chemical Society (ACS), v. 107, n. 35, p. 9214–9219, set. 2003. Disponível em: <https://doi.org/10.1021/jp034445w>. Citado na página 23.

WANG, Y.; TEITEL, S.; DELLAGO, C. Surface-driven bulk reorganization of gold nanorods. **Nano Letters**, American Chemical Society (ACS), v. 5, n. 11, p. 2174–2178, nov. 2005. Disponível em: <https://doi.org/10.1021/nl051149h>. Citado na página 23.

WHINNERY, J. R. Laser measurement of optical absorption in liquids. **Accounts of Chemical Research**, American Chemical Society (ACS), v. 7, n. 7, p. 225–231, jul. 1974. Disponível em: <https://doi.org/10.1021/ar50079a003>. Citado na página 59.

WONG, J. K. et al. Temperature measurements of a gold nanosphere solution in response to light-induced hyperthermia. In: **Volume 8A: Heat Transfer and Thermal Engineering**. American Society of Mechanical Engineers, 2013. Disponível em: <https://doi.org/10.1115/imece2013-66424>. Citado na página 55.

XU, X. et al. Discrete dipole approximation simulation of the surface plasmon resonance of core/shell nanostructure and the study of resonance cavity effect. **The Journal of Physical Chemistry C**, American Chemical Society (ACS), v. 116, n. 45, p. 24046–24053, nov. 2012. Disponível em: <https://doi.org/10.1021/jp306238x>. Citado na página 39.

YAKUNIN, A. N.; AVETISYAN, Y. A.; TUCHIN, V. V. Quantification of laser local hyperthermia induced by gold plasmonic nanoparticles. **Journal of Biomedical Optics**, SPIE-Intl Soc Optical Eng, v. 20, n. 5, p. 051030, jan. 2015. Disponível em: <https://doi.org/10.1117/1.jbo.20.5.051030>. Citado 2 vezes nas páginas 48 and 49.

YIN, Z. et al. Cu_3N nanocubes for selective electrochemical reduction of CO_2 to ethylene. **Nano Letters**, American Chemical Society (ACS), v. 19, n. 12, p. 8658–8663, nov. 2019. Disponível em: <https://doi.org/10.1021/acs.nanolett.9b03324>. Citado na página 36.

ZHANG, D. et al. Localized surface plasmon resonance enhanced singlet oxygen generation and light absorption based on black phosphorus@AuNPs nanosheet for tumor photodynamic/thermal therapy. **Particle & Particle Systems Characterization**, Wiley, v. 35, n. 4, p. 1800010, mar. 2018. Disponível em: <https://doi.org/10.1002/ppsc.201800010>. Citado na página 22.

ZHANG, Y. et al. Metal-enhanced singlet oxygen generation: A consequence of plasmon enhanced triplet yields. **Journal of Fluorescence**, Springer Science and Business Media LLC, v. 17, n. 4, p. 345–349, maio 2007. Disponível em: <https://doi.org/10.1007/s10895-007-0196-y>. Citado na página 22.

ZHANG, Y. et al. Temperature-dependent cell death patterns induced by functionalized gold nanoparticle photothermal therapy in melanoma cells. **Scientific Reports**, Springer Science and Business Media LLC, v. 8, n. 1, jun. 2018. Disponível em: <https://doi.org/10.1038/s41598-018-26978-1>. Citado na página 26.

ZHAO, J. et al. Ag nanoframes: controllable reduction of AgClxBr1-x nanocubes. **Chemical Communications**, Royal Society of Chemistry (RSC), v. 55, n. 39, p. 5571–5574, 2019. Disponível em: <https://doi.org/10.1039/c9cc02240f>. Citado na página 36.

ZHAO, Y. et al. Plasmonic-enhanced Raman scattering of graphene on growth substrates and its application in SERS. **Nanoscale**, Royal Society of Chemistry (RSC), v. 6, n. 22, p. 13754–13760, set. 2014. Disponível em: <https://doi.org/10.1039/c4nr04225e>. Citado na página 22.

ZHOU, N. et al. Plasmon-enhanced light harvesting: applications in enhanced photocatalysis, photodynamic therapy and photovoltaics. **RSC Advances**, Royal Society of Chemistry (RSC), v. 5, n. 37, p. 29076–29097, 2015. Disponível em: <https://doi.org/10.1039/c5ra01819f>. Citado na página 22.

ZHU, X. et al. Cellular uptake behaviour, photothermal therapy performance, and cytotoxicity of gold nanorods with various coatings. **Nanoscale**, Royal Society of Chemistry (RSC), v. 6, n. 19, p. 11462–11472, ago. 2014. Disponível em: <https://doi.org/10.1039/c4nr03865g>. Citado na página 48.

ZHUO, X. et al. Colour routing with single silver nanorods. **Light: Science & Applications**, Springer Science and Business Media LLC, v. 8, n. 1, abr. 2019. Disponível em: <https://doi.org/10.1038/s41377-019-0150-1>. Citado na página 36.

ZONG, C. et al. Plasmon-enhanced stimulated Raman scattering microscopy with single-molecule detection sensitivity. **Nature Communications**, Springer Science and Business Media LLC, v. 10, n. 1, nov. 2019. Disponível em: <https://doi.org/10.1038/s41467-019-13230-1>. Citado na página 22.

ZORIĆ, I. et al. Gold, platinum, and aluminum nanodisk plasmons: Material independence, subradiance, and damping mechanisms. **ACS Nano**, American Chemical Society (ACS), v. 5, n. 4, p. 2535–2546, mar. 2011. Disponível em: <https://doi.org/10.1021/nn102166t>. Citado na página 36.

ZULOAGA, J.; PRODAN, E.; NORDLANDER, P. Quantum plasmonics: Optical properties and tunability of metallic nanorods. **ACS Nano**, American Chemical Society (ACS), v. 4, n. 9, p. 5269–5276, ago. 2010. Disponível em: <https://doi.org/10.1021/nn101589n>. Citado na página 37.

APPENDIX A – MATLAB SCRIPTS

In this section, the *Matlab* scripts employed throughout the progress of this research are presented.

SIZE DEPENDENT DRUDE MODEL FOR METALLIC NANOPARTICLES

```
% Script criado por Túlio Pedrosa (Laboratório de Óptica Biomédica e Imagem
% - DES/CTG UFPE) - Setembro de 2019

% Este script corrige a Teoria de Drude para Metais para nanobastões de
% ouro com comprimentos variando de 5 nm a 200 nm (limite superior
% arbitrário). A permissividade bulk é obitida a partir dos índices de
% refração do ouro medidos por Johnson e Christy

clear
clc

format long

% Inicialização de parâmetros

N    = 5.90e28;                 % Densidade de elétrons livres
e    = 1.6e-19;                 % Carga fundamental
eps0 = 8.854e-12;               % Permissividade do vácuo
me   = 9.11e-31;                % Massa do elétron

wp = sqrt((N*e^2)/(eps0*me));   % Frequência de plasma

y0  = 1.07e14;                  % Amortecimento

vf   = 1.40e6;                  % Velocidade de Fermi
A    = 0.25;                    % Parâmetro fenomenológico de espalhamento
                                % (este é um parâmetro associado as
                                % contribuições e-e, e-lattice e e-surface
                                % e e-ph. Seu valor muda para diferentes
                                % formatos e para diferentes materiais)

L = 100e-9;                     % Comprimento do bastão
D = 10e-9;                      % Diâmetro do bastão
AR = L/D;                       % Razão de aspecto do bastão

import1 = csvread('n_(Johnson_Au).csv',1);  % Importa a parte real do
                                            % índice de refração do ouro
import2 = csvread('k_(Johnson_Au).csv',1);  % Importa a parte imaginária do
```

```
                                        % índice de refração do ouro
                                        % https://refractiveindex.info/

wl = import1(:,1);                      % Importando os comprimentos de
                                        % onda (um)
wlexport = (1e9).*wl;                   % Forma de "exportação" do
                                        % comprimento de onda (nm)

n = import1(:,2);                       % Índice de refração (Re)
k = import2(:,2);                       % Índice de refração (im)

eb_r = n.^2 - k.^2;                     % Permissividade (Re)
eb_i = 2*(n.*k);                        % Permissividade (Im)

eb = eb_r + i*eb_i;                     % Permissividade complexa

w  = (2*pi*(3e8))./wl;                  % Frequência angular

drude = (wp^2)./(w.*(w+i*y0));

V = (pi/4)*(D.^3).*(AR - 1/3);          % Volume do nanobastão
S = pi*(D.^2).*AR;                      % Área do nanobastão

Leff = 4*V./S;                          % Livre caminho médio efetivo
yeff = y0 + A*vf./Leff;                 % Correção do amortecimento

drude_correction = (wp^2)./(w.*(w+i*yeff));

e = eb + drude - drude_correction;      % Permissividade corrigida

er = real(e);                           % Parte real corrigida
ei = imag(e);                           % Parte imaginária corrigida

figure(1)
plot(wlexport,er);                      % Plota a parte real da
                                        % permissividade corrigida
figure(2)
plot(wlexport,ei);                      % Plota a parte imaginária da
                                        % permissividade corrigida

output_r = [wlexport(:),er(:,k)];       % Concatenação
output_i = [wlexport(:),ei(:,k)];       % Concatenação

nome_real = strcat('Permissividade_Corrigida_Re.xlsx');
nome_imag = strcat('Permissividade_Corrigida_Im.xlsx');

writematrix(output_r,nome_real);        % Exporta em .xlsx
```

```
writematrix(output_i,nome_imag);            % Exporta em .xlsx
```

MIE-GANS THEORY FOR PROLATE SPHEROIDS

```
% Script criado por Túlio Pedrosa (Laboratório de Óptica Biomédica e Imagem
% - DES/CTG UFPE) - Setembro de 2019

% Este script calcula as propriedades ópticas e térmicas de nanobastões
% por meio da teoria de Mie-Gans para esferoides prolatos. Este script
% a correção de Drude para Metais para nanobastões de ouro descrita no
% script anterior. A permissividade bulk é obitida a partir dos índices de
% refração do ouro medidos por Johnson e Christy, e pode ser obtida em
% https://refractiveindex.info/

clear
clc

format long

% PARÂMETROS DO NANOBASTÃO

L = 75e-9;       % Comprimento do nanobastão
AR = 6.7;        % Razão de aspecto do nanobastão
D = L/AR;        % Diâmetro do nanobastão


% CORREÇÃO DE DRUDE PARA O TAMANHO (AuNRs)

M = csvread('Au_Bulk.csv',1);

wl = M(:,1);
wl2 = (1e-6).*wl;

n = M(:,2);
k = M(:,3);

N    = 5.90e28;
e    = 1.6e-19;
eps0 = 8.854e-12;
me   = 9.11e-31;
lambda_ref = 1240e-9;

wp = sqrt((N*e^2)/(eps0*me));

y0  = 1.07e14;
y0      = y0*ones(1,length(L));

vf   = 1.40e6;
```

```
A    = 0.25;
epsm = 1.33^2;

eb_r = n.^2 - k.^2;
eb_i = 2*(n.*k);

eb = eb_r + i*eb_i;

w  = (2*pi*(3e8))./wl2;

drude = (wp^2)./(w.*(w+i.*y0));

V = ((pi/4)*(D.^3)).*(AR - 1/3);
S = (pi*(D.^2)).*AR;

Leff = 4*V./S;
yeff = y0 + A*vf./Leff;

drude_correction = (wp^2)./(w.*(w+i.*yeff));

e = eb + drude - drude_correction;

er = real(e);
ei = imag(e);

wl_array = 200e-9:1e-10:2000e-9;

interp_r = zeros(length(wl_array),1);
interp_i = zeros(length(wl_array),1);

interp_r(:) = spline(wl2,er(:),wl_array);
interp_i(:) = spline(wl2,ei(:),wl_array);

% MODELO DE GANS PARA NANOBASTÕES

depolarization_a = (1./(AR.^2 - 1)).*((AR./(2.*sqrt(AR.^2 - 1))).*log((AR+
    sqrt(AR.^2 - 1))./(AR-sqrt(AR.^2 - 1))) - 1);
depolarization_a = real(depolarization_a);
depolarization_b = (1 - depolarization_a)/2;
depolarization_c = (1 - depolarization_a)/2;

e1 = interp_r;
e2 = interp_i;

factor_abs_a = (e2./((depolarization_a).^2))./((e1 + (1 - depolarization_a)
    *epsm./depolarization_a).^2 + e2.^2);
```

```
factor_abs_b = (e2./((depolarization_b).^2))./((e1 + (1 - depolarization_b)
    *epsm./depolarization_b).^2 + e2.^2);
factor_abs_c = (e2./((depolarization_c).^2))./((e1 + (1 - depolarization_c)
    *epsm./depolarization_c).^2 + e2.^2);

factor_sca_a = ((e1 - epsm).^2 + ((e2.^2)/((depolarization_a).^2))).//((e1 +
     ((1 - depolarization_a)./depolarization_a)*epsm).^2 + e2.^2);
factor_sca_b = ((e1 - epsm).^2 + ((e2.^2)/((depolarization_b).^2))).//((e1 +
     (1 - depolarization_b).*epsm/depolarization_b).^2 + e2.^2);
factor_sca_c = ((e1 - epsm).^2 + ((e2.^2)/((depolarization_c).^2))).//((e1 +
     (1 - depolarization_c).*epsm/depolarization_c).^2 + e2.^2);

sum_abs = factor_abs_a+factor_abs_b+factor_abs_c;
sum_sca = factor_sca_a+factor_sca_b+factor_sca_c;

wl_trans = wl_array.';

sigma_abs = ((2*pi)*(epsm^(3/2)).*sum_abs.*V)./(3*wl_trans);
sigma_sca = ((8*pi^3)./(9*wl_trans.^4))*(epsm^2)*(V.^2).*sum_sca;
sigma_ext = sigma_sca + sigma_abs;

J0 = (lambda_ref/(2*pi)).*(sigma_abs./V);

beta = 1 + 0.096587*(log(AR))^2;
Req = ((3*V/(4*pi))^(1/3));
S2F = sigma_abs/(beta*Req);

wlexport = (1e9).*wl_array;


% RESULTADOS

output_absorption = [wlexport(:),sigma_abs];
output_scattering = [wlexport(:),sigma_sca];
output_extinction = [wlexport(:),sigma_ext];
output_Joulenumber = [wlexport(:),J0];
output_SteadyStateFactor = [wlexport(:),S2F];

writematrix(output_absorption,'NR_AbsorptionCS.xlsx');
writematrix(output_scattering,'NR_AbsorptionCS.xlsx');
writematrix(output_extinction,'NR_AbsorptionCS.xlsx');
writematrix(output_Joulenumber,'NR_AbsorptionCS.xlsx');
writematrix(output_SteadyStateFactor,'NR_AbsorptionCS.xlsx');
```

DATA PROCESSING FOR THERMAL LENS MEASUREMENTS

```
% Script criado por Túlio Pedrosa (Laboratório de Óptica Biomédica e Imagem
% - DES/CTG UFPE) - Janeiro de 2020
```

```
% Este script processa os arquivos (.csv) dos experimentos de lente térmica
% de duplo feixe mode-mismatched obtidos em osciloscópio

clear
clc

% ---------------------------- Initialization -----------------------------

import1 = csvread('ARQUIVO.csv',1,3);

x_axis = import1(:,1);
y_axis = import1(:,2);


% --------------------------- Z-Scan parameters ---------------------------

z_op    = 27.5e-3;          % Comprimento Rayleigh to feixe de sonda
z_2     = 1;                % Distância óptica entre amostra e fotodetector
                            % (em metros - feixe sonda)
w_probe = 74.4e-6;          % Cintura do feixe sonda (633 nm)
w_pump  = 20.3e-6;          % Cintura do feixe de excitação (532 nm)

dndT = -0.8e-4;             % Coeficiente termo-óptico da água
L = 2e-3;                   % Espessura da cubeta
lambda_probe = 633e-9;      % Comprimento de onda de sonda

z_foco = 17.09;             % Posição focal da amostra (mm)
z_effect = 15.33;           % Posição de máximo efeito térmico (mm)

z = abs(z_foco - z_effect)*(1e-3);          % Posição Z-scan
m = (w_probe/w_pump)^2;                     % Fator de mode-mismatch
V = z/z_op + (z_op/z_2)*(1 + (z/z_op)^2);

num = 2*m*V;
den_a = ((1+2*m)^2 + V^2)/2;
den_b = 1 + 2*m + V^2;

% ---------------------------------------------------------------------------
%         Detecção dos períodos de absorção e relaxação térmica

y_smooth = y_axis;

for index = 1:256

    y_smooth = smooth(y_smooth);
```

```
end

diff = y_axis - y_smooth;

fs = 1000;
[sdiff,d3] = lowpass(diff,20,fs,'ImpulseResponse','iir','Steepness',0.95);

sdiff = smooth(sdiff);
max_diff = max(sdiff);

sdiff = sdiff/max_diff;
sdiff = abs(sdiff);

[val,pos] = findpeaks(sdiff,'MinPeakProminence',1-1/exp(1));

period_fall = x_axis(pos(2)) - x_axis(pos(1));
period_rise = x_axis(pos(3)) - x_axis(pos(2));

time_fall = zeros(pos(2)-pos(1),1);
val_fall = zeros(pos(2)-pos(1),1);

time_rise = zeros(pos(3)-pos(2),1);

for index = pos(1):pos(2)
    time_fall(index - pos(1) + 1) = x_axis(index);
    val_fall(index - pos(1) + 1) = y_axis(index);
end

for index = pos(2):pos(3)
    time_rise(index - pos(2) + 1) = x_axis(index);
end

time_fall_norm = time_fall - min(time_fall);
time_rise_norm = time_rise - min(time_rise);

% Interpolação do sinal DTL para obtenção dos coeficientes \theta e t_c

I0_fall = max(val_fall);

fun = @(coeff,time_fall_norm) I0_fall*(1 - (coeff(1)./2).*atan(num./(den_a
    *(coeff(2)./time_fall_norm) + den_b))).^2;

initial_values = [0.5,1e-4];
[coeff,resTDL,jacTDL,covTDL,errvarTDL,errmodTDL] = nlinfit(time_fall_norm,
    val_fall,fun,initial_values);

theta = coeff(1);
```

```
tc = coeff(2);

timesDTL = linspace(time_fall_norm(1),time_fall_norm(end));
figure(2)
hold on
plot(time_fall_norm,val_fall,'ko');
plot(timesDTL,fun(coeff,timesDTL),'-','linewidth',2,'color','#77AC30');
hold off
xlabel('t (s)','FontSize',12,'FontWeight','bold');
ylabel('Thermal lens Intensity (arb. units)','FontSize',12,'FontWeight','
    bold');
box on
set(gca,'FontSize',12,'FontWeight','bold','linewidth',1.1);
lgd = legend('Experimental','Best fit');
legend boxoff

% Transformação do efeito de lente em variação de temperatura

window_max = 100e-3;                        % Janela de excitação do chopper
time_window = linspace(0,window_max,100);
syms k;
f_max = (((-2)^k)/(k*factorial(k+1))).*(1-(1./(1+2.*window_max./tc)).^k);
sum_max = symsum(f_max,k,1,100);
sum_max = double(sum_max);

deltaT_max = -((theta*lambda_probe)/(4*pi*L*dndT))*(log(1+2*window_max/tc)
    + sum_max)

deltaT_curve = deltaT_max*(-y_axis - min(-y_smooth))/max(-y_smooth - min(-
    y_smooth));

figure(3)
plot(x_axis,deltaT_curve,'-','linewidth',2,'color','#A2142F');
xlabel('t (s)','FontSize',12,'FontWeight','bold');
ylabel('\DeltaT_{bulk} (\^oC)','FontSize',12,'FontWeight','bold');
box on
set(gca,'FontSize',12,'FontWeight','bold','linewidth',1.1);

for index = pos(2):pos(3)
    thermal_decay(index - pos(2) + 1) = deltaT_curve(index);
end

% Obtenção do parâmetro associado a perda de calor (B)

thermal_decay = thermal_decay.';

loss = @(B,time_rise_norm) deltaT_max*exp(-B*time_rise_norm);
```

```
B0 = 60;
[B,resLoss,jacLoss,covLoss,errvarLoss,errmodLoss] = nlinfit(time_rise_norm,
   thermal_decay,loss,B0);

timesLoss = linspace(time_rise_norm(1),time_rise_norm(end));
figure(4)
hold on
plot(time_rise_norm,thermal_decay,'ko');
plot(timesLoss,loss(B,timesLoss),'-','linewidth',2,'color','#D95319');
hold off
xlabel('t (s)','FontSize',12,'FontWeight','bold');
ylabel('\DeltaT_{bulk} (\^oC)','FontSize',12,'FontWeight','bold');
box on
set(gca,'FontSize',12,'FontWeight','bold','linewidth',1.1);
lgd = legend('Experimental decay','Best fit of B');
legend boxoff

% Resultados

[theta,tc,deltaT_max,B]
```

APPENDIX B – FINITE ELEMENT METHOD SIMULATIONS

OVERVIEW OF FINITE ELEMENT METHOD (FEM)

The Finite Element Method (FEM) is a numeric computational procedure with the purpose of solving multiphysics systems described by differential equations under the influence of specific boundary value problems. The employment of the FEM allows the analysis of physical phenomena with high accuracy, yielding results in good agreement with experimental data when compared to other numeric and analytical methods. Therefore, the assessment of a good part of physical phenomena in research and the design of systems in engineering is performed by FEM calculations.

The applicability of the FEM method supposes the problem to be to be subjected to an integral law or differential equation, enabling such equations to be replaced in all domains by a finite summation of discretized sub-domains that remain under the same physical regime. Each sub-domain features a simple geometry in which the problem preserves continuity and differentiability. The sub-domains are integrated and the individual results are added together. Equation B.1 describes the reconstitution of a discretized problem, while equation B.2 shows the discretization of a domain *V* into sub-domains V_i.

$$\int_V f dV = \sum_{i=1}^{n} \int_{Vi} f dV \tag{B.1}$$

in which

$$V = \sum_{i=1}^{n} V_i \tag{B.2}$$

Suppose that a function f is a variable of a differential function. One can approximate f as a function f_i that is the linear combination of a base of building orthogonal functions $\{\lambda_1, \lambda_2, \cdots, \lambda_n\}$:

$$f \approx f_i \tag{B.3}$$

$$f_i = \sum_{n} f_n \lambda_n \tag{B.4}$$

Here, f_n characterizes as the coefficients of the basic building functions. The geometry is then discretized in smaller elements called *Mesh cells*, allowing the solution of complex problems with less computational effort due to fragmentation of the problem. In such fragments, the number of physical variables associated to the problem (that are infinitely many real variables) are replaced by a limited number of well behaved variables. The accuracy of the FEM is related to the type of elements associated to the model. For instance, hexahedral mesh is preferable to solve bi-dimensional problems, while the tetrehedral one performs better in three-dimensions. The figure 39 shows a spherical region partitioned in many sub-domains to endure FEM computation. An increase in mesh number can lead to a refinement in accuracy, but processing times also increase. Besides that, not always an increase in mesh number will lead to an increase in accuracy. The steps associated to any FEM analysis are listed below:

1. Discretization of the region to be analyzed in a finite number of sub-domains (meshing);
2. Derivation of equations that govern the behavior of each sub-domain;
3. Grouping of all elements in the region undergoing analysis and conjugation of individual results;
4. Solving set of the linear system of equations.

Figure 39 – Sub-domains in a model undergoing FEM analysis. The region is said to be meshed..

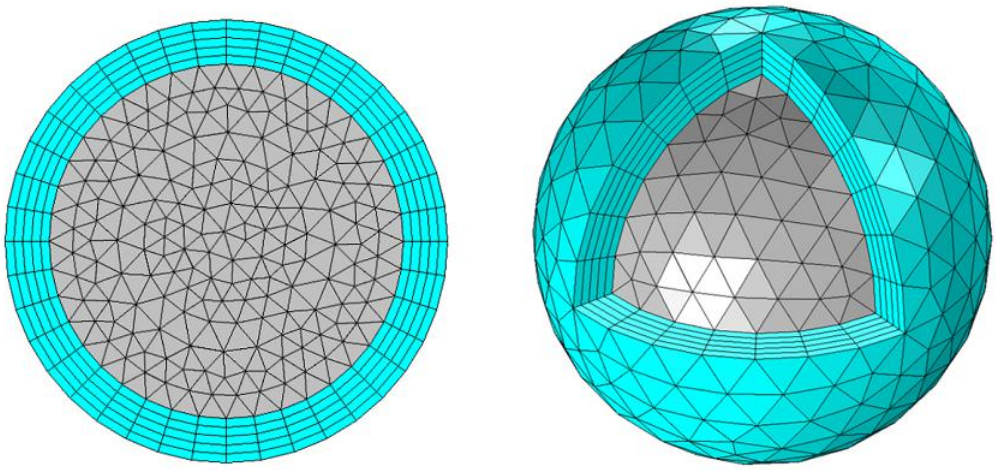

Source: adapted from (COMSOL, 2016).

In problems where EM fields are involved, the FEM approximation is implemented in Maxwell Equations for electrodynamics. In order to be resolvable, a set of boundary conditions and material constitutive relations are necessary. The COMSOL formulation of Maxwell equations are the same to both the Radio-Frequency - *Frequency Domain* module and the Waveoptics

- *Wavelength Domain* module, and presents a classical analysis at macroscopic level based on the solution of the non-homogeneous wave equation

$$\vec{\nabla} \times \left[\mu_r^{-1}\left(\vec{\nabla} \times \vec{E}\right)\right] - \omega^2 \epsilon_0 \mu_0 \left(\epsilon_r - j\frac{\sigma}{\omega \epsilon_0}\right)\vec{E} = 0 \tag{B.5}$$

in which μ_0 and ϵ_0 are respectively the vacuum magnetic permeability and electric permittivity, and μ_r and ϵ_r designate respectively the relative permeability and relative permittivity of material media associated to the problem.

Similarly, in problems where transient conductive heat transfer are involved, the Laplace equation is implemented by FEM method. The COMSOL formulation to a generic heat-transfer problem is given by equation B.6, where $\vec{u}$ is the fluid velocity and *Q* is the volumetric power density.

$$\rho C_p \frac{\partial T}{\partial t} + \rho C_p \, \vec{u} \cdot \nabla T + \nabla \cdot (-\kappa \nabla T) = Q \tag{B.6}$$

SIMULATION OF METALLIC NANOSTRUCTURES IN COMSOL MULTIPHYSICS

This tutorial describes the procedures performed to simulate gold nanoparticles using the Electromagnetic Waves model of COMSOL. Here, at the end of the simulation, the optical cross sections of scattering, absorption and extinction of a nanoparticle are going to be obtained, as well as the Joule number and the Steady-state factor of a single nanorod. Furthermore, this tutorial can be employed as a basic framework to the simulation of nanoparticles of any other material or morphology of interest.

After opening COMSOL, you will come across the New project window. In the window *New*, click in Model Wizard, and after that, select *3D* in the space dimension menu. It's necessary now to select the physical module that will be employed to analyze the problem. In *Select Physics*, expand the drop-down bar *Radio Frequency*, and select the *Frequency Domain (emw)* option and Click in *Add*. With such physics interface selected, click in *Study* and in the *Select Study* screen click in *Frequency Domain* and after that, click in *Done*. A new screen with many elements will show, as can be seen in figure 40. Take the opportunity to save the project in at a desired location with a desired name.

In figure 40, the main screen is divided in four parts. Section 1 is the *Toolbar*, and has among its functions the role of adding new and diverse elements to the project. Section 2 (*Model Builder*) is the menu that allows the user to navigate throughout the project. Here, it is also possible to perform some of the *Toolbar* functionalities. Section 3 (*Settings*) has all alterable properties (parameters) a selected object. The section 4 (*Graphics*) exhibits the system geometry and resulting curves obtained in the simulation. It is possible to rotate the geometry by holding

Figure 40 – Screen after the project setup. This is the main project screen of COMSOL.

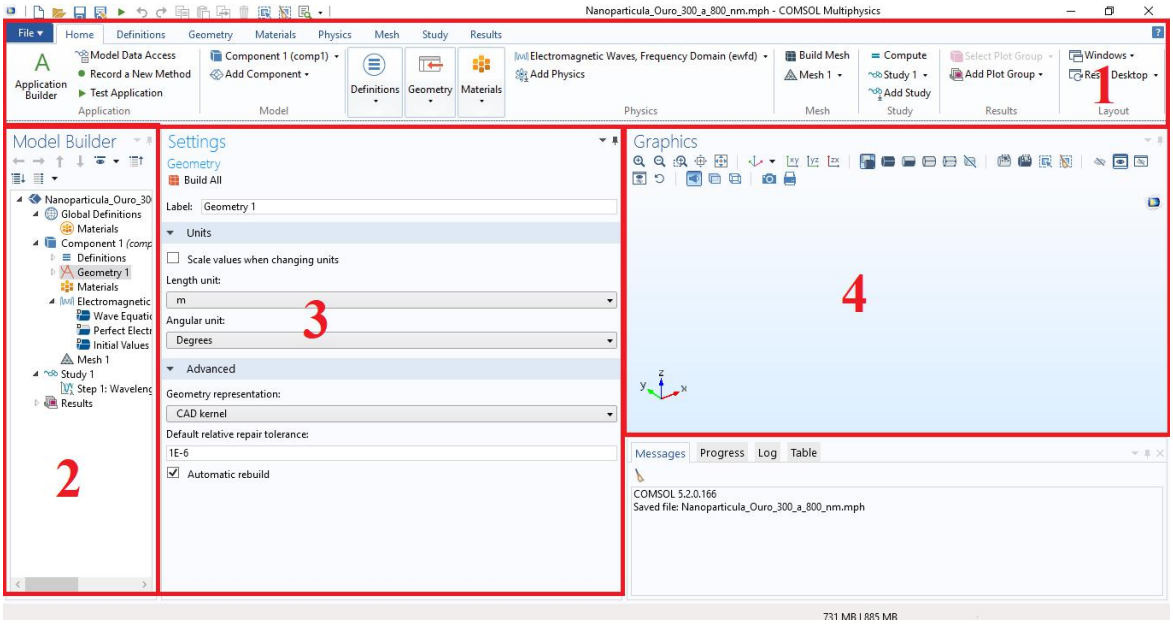

Source: belongs to the author.

the left click button and moving the mouse. Translation can be accomplished by holding the right button of the mouse and dragging the cursor. In possession of such information, let's begin the construction of our project by defining some global parameters associated to the problem. To do so, click in *Home* (toolbar), after that click in *Definitions*. Then, select *Parameters*. Notice now that the *Setting* session has changed, and now it contains a table to be filled by global parameters. Fill this table accordingly to table 3.

Table 3 – Global simulation parameters in COMSOL.

Name	Expression	Value	Description
length	L-D	-	-
D	L/AR	-	Nanorod diameter
radius	D/2	-	Nanorod radius
L	45	-	Nanorod length
AR	4.0	-	Nanorod aspect ratio
r_pml	3500	-	PML radius
lambda_ref	1240[nm]	-	-
lambda	1064	-	Wavelength
t_pml	1000	-	PML thickness
E_0	1[V/m]	-	Incident electric field
n_water	1.33	-	Water refractive index
Vol	(pi*((D[nm]) ^ 3)/2)*(AR/2 - 1/6)	-	Nanorod volume
S_{in}	((n_water*(E0 ^ 2))/(2*Z0_const))	-	Poynting vector of incident EM wave
beta	1 + 0.096587*(ln(AR)^2)	-	S2F shape factor
Req	(3*Vol/(4*pi))^(1/3)	-	Equivalent radius

Source: belongs to the author.

With table filled, click in *Geometry 1* (model builder) and in the *Length unit* drop down bar replace from *m* to *nm*. Right click *Geometry 1* and select a sphere. At the sphere *Settings* section, fill the field *Radius* and *z* with the parameters *radius* and *length/2* respectively. In the superior part of the settings menu, click *Build All Objects*. Repeat the step to add a second sphere. Fill the field *Radius* and *z* with the parameters *radius* and *-length/2* respectively. Now, add a cylinder. Fill the field *Radius* and *z* with the parameters *radius* and *-length/2* respectively. The field *Height* must be filled with *length*. Click in *Build All Objects*. After that, in the *Graphics* section, click in *Go to Default View*. You should now be able to see a nanorod. It is now necessary to connect the geometries into a single entity. To do so, left click *Geometry 1* in the model builder, go to *Booleans and partitions* and click in *Union*. In the *Graphics* screen, select the three geometries placed, and unckeck the field *Keep interior boundaries*. Click in *Build All Objects*. The nanorod now must be a single entity.

Add another sphere to the problem, and fill the *Radius* field with *r_pml*. In the bottom of the page, yet in the *Settings* menu, expand the *Layers* field and add a new layer of thickness *t_pml*. In *Graphics*, click in *Go to Default View*. With the full view of the outside sphere that limits the nanorod domain, it is now necessary to define the domains and boundaries of the problem. Click in *Definitions* (toolbar) and then click in *Explicit*. In *Geometry*, enable the option *Click and Hide*, and hide the spherical shell as a whole (click in the pieces to hide them). Disable the option *Click and Hide* and select the remaining surface. Enable the option *Click and Hide* once again, hide the surface (exposing the nanorod), disable the option *Click and Hide* and select the nanoparticle. In the settings panel you must be able to notice the domains 5 and 6 selected. Rename the label *Explicit 1* to *Physical Domains*. In *Graphics*, click in *Reset Hiding*.

In *Definitions* (toolbar), click in *Complement* and rename its label to *PML Domains*. Yet in the settings, look for the field *Input Entities* and click in *Add* in *Selections to invert*. A pop-up will appear. Select *Physical Domains* and click in *OK*. Add now a new *Explicit* and rename it as *Nanoparticle*. Hide once again the external sphere and the surface, and select the nanorod. Add another explicit, click in *Zoom Extents* (graphics) and in the parameter *Geometric Entity Level* (settings), replace *Domain* with *Boundary*. Select all the pieces of the nanoparticle surface and then rename the explicit to *Nanoparticle surface*. Add a fourth Explicit, click in *Reset Hiding*, *Zoom Extents* and change the *Geometric Entity Level* from *Domain* to *Boundary*. Select all parts of the external surface and rename the explicit as *External PML Surface*. Add a fifth and a last *Explicit*, change the option *Domain* with *Boundary* and rename it to *Internal PML Surface*. Hide the spherical shell and select only the remaining surface.

To define the PML, click in *Definitions* (toolbar) and click in *Perfectly Matched Layer*. In *Domain Selection* (settings) change *Manual* with *PML Domains*. In the bottom part of the menu, change the option *Geometry* from *Cartesian* to *Spherical*. Look for the field *PML Scaling factor* and define it as 0.5. Now, we proceed to add the materials of the problem. Using the scripts provided in the previous appendix, create the real and imaginary permittivity tables of

gold nanorods for the desired dimensions. With the files in hand, go to *Definitions*, and select *Interpolations*. Click in *Load from File*, browser to the real permittivity file and select it. In *Interpolation and Extrapolation* bars, change *Interpolation* from *Linear* to *Cubic Spline*. In the field *Function name*, write *eps_real*. Repeat this process to the imaginary permittivity, and write the field *Function name* as *eps_img*.

In the *Model builder* toolbar, right click *Materials*. Select *Blank material*. In the *Geometric Entity Section* change the drop down bar *Selection* from *Manual* to *Nanoparticle*. In *Material Contents*, fill the Relative permittivity value with *eps_real(lambda)-i*eps_img(lambda)*. The Relative permeability and electrical conductivity must be filled with 1 and 0 respectively. Add a new *Blank material*. In *Selection*, replace *Manual* with *All domains*. Click in domains *6* (nanoparticle) and click to *Remove from Selection*. Fill the permittivity, permeability and conductivity fields with *n_waterˆ2*, *1* and *0* respectively. Now, we have to define the incident electromagnetic wave that will interact with the nanorod. To do so, in *Model Builder* click in *Electromagnetic Waves, Frequency Domain*. In *Settings*, replace the option *Solver* from *Full field* with *Scattered field*. Bellow, in *Background electric field*, fill the *z* component with *E0*exp(-j*2*n_water*pi/(lambda[nm])*x)*, while keeping the *x* and *y* components null. Right click *Electromagnetic Waves, Frequency Domain* and select *Scattering Boundary Condition*. In *Boundary selection* replace *manual* with *Internal PML Surface*.

It is necessary to fragment the structure into many finite elements in order to proceed with electrodynamics calculations. To do so, in *Model Builder*, right click in *Mesh*, expand the *More Operations* option and select *Free triangular*. In *Boundary selection* change the option from *Manual* to *External PML Surface*. Click in *Build All*. Right click once again in *Mesh*, but this time, select the *Swept* option. Change the *Geometric Entity Level* from *Remaining* to *Domain*, and change *Selection* from *Manual* to *PML Domains*. Right click *Swept* and select *Distribution*. Verify if the field *Number of elements* is defined as 5, and click in *Build All*. Right click *Mesh* once again, but this time choose *Free Tetrahedral*. Right click *Free Tetrahedral* and select *Size*. In the option *Element size*, expand the drop down bar and change from *Normal* to *Extra Fine*. Click in *Build All*.

To define the analysis to be performed, the parametrization of frequency excitation is necessary. In *Model Builder* right click in *Study*, and select *Parametric Sweep*. In *Study Settings* click in *Add*. In the new parameter that showed up, select *lambda*. Fill the column *Parameter Value List* with *range(650,5,1050)*. In *Model Builder* click in *Step 1: Frequency Domain*, and in the field *Frequency unit*, write *Hz*. Replace the field *Frequencies* with *c_const/(lambda[nm])*. In the *Model Builder* click in *Component 1*. In the *toolbar* field *Definitions*, click in *Component Couplings* and select *Integration*. Modify the field *Operator Name* from *intop1* to *intop_vol*, and change the *Selection* field from *Manual* with *Nanoparticle*. Repeat the same proceedings, but instead, the name of the new operator is *intop_surf*. In *Source Selection*, modify the *Geometric Entity Level* from *Domain* with *Boundary* and choose the *Selection* field as *Nanoparticle Surface*.

Right click *Definitions* in *Model Build*, and select *Variables*. Fill the table that pops up accordingly to table 4. Now we are ready to begin the simulation. Click in *Study* and select *Compute*. Wait until the simulation is finished. The results are presented in figure 41.

Table 4 – Thermoplasmonic variables to be appraised in COMSOL.

Name	Expression	Value	Description
nrelPoav	nx*emw.relPoavx + ny*emw.relPoavy +	-	
	nz*emw.relPoavz	-	Poynting vector
sigma_sc	intop_surf(nrelPoav)/S_in	-	Scattering
sigma_abs	intop_vol(emw.Qh)/S_in	-	Absorption
sigma_ext	sigma_sc + sigma_abs	-	Extinction
J0	(lambda_ref/(2*pi))*(sigma_abs/Vol)	-	Joule number
S2F	sigma_abs/(beta*Req)	-	Steady-state Factor

Source: belongs to the author.

To obtain such plots after the simulation is finished, it is necessary to evaluate the calculated data. Click in *Results* (toolbar). In *Derived Values* look for *Global Evaluation*. In the settings, select the field *Data set* and choose *Study 1/Parametric Solution 1 (Sol2)*. In *Expression*, type the name of the expression of table 4 that you desire to appraise. In this case, type all variables, except for the Poynting vector. After the expressions were selected, click in *Evaluate* and wait the results to be processed. The generated table can be exported to an external file. Figure 41a presents the optical absorption cross-section response of the gold nanorod. Figures 41b and 41c depict the thermoplasmonic properties of such structure, i.e., its capacity to generate heat. One can observe that all the aforementioned phenomenon occurs for wavelengths around 800 nm in this specific particle.

Figure 41 – Simulated optical and thermoplasmonic properties of a gold nanorod (45 nm x 11 nm) obtained by FEM in COMSOL. (a) Absorption cross-section. (b) Joule number. (c) Steady-state factor.

(a)

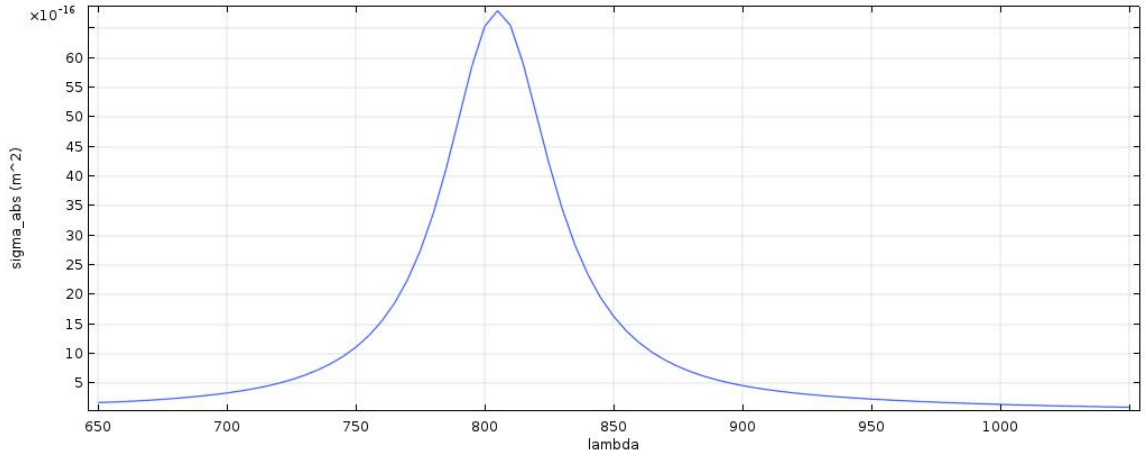

(b)

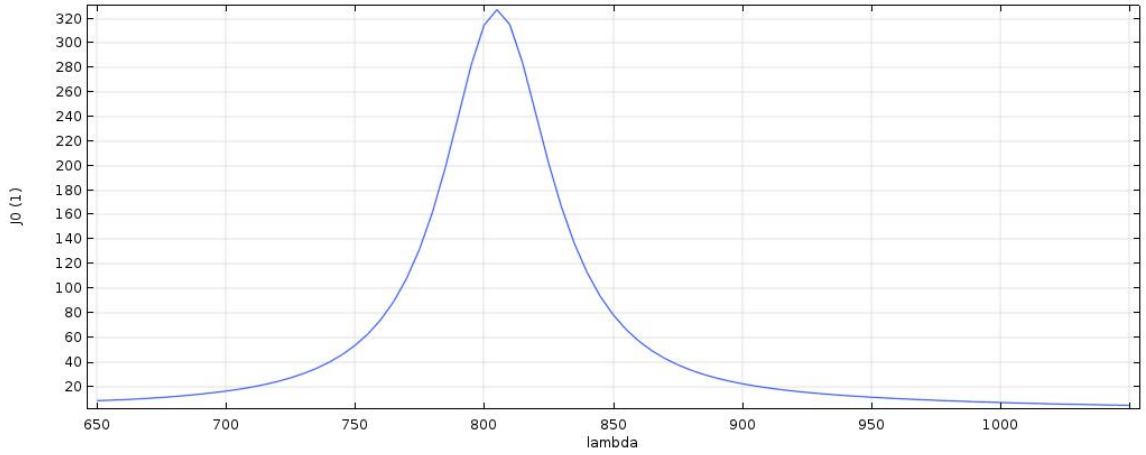

(c)

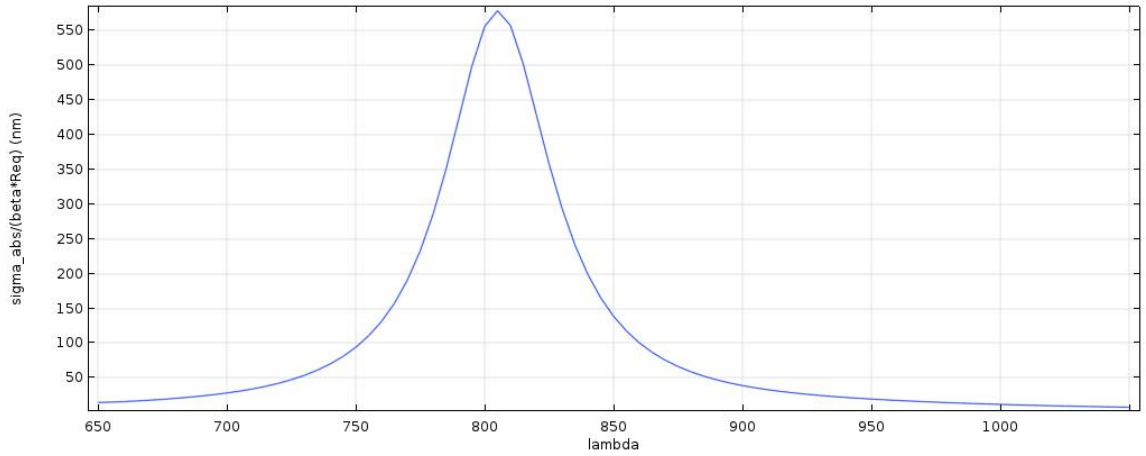

Source: belongs to the author.